Design of a Molten Salt Metal-Air Battery with High-Energy Density – Proof of Concept, Modeling, and Recharging

Abstract

The decarbonization of the shipping industry, among other long-haul transportation, is a significant challenge for eliminating greenhouse emissions. However, a promising solution lies in molten salt magnesium-air batteries, which can offer a high-energy density and cost-effective alternative to lithium-ion batteries. This work investigates a novel molten salt magnesium-air battery using an $MgCl_2$-NaCl-KCl-MgO electrolyte operating at 420-620°C Maximum open-circuit voltage is 1.9 V, which is the highest to date for an Mg-air battery. Experiments and modeling presented here indicate this battery has the potential to deliver 60-90 MWh of energy in a 20-foot shipping container, 15-22 times the energy of containerized lithium-ion batteries, at an upfront cost of about $3-6/kWh. However, the battery's high-temperature operation poses limitations on its scalability, and its round-trip efficiency is lower than that of Li-ion batteries. Future research should focus on the stability of the cathode material and the removal of MgO products from the electrolyte through directional solidification to develop larger-scale cells. Overall, the molten salt magnesium-air battery offers a promising solution for decarbonizing long-haul transportation and reducing greenhouse emissions.

Acknowledgment

I would like to express my sincere gratitude and appreciation to all the individuals who have contributed to the completion of my PhD journey. Firstly, I would like to thank my advisor Prof. Adam Powell, for his unwavering support, guidance, and encouragement throughout my research. His expertise, insights, and constant feedback have been invaluable in shaping my research and developing my skills as a researcher.

I would also like to extend my heartfelt thanks to my loving husband Milad Farzad, who has been my biggest source of strength and inspiration. His patience, understanding, and unwavering support have been instrumental in helping me overcome the various challenges that come with pursuing a PhD.

I am also grateful to my parents and my brother for their constant love, encouragement, and support. Their unwavering belief in me has been a great motivation and source of inspiration throughout this journey.

I would like to acknowledge and thank my colleagues who have supported me throughout my PhD and the undergraduates working on this project: Nicolas Masse, Amanda Lota, Haeth Bastow, Lucien Wallace. And a great thank you to my friends for their encouragement, advice, and friendship have been invaluable in helping me navigate through the various stages of my research.

Finally, I would like to acknowledge the funding from Massachusetts Clean Energy Center for their support in funding my research. Their support has been crucial in enabling me to pursue my research goals and make significant contributions to my field of study. Thank you for your invaluable support.

Table of Contents

Table of Figures

Nomenclature

η_{act}	Activation polarization	T_L	Liquidus temperature
V	Actual cell voltage	L_{el}	Lorenz number (2.44e-8 W. $\Omega.K^{-2}$)
j_{0a}	Anodic exchange current density	C	Molar density
ASR_{ohm}	Area-specific resistance for ohmic polarization	j	Net current density
j_{0c}	Cathodic exchange current density	n_{cells}	Number of cells
α_a	Charge transfer coefficients of anodic reactions	n	Number of electrons participating in the reaction
α_c	Charge transfer coefficients of cathodic reactions	leads	Number of leads
α_i	Charge transfer coefficients of substances where i represents each species in the reactions	η_{ohm}	Ohmic polarization
η_{conc}	Concentration polarization	T	Operating temperature
$D_{cathode}$	Diffusion coefficient of cathode	OCR	Oxygen consumption ratio
D	Diffusion coefficient of charge carrier	η	Polarization
D_L	Diffusivity in the liquid	T_S	Solidus temperature
F	Faraday's constant (96485.3329 C/mol)	ΔT	Temperature above that of environment
G	Gibbs free energy	G_T	Temperature gradient
v	Growth rate	E_{th}	Theoretical open circuit voltage
HEF	Heat exchanger efficiency	L	Thickness of electrode

j_L	Limiting current density	ΔV_{lead}	Voltage loss from the leads
$C_{L,\ cathode}$	Limiting MgO molar density		
E_{cell}	Cell potential (V)		
$E°_{cell}$	Standard cell potential (V)		
R	Gas constant (8.314 J/mol*K)		
Q	Reaction quotient		

Chapter 1- Background

1.1 Literature Review

Batteries have become an integral part of our daily lives, powering various portable and stationary devices, from smartphones to electric vehicles. The development of advanced battery technologies has enabled us to store more energy in smaller packages, making them more efficient and reliable. In this literature review, we will explore the recent advancements in battery technology and their potential applications.

Lithium-ion batteries (LIBs) are widely used in portable devices due to their high energy density, long cycle life, and low self-discharge rate. Recent developments have focused on improving the safety and sustainability of LIBs, as well as increasing their energy density. One approach is to replace the traditional graphite anode with silicon, which has a higher capacity for lithium ions. Another approach is to use solid-state electrolytes instead of liquid electrolytes, which can improve the safety and stability of the battery. A recent study demonstrated a solid-state lithium-ion battery with a high energy density of 350 Wh/kg and a long cycle life of over 1000 cycles [1].

Sodium-ion batteries (NIBs) have gained attention as an alternative to lithium-ion batteries due to the abundance of sodium and its low cost. However, NIBs have lower energy density and cycle life compared to LIBs. Recent research has focused on developing new electrode materials and electrolytes to improve the performance of NIBs. A study demonstrated a sodium-ion battery with a high energy density of 250 Wh/kg and a long cycle life of over 1000 cycles using a high-capacity cathode material [2].

Zinc-based batteries are attractive for their low cost, safety, and environmental friendliness. Recent advancements have focused on improving the energy density and cycle life of zinc-based batteries. One approach is to use a zinc-air battery, which has a high theoretical energy density of 1088

Wh/kg. A study demonstrated a rechargeable zinc-air battery with a high energy density of 450 Wh/kg and a long cycle life of over 1000 cycles [3].

Redox flow batteries (RFBs) are a type of rechargeable battery that uses two tanks of electrolytes to store and release energy. RFBs are attractive for stationary energy storage applications due to their scalability and long cycle life. Recent research has focused on developing new electrode materials and electrolytes to improve the performance of RFBs. A study demonstrated an RFB with a high energy density of 23 Wh/L and a long cycle life of over 1000 cycles using a high-capacity electrolyte material [4].

In Licht et al study in 2013 [5], the authors introduce a new class of high-energy batteries called "molten air batteries," which use air and a molten electrolyte to achieve high intrinsic energy storage capacities. The paper [5] provides examples of three different types of molten air batteries with varying energy densities, highlighting the potential for this technology to be used in a wide range of applications. The three batteries studied in this work [5] are iron, carbon, and VB_2 molten air batteries with respective intrinsic volumetric energy capacities of 10 000, 19 000, and 27 000 Wh/L, compared to 6200 Wh/L for the lithium-air battery. In the following year, Licht et al published a paper focusing on iron air batteries [6]. This technology can operate at temperatures suitable for electric vehicle (EV) applications, which is an important step toward the practical implementation of this technology [6]. The authors demonstrated the successful operation of a low-temperature iron molten air battery, with an average coulombic efficiency of 62% at 1.0 V charge and 0.5 V constant load discharge [6]. The authors attribute this performance to the use of a eutectic electrolyte with soluble $LiFeO_2$ and an optimized cell configuration [6]. In a more recent work from Liu et al. [7] the authors demonstrated a new design that overcomes some of the challenges typically faced with traditional zinc-air batteries, such as low energy density, poor cycle life, and limited rechargeability. The proposed battery design uses a molten salt electrolyte consisting of a mixture of lithium nitrate and potassium nitrate, which can function at temperatures up to 350 °C [7]. The electrolyte is contained within a ceramic membrane and separates the anode and cathode. The anode is made of zinc, while the cathode is a carbon foam catalyst. The

researchers conducted various tests to evaluate the battery's performance, including discharge-charge cycling tests, electrochemical impedance spectroscopy, and cyclic voltammetry [7]. The results of the experiments showed that the proposed battery design had a high energy density of 725 Wh/kg, a long cycle life of over 200 cycles, and excellent rechargeability. Additionally, the researchers found that the battery could be recharged using a simple process of immersing the zinc electrode in a zinc salt solution and circulating air through the cathode chamber [7].

Battery technology is rapidly evolving, with new materials and designs being developed to improve their performance and reduce their environmental impact. Lithium-ion batteries were the dominant technology for portable devices, but alternative technologies such as magnesium-air, sodium-ion, and zinc-based batteries are gaining attention due to their low cost and environmental friendliness. Redox flow batteries are attractive for stationary energy storage applications, but further research is needed to improve their performance and reduce their cost. Overall, the development of advanced battery technologies will play a crucial role in enabling the transition to a more sustainable and electrified future.

Lithium-ion batteries (LIBs) have a wide variety of applications. They are used in portable battery-powered electronic devices, especially in notebook computers and mobile phone applications as well as electric vehicles (EV) and electric motor bicycles [8]. Despite the widespread use of LIBs, they face several challenges for the most demanding applications. These challenges include high cost, lower energy density than fossil fuels, safety, and environmental hazard which makes them less favorable for some energy storage needs [9]. Metal-air batteries on the other hand have been studied since the 1960s [10] and have been intensely focused upon as promising next-generation high-energy batteries [11].

Metal-air batteries use metal as the anodic reactant and oxygen from the air as the cathode. This cathode allows battery weight to drop and makes valuable space available for storing energy. Table 1 provides an overview of metal-air batteries' properties and their costs along with other common or potential shipping energy sources. It is important to note that H_2 with the highest fuel-specific

energy (39.7 kWh/kg), has very low stored fuel-specific energy which is around 1-3 kWh/kg. The next highest fuel-specific energy is for bunker fuels; however, they emit CO_2 as well as SO_2 and soot, the former being the principal greenhouse gas contributing to global warming [12]. Similarly, Alumina (Al_2O_3) is produced when using Al as the anode which can accumulate in organs and leads to health problems. With a molten salt electrolyte, this process also produces aluminum salts ($AlCl_3$) which are highly toxic [13]. However, considering resource availability, Magnesium is an emission-free energy source commercially extracted from seawater that has high fuel and storage-specific energy as well as high energy density and minimal toxicity which make it a suitable alternative for high-energy applications.

Table 1, Comparison of potential fuels and batteries for long-range transportation. The red color illustrated the cons of the energy source while the green illustrates the optimal property

Energy source	Bunker fuel	Mg	NH_3	H_2	Li-ion	Fe	Al
Fuel-specific energy, kWh/kg	12.8	6.9	5.2	39.7	0.2	1.4	8.6
Stored fuel sp. energy, kWh/kg	10	5	3	1-3	0.2		
(Round-trip) efficiency	50%	40-55%	30%	40%	90%	50%	
Delivered energy cost, $/kWh	0.03	0.3	0.4	0.3	<0.1		
Energy storage cost, $/kWh	Small	1-3	10	23	100		2-4
Direct operating emissions	CO_2, SO_2	–	NO_x, NH_3	–	–		Al_2O_3, $AlCl_3$

1.2 Current Metal-Air Battery Challenges

Despite the acceptable range of specific energy of metal-air batteries, efficient direct recovery of electrical energy from most of the metal oxidation enthalpy in a fuel cell is challenging for four primary reasons:

1) Metal oxidation forms a passivating oxide film, and in the case of aqueous electrolytes presence, a hydroxide film. oxide or hydroxide films slow or shut down the reaction.
2) Reactive metals with the highest energy per ion such as Li, Ca, Mg, and Al undergo a parasitic reaction with aqueous electrolytes to form hydrogen [14].
3) The oxygen reduction reaction requires precious metal catalysts such as platinum or palladium.
4) It is necessary to remove the oxidation product from the electrolyte [15].

These challenges are all addressed in the molten air batteries of Licht et al[5]–[7], of which the present MAB design is a new candidate. Starting with the first challenge, the electrolyte also has sufficient metal oxide solubility to avoid oxide film formation. Second, an anhydrous molten salt electrolyte eliminates hydrogen production which helps with both the first and second challenges. The third challenge is resolved by operating at high temperatures which removes the need for precious metal catalysts [5], [6], [16]. The most common cathode material is nickel, which is practically oxidized in situ to NiO [5], [6], [16], [17]. Finally, to mitigate the last problem, one can remove the metal oxide reaction product from the electrolyte by directional solidification or filtration as in [15].

1.3 Magnesium Properties

Magnesium metal is potentially a viable zero-emission fuel for shipping propulsion due to: its higher energy density than liquid fuels, higher specific energy than alkanes, high potential battery efficiency, the prevalence in seawater, fewer health issues than Al and Si, and recyclable products such as MgO, $Mg(OH)_2$ and $MgCO_3$. As presented in last section, an efficient Mg-air battery could cleanly deliver the energy needed for long-haul shipping, and the Mg is an ideal energy shipping medium: Mg specific energy is 3.7 times that of methylcyclohexane-toluene which is considered the most practical way to ship hydrogen.

Batteries are essential for powering various devices, ranging from small electronics to electric vehicles. One promising technology for next-generation batteries is metal-air batteries, which use metals like magnesium as the anode and oxygen from the air as the cathode. Magnesium-air batteries have gained significant attention due to their high energy density, low cost, and environmental friendliness. The following sections include an overview of magnesium-air batteries, including their working principle, advantages, limitations, and current research progress.

MAB generates electricity through the electrochemical reaction between magnesium and oxygen from the air. The anode in MAB is made of magnesium, which oxidizes and releases electrons as it reacts with oxygen to form magnesium oxide. The oxygen from the air acts as the cathode, which turns into oxygen ions by consuming electrons. The overall reaction produces electricity and magnesium oxide. MAB is considered to have a high energy density because magnesium is highly reactive and lightweight, with a theoretical capacity of 2205 mAh/g [18].

MAB has several advantages compared to other battery technologies. These include high energy density, low cost, and environmental friendliness [19]. Magnesium is abundant and inexpensive, which makes it a suitable candidate for large-scale energy storage applications. MAB also do not produce harmful pollutants during operation, making them a cleaner alternative to traditional batteries. Another advantage is their high theoretical energy density, which can potentially be higher than that of lithium-ion batteries [19].

Despite their advantages, MAB also has several limitations. One major limitation is their low efficiency due to the difficulty in recharging magnesium. Recharging involves the oxidation of magnesium hydroxide back to magnesium, which requires high energy and is challenging to achieve. Another limitation is their short lifespan, as magnesium anodes tend to degrade quickly during cycling. Magnesium also has high reactivity with water and can produce hydrogen gas during operation, which can lead to safety concerns [18].

Recent studies have explored different approaches to improve the efficiency and lifespan of magnesium-air batteries, such as using different cathode materials, optimizing the design of the battery, and developing new electrolytes. In this work, we demonstrated the high energy density and good cycling stability of magnesium-air batteries under certain conditions. Moreover, we further studied the need to overcome the limitations of magnesium-air batteries and develop practical applications.

Magnesium-air batteries are a promising technology with high energy density, low cost, and environmental friendliness. However, they also face several challenges, including low efficiency, short lifespan, and safety concerns. These works include efforts to improve the performance and address the limitations of magnesium-air batteries. The development of practical magnesium-air batteries has the potential to revolutionize the energy storage industry and accelerate the transition to clean energy sources.

In a study conducted by Blurton and Sammells [10], a comprehensive overview of metal/air batteries was provided, including their working principles, various types, and potential applications. The authors have conducted extensive research on metal/air batteries and provided valuable insights into their current status, challenges, and prospects.

The paper begins with an introduction to metal/air batteries, highlighting their advantages over other battery technologies, including their high energy density, low cost, and environmental friendliness. The authors then provide a detailed description of the working principles of metal/air batteries, explaining how they generate electricity through the electrochemical reaction between metal anodes and air cathodes.

The authors also discuss the different types of metal/air batteries, including aluminum-air, zinc-air, and lithium-air batteries. They compare the advantages and limitations of each type, highlighting their unique properties and potential applications. The paper also discusses the current

status of metal/air batteries, including their commercialization and the challenges they face, such as low efficiency, short lifespan, and safety concerns.

The authors conclude the paper by discussing the prospects of metal/air batteries, including the potential for developing high-performance batteries for various applications, including electric vehicles and grid energy storage. They also emphasize that different metal-air batteries have their protagonists and they each have a more suitable application. This approach has been followed in this study and the targeted industry for this technology was studied through an NSF ICorps program discussed in Section 1.7.

In another paper authored by Rahman et al. [20] detailed overview of high-energy density metal-air batteries was conducted. The authors identify one of the main advantages of metal-air batteries as their high energy density, which can potentially provide longer battery life and greater storage capacity compared to other types of batteries. They also mention that metal-air batteries are also potentially less expensive and more environmentally friendly than traditional lithium-ion batteries because they do not require the use of toxic materials in their construction. The challenge of these batteries is the need for efficient oxygen diffusion and the potential for the metal anode to degrade over time [20].

A similar study was performed by Olabi et al. [18] provides a comprehensive overview of metal-air batteries, including their working principles, various types, and potential applications. One of the points identified as essential for the commercialization of metal-air batteries is a thermally and mechanically porous cathode electrode that can perform Oxygen Reduction Reaction (ORR) and Oxygen Evolution Reaction (OER) effectively [18]. This paper identifies Al-air and Fe-air batteries as good candidates for large-scale production of metal-air batteries.

As identified by Li et al. [21] to be a preferred electrochemical energy storage solution in the future a battery should have an energy density above 500 Wh/kg and a life cycle over 1000 cycles at a cost lower than $100/kWh [21]. This means with an energy density of 500 Wh/kg, a battery pack

including necessary ancillaries weighing no more than 300 kg would provide sufficient energy to drive EVs for at least 500 km [21].

Cao et al. [22] identified four points that should be further improved in metal-air batteries to develop a highly efficient metal-air battery. First is to optimizing catalytic activity requires careful interface design, as ORR and OER involve multiple phases. Hydrophobicity and porosity must be controlled in electrodes and catalysts to prevent active site flooding due to the relatively low solubility of oxygen in the liquid electrolytes [22]. Secondly, for effective current collection, the electrode or catalyst materials should have a high electrical conductivity. By using highly conductive current collectors/substrates, the inadequate electrical conductivity of catalysts must be reduced. To enable simple electron movement across the interfaces, the contact between catalysts and current collectors also needs to be appropriate [22]. Thirdly, the geometric and electronic structure of a catalyst, which correlates with the binding affinity of oxygen on the surface of active sites, may have a significant impact on the catalyst's ability to catalyze reactions. The design of catalyst materials and the prediction of catalytic activity may both benefit from computational quantum chemistry. Moreover, the orientation and binding energy of oxygen adsorbed to active sites may be impacted by the surface nanostructure and local morphology of the catalysts [22]. Lastly, structures drawn from nature may be helpful in the construction of an air electrode system that can breathe oxygen. Excellent air electrode architectures for metal-air batteries may be provided by bio-inspired structures [22].

Lee et al. [23] provided a fully detailed comparison of Li-air batteries to Zn-air. Zinc morphology can affect the electrochemical behavior of Zn-air batteries because zinc particles with a high surface area can react efficiently with electrolytes [23]. This can be applied to the Mg in Mg-air batteries. Another point that is mutual between the Zn-air and Mg-air is that the architecture of air electrodes is also an important criterion affecting the overall performance of cathode electrodes [23].

1.4 Current Energy Storage Technology

An energy storage system usually comprises mainly batteries, a control and power conditioning system, and the rest of the plant [24]. The batteries, which are the major components are made of stacked cells in which the chemical energy is converted to electrical energy and vice versa [24]. The desired battery voltage and current levels are obtained by electrically connecting the cells in parallel and series [24]. Energy and power capacity are the main features for rating different batteries [24]. Roundtrip efficiency, cycle life, operating temperature, depth of discharge (the extent to which a battery can discharge less than %100), self-discharge, and energy density are other important features describing a battery [16], [25].

Researchers now study multiple battery technologies, some of which are commercially available, and some are still in the experimental stage [26]. Current power systems batteries applications are deep cycle batteries with energy capacity ranging from 17 to 40 MWh and an efficiency of 70-80% [24]. Some of the most widely used batteries in this category along with other energy sources are listed below:

- Lithium-ion (Li-ion): These batteries have lithium metal oxide for the cathode and graphitic carbon with a layer structure for the anode [27]. The electrolyte is lithium salts dissolved in organic carbonates [27]. Li-ion batteries with high energy density (up to 705 Wh/L) and power density (up to 10,000 W/L) are widely used in power sources for cell phones, laptops, and other portable devices [28]. The acceptable temperature region for these batteries is -20^{o}C to 60^{o}C [28] with an optimal range of 15^{o}C to 35^{o}C [28].
- Lead acid: these batteries comprise a cathode electrode of lead dioxide and an anode electrode of sponge lead separated by a micro-porous material. Anode and cathode pairs are immersed in an aqueous sulfuric acid electrolyte.
- Sodium sulfur (NaS): The cathode in these batteries consists of molten sulfur and the anode is molten sodium separated by a solid beta alumina ceramic electrolyte. The operating temperature for these batteries is about 300^{o}C to keep the electrode materials in a molten state [29].

- Metal air: The cathodes in these batteries are air electrodes often made of porous carbon structure, metal mesh covered with proper catalysts [30]. The anodes are commonly available metals with high energy density such as aluminum [31], zinc [32], iron [33], or magnesium [34] that release electrons when oxidized. The electrolytes are often a good hydroxide (OH-) ion conductor in liquid form, a saturated solid polymer membrane [33], or in the case of Mg-air molten chloride salt [34].
- Ammonia: Ammonia is a good energy vector with 22.5 MJ/kg specific energy at a higher heating value (HHV) and 11.5 MJ/L energy density for raw ammonia. It has drawn a lot of attention as its only product is water from either combustion or fuel cells [35]. However, ammonia's toxicity is the major drawback of this technology [36]. Ammonia has a much lower cost to store, and deliver when compared to hydrogen [28].
- Hydrogen: Hydrogen is a non-toxic, clean energy carrier and has higher specific energy than gasoline [37]. With 8.491 MJ/L energy density [35] and 141.9 MJ/Kg specific energy [38], hydrogen has good advantages as a clean energy media, however, storage of hydrogen in liquid form is difficult and requires very low temperatures and/or high pressures [38].

Mg metal is potentially a viable zero-emission fuel with higher energy/volume than hydrocarbons and five times the energy/mass of iron as shown in Figure 1 [39]. It is also abundant with 2x10^15 tons of it in the oceans, and a non-toxic [34]. Comparing Mg-air battery to other metal-air batteries, although the energy density of similar Si-air and Al-air is in principle higher than Mg-air, the volatility of SiCl4, which boils at −60 °C, and toxicity of $AlCl_3$ makes Mg a more suitable material.

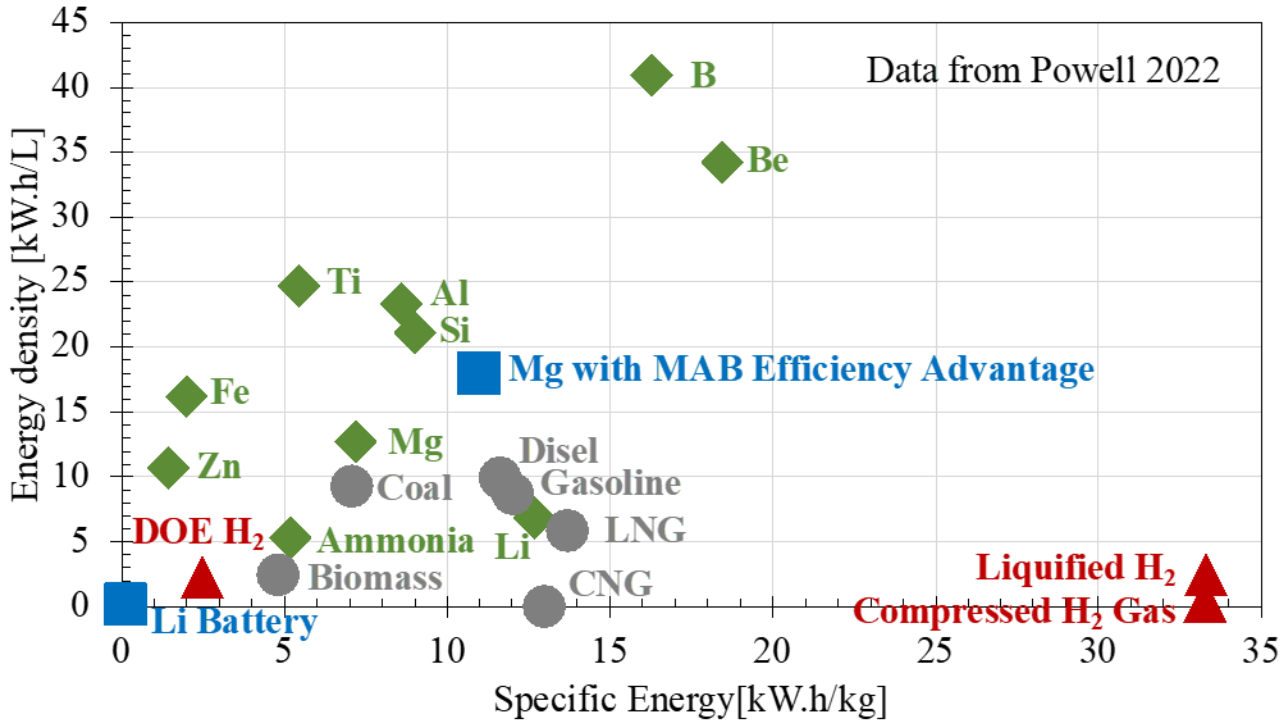

Figure 1, Specific Energy and Energy Density comparison of most popular energy sources

1.5 Current Technologies With Their Criteria Performance

Pressure to reduce shipping's Greenhouse Gas (GHG) footprint has risen sharply and keeps growing [40]. The International Maritime Organization (IMO) is the most influential regulator in the shipping industry and requires them to reduce their shipping emissions [40].

A fully electric cruise ship, Yangtze River Three Gorges 1, started its first voyage in March 2022. It has a 7.5 MWh battery capacity which is equivalent to over 100 EVs. Using this ship will result in 1,660 fewer tons of toxic emissions each year, however, the current range for each charge of this ship is very limited at about 100 km [41].

Another current fully electric ship, the Danish ferry Ellen, is an all-electric ferry with a battery of 4.3 MWh capacity and a travel distance of 40 km. This is also, the first ferry with no emergency diesel generator on board [42].

With two high-end technologies at the same time, Yara Birkeland will be the world's first fully electric and autonomous container vessel producing zero emissions [43]. With a 6.8 MWh

battery, Yara Birkeland will sail between Herøya and Brevik (only 13 km) carrying chemicals and fertilizer [44].
MV Ampere is an electric car ferry currently operating in Norway. It has two onboard 450kW electric motors, powered by lithium-ion batteries and an overall output of 1 MWh traveling 7km in Norway [45].
The current challenge with fully electric ships is the battery's energy density and consequently short travel distances. The Mg-air battery is designed to solve the toughest transportation decarbonization challenges, by efficiently electrifying long-distance shipping.

1.6 Emission-Free Transportation

The transportation sector is responsible for approximately 28% of the country's total greenhouse gas emissions [46]. Some of the strategies to reduce emissions are developing more fuel-efficient vehicles, adopting alternative fuel vehicles, and improving public transportation systems [46].

Federal policies and regulations have a critical role in driving emission reductions in the transportation sector, such as the Corporate Average Fuel Economy (CAFE) standards and the Clean Air Act [46]. Besides them, state and local governments also play a role in promoting sustainable transportation solutions [46]. The United States needs to take a comprehensive and coordinated approach to address transportation emissions, including the adoption of more sustainable transportation solutions, the development of new technologies, and the implementation of supportive policies and regulations; otherwise, the goal of zero net GHG emissions by 2050 cannot be met [46].

Khalil [47] studied hydrogen as an energy carrier and an emission-free transportation fuel. The author presents a detailed analysis of the potential safety risks and hazards associated with hydrogen, as well as the various strategies and frameworks that can be employed to mitigate these risks [47]. For example, Ammonia borane (NH_3BH_3) dust cloud in the air is highly reactive and explosive and discharged alane (AlH_3) dust cloud in the air is more reactive com-

pared to its charged state [47]. The first mitigation strategy is Hydride powder compaction which is an effective risk mitigation strategy that eliminated pyrophoricity and reactivity of hydrides like $NaAlH_4$, $2LiBH_4 + MgH_2$, and $3Mg(NH_2)_{2.8}LiH$ [47]. Therefore, it is important to develop a science-based framework to ensure the safe use of hydrogen as an energy carrier and transportation fuel [47]. The article presents a detailed analysis of the various safety standards, codes, and regulations that have been developed to govern the use of hydrogen, including the International Organization for Standardization (ISO) and the National Fire Protection Association (NFPA) standards [47].

Hasanvand et al. [48] present a novel approach for scheduling the power distribution of an emission-free ship. The purpose of this study is to optimize the power distribution of the ship in real-time, while simultaneously minimizing operating costs and maximizing the reliability of the power system using a deep learning approach [48]. The authors have considered two standards: DNVGL-ST-0033 [49] and DNVGL-ST-0373 [50]. These standards were developed by DNV GL, a global quality assurance, and risk management company, to provide guidelines for the certification of offshore wind turbines. The standard specifies the technical requirements, assessment methods, and documentation needed for certification of offshore wind turbines, including design, manufacturing, installation, and operation. It also covers topics such as structural integrity, safety, and environmental considerations. The DNVGL-ST-0033 standard [49] is widely recognized in the offshore wind industry as a benchmark for quality and safety in wind turbine certification. Moreover, the DNVGL-ST-0373 [50] standard focus on wind turbine manufacturers, as it demonstrates that their turbines meet the industry's technical and quality standards, as well as regulatory requirements. Hasanvand et al. were able to conduct a real-time simulation and successfully showed the performance and efficacy of the proposed method for emission-free ships [48].

In a similar study by Anantharaman et al. [51] the urgent need to reduce greenhouse gas emissions from the shipping industry, which is responsible for a significant portion of global carbon emissions was highlighted. The paper also points out that the International Maritime Organization (IMO) has always been proactive in dealing with this matter to reach the target which is to reduce

GHG emissions by 50% in 2050 compared to the emissions figure of 2008 [51]. The authors discuss the trade-offs of using emission-free alternatives in terms of other environmental impacts such as human toxicity (cancer and noncancer effects) and freshwater ecotoxicity. Anantharaman et al. [51] conclude that hydrogen is the cleaner alternative because of cleaner combustion in internal combustion engines; hence, eLH2ICE and HyMethShip options have a lower impact on the environmental impact categories.

The HyMethShip option was further studied by Malmgren et al. [52] in which they evaluate the environmental performance of a fossil-free ship propulsion system with onboard carbon capture. In this paper, the HyMethShip concept, which uses a combination of hydrogen and methanol as fuel, is analyzed using a life cycle assessment (LCA) approach [52]. This paper indicates that HyMethShip could be an alternative to reduce the climate impact of shipping [52]. Their result has proven a lower impact on acidification, climate change, marine eutrophication, particulate matter, photochemical ozone formation, and terrestrial eutrophication compared to internal combustion engines run on either marine gas oil (0.1% sulfur content), biogenic methanol, fossil methanol, or electro-methanol [52]. Malmgren [52] and Anantharaman et al. [51] both identified toxicity impact as one of the trade-offs of the HyMethShip concept compared to most other options, due to metal needs in wind power plants.

The shipping industry is responsible for approximately 2-3% of global greenhouse gas (GHG) emissions, and this is expected to increase in the coming years. This has led to an increased focus on finding ways to reduce emissions from the shipping industry[53]. Most emissions from the shipping industry come from the burning of fossil fuels in ships' engines. The most common fuels used in the shipping industry are heavy fuel oil (HFO), marine diesel oil (MDO), and liquefied natural gas (LNG). HFO is the most used fuel, but it is also the most polluting, emitting high levels of sulfur oxides (SOx) and nitrogen oxides (NOx), as well as particulate matter (PM). MDO and LNG emit lower levels of SOx, NOx, and PM, but still, contribute to GHG emissions [53].

The following alternatives were studied for the shipping industry [53]–[56]:

a. Low-sulfur fuels: One solution is to switch to low-sulfur fuels such as marine gas oil (MGO) or ultra-low-sulfur fuel oil (ULSFO). This can significantly reduce SOx emissions, but it does not address the issue of GHG emissions [53].

b. Alternative fuels: Another solution is to switch to alternative fuels such as biofuels, hydrogen, or ammonia. These fuels have the potential to significantly reduce GHG emissions, but they are currently more expensive and less widely available than traditional fossil fuels [54], [55].

c. Electric or hybrid ships: Electric or hybrid ships that use batteries or fuel cells to power their engines are another potential solution. These ships emit zero emissions during operation and have the potential to significantly reduce GHG emissions. However, they are currently more expensive than traditional ships and have a limited range [53]. This section is the target of Mg-air batteries which are high-energy density cost-efficient energy sources for turning the shipping industry emission-free.

d. Improved efficiency: Improving the efficiency of ships can also reduce emissions. This can be achieved through measures such as optimizing ship design, reducing ship speed, and improving maintenance practices [54].

Regulatory measures can also play a role in reducing emissions from the shipping industry. The International Maritime Organization (IMO) has introduced regulations such as the International Convention for the Prevention of Pollution from Ships (MARPOL) and the Energy Efficiency Design Index (EEDI) to reduce emissions from ships. In addition, the European Union has introduced the Emissions Trading System (ETS) and the Monitoring, Reporting, and Verification (MRV) regulation to monitor and reduce emissions from ships operating in European waters [53].

Reducing emissions from the shipping industry is crucial to address the issue of climate change. The industry has several potential solutions available, including low-sulfur fuels, alternative fuels,

electric or hybrid ships, and improved efficiency. Regulatory measures can also play a role in reducing emissions from the industry. Further research and investment are needed to develop and implement these solutions on a larger scale [56].

1.7 I-Corps Study

I-Corps (short for Innovation Corps) is a program funded by the National Science Foundation (NSF) in the United States that aims to help researchers and entrepreneurs commercialize their technology and turn it into viable products or services.

The program includes a curriculum designed to help teams identify the target market and potential customers for their technology, as well as to refine their business model and value proposition. The curriculum also includes training on customer discovery, product development, and creating a sustainable business model.

An I-Corps study was conducted as a part of this work. 31 interviews with industry leads were performed and the shipping industry was chosen as the main targeted industry. This is because the main pain point of this industry is its requirement to go emission free by 2050 according to International Maritime Organization (IMO). The key points from the conducted interviews are listed below:

- On average each shipping company owns 7 ships. Big companies (Maersk) own about 1000 ships. Smaller companies follow the innovation chosen by bigger ones.
- The space required for fuel tanks is very large as some ships require a double bottom for safety, about 20 20-foot container
- Nuclear energy is used in US Military submarines and other vessels
- Implementation of the emission-free requirement will be applied by ports, where the ships are operating out of

The business model canvas from this study is shown below:

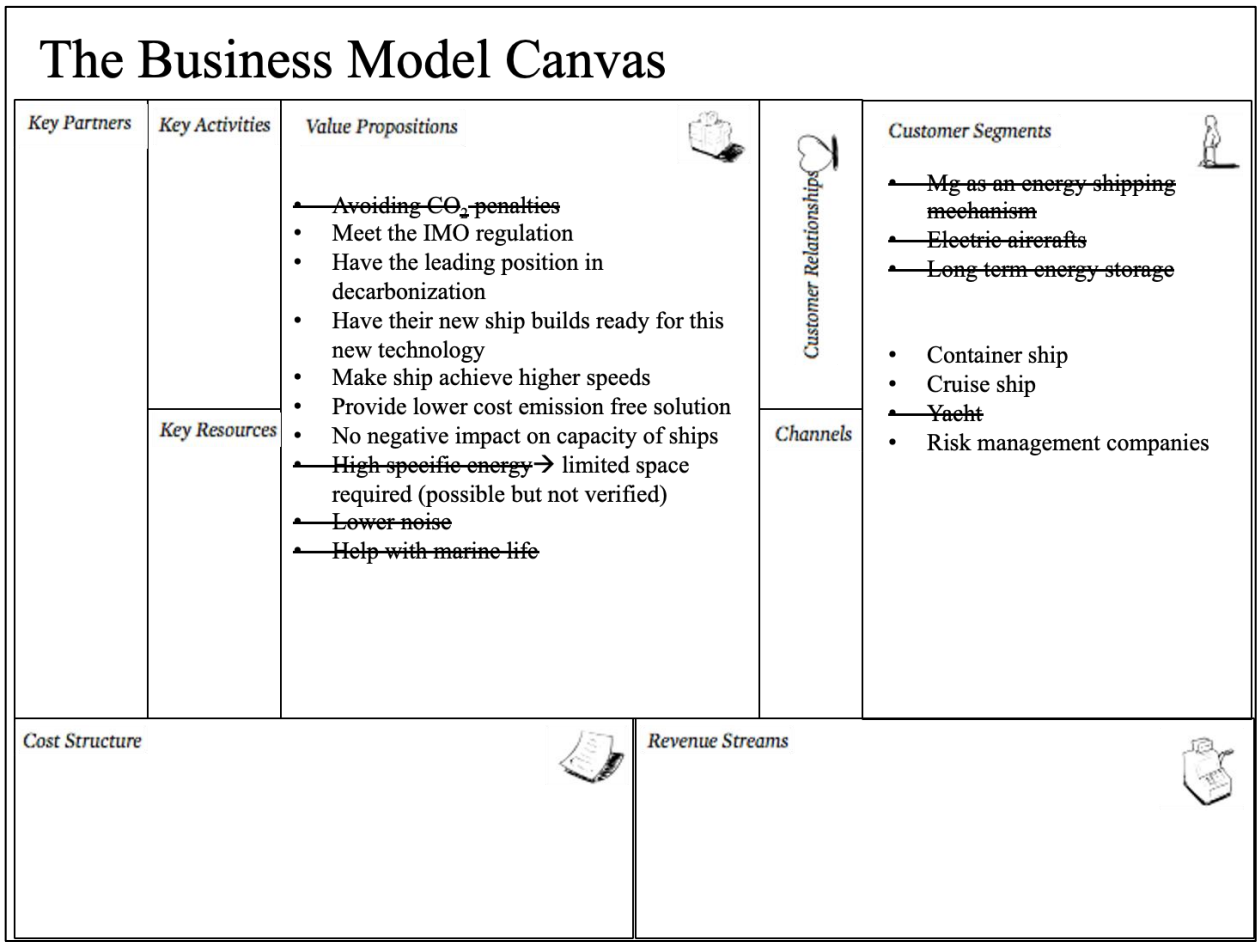

Figure 2, Overview of the business model Canvas, developed for MAB during the I-Corps program

1.8 Overview

The following chapter discusses the theoretical and analytical studies on Mg-air batteries. The next four chapters go through the experimental effort to prove the concept, improve its efficiency, and study long-time discharge and rechargeability. A 1D diffusion model is developed to describe the directional solidification of MgO from this molten salt bath. Finally, Cost modeling analysis is performed. The key findings of this technology are summaries at the end of this work.

Chapter 2 – Analytical Model of Mg-Air Batteries

2.1 Mg-Air Technology

The Mg-air battery presented here consists of the Mg metal anode, the air cathode, and the molten salt electrolyte as shown in Figure 4. The molten salt electrolyte consists of NaCl-KCl-$MgCl_2$ with ~0.5% MgO solubility. Moreover, its eutectic [124] is around 400°C and the Mg melting point at 650°C bound the operating temperature range of approximately 420-620°C.

Cathode: O_2 (air) + 4 e^- (cathode) → 2 O^{2-} (bath)

Anode: 2Mg (anode) → 2Mg^{2+} (bath) + 4 e^- (anode)

Total reaction: 2 Mg+ O_2= 2MgO

Besides the individual ions, other components can be formed during the battery performance and recharging which should be further studied for these batteries. A similar idea was performed for molten salts using a combination of experimental techniques (X-ray scattering and Raman spectroscopy) and computational methods (ab initio molecular dynamics) [57]. The combination of experimental and computational techniques is a powerful approach in materials science research, as it allows for a more comprehensive understanding of complex systems. As shown in Figure 3, from [58], the ternary phase diagram of MgCl2-KCl-NaCl shows the possible phases and their compositions that can exist at different temperatures and concentration conditions for a mixture of these three salts. Based on [57], it is possible that magnesium forms $MgCl_4^{2-}$ or $MgCl_5^{3-}$ complex ions in this type of molten salt. Further analysis will be necessary to confirm presence of those species in this system.

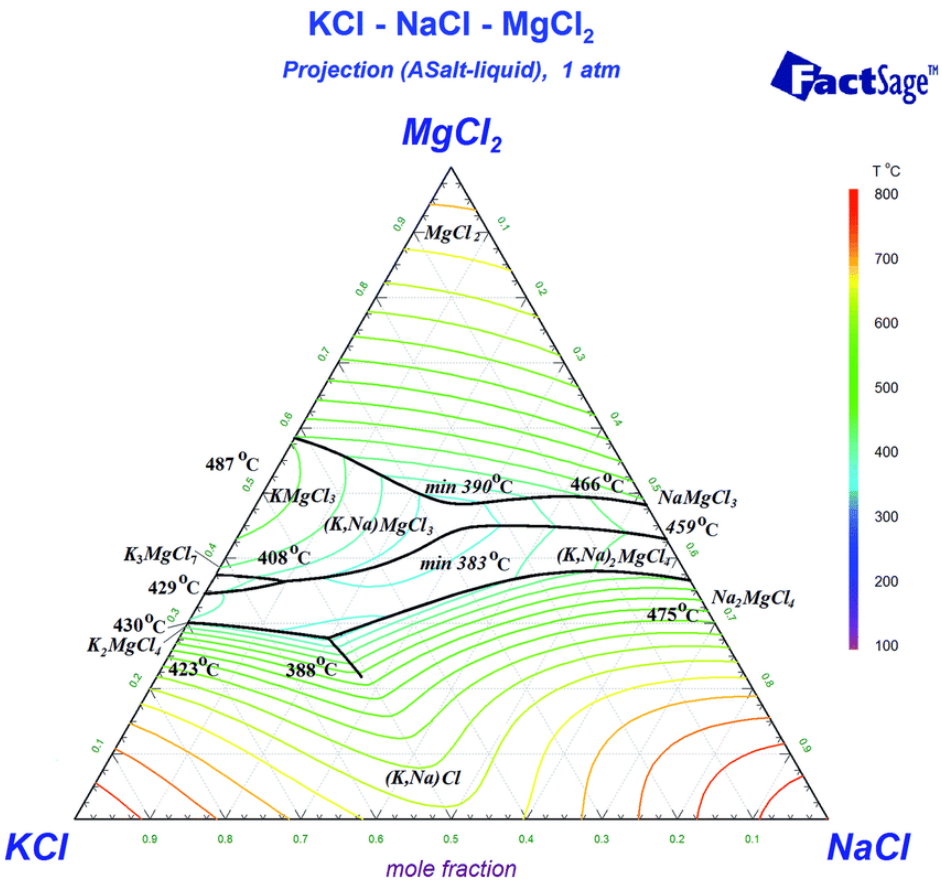

Figure 3, $MgCl_2$, KCl, NaCl ternary phase diagram [58]

2.2 Theoretical Voltage Measurement

The voltage produced by a magnesium-based electrochemical cell can be calculated using the Nernst equation, which relates the cell potential to the concentrations of the species involved in the redox reaction:

$$E_{cell} = E°_{cell} - (RT/nF) \ln(Q) \qquad \text{Equation 1}$$

where:

E_{cell} is the cell potential, or voltage, in volts (V)

E°cell is the standard cell potential, in V, which depends on the specific reaction and can be looked up in tables

R is the gas constant (8.314 J/mol*K)

T is the temperature in Kelvin (K)

n is the number of electrons transferred in the reaction

F is the Faraday constant (96,485 C/mol)

Q is the reaction quotient, which is calculated based on the concentrations of the reactants and products in the electrochemical cell

For a magnesium-based electrochemical cell, the half-reaction at the negative electrode (the anode) is:

$Mg(s) \rightarrow Mg^{2+} + 2\ e^-$

This half-reaction has a standard reduction potential of -2.37 V vs. SHE. The half-reaction at the positive electrode (the cathode) and the electrolyte used will depend on the specific application of the cell.

To calculate the voltage produced by the cell, you would use the Nernst equation with the specific values for the reaction and conditions used in your application. Keep in mind that this is a theoretical calculation and the actual voltage produced may be different due to factors such as electrode materials, electrolyte composition, and other variables.

The reaction quotient, Q, is a measure of the relative concentrations of reactants and products in an electrochemical cell at a given point in time. It is used in the Nernst equation to calculate the cell potential, and it can be calculated using the following equation:

$Q = [C]^c[D]^d / [A]^a[B]^b$

where [A], [B], [C], and [D] are the molar concentrations of the species involved in the cell reaction, and a, b, c, and d are the stoichiometric coefficients of the species in the balanced chemical equation $a\ A + b\ B \rightarrow c\ C + d\ D$

To determine the molar concentrations of the species, you can measure them directly if possible, or estimate them using other information, such as the amount of material added to the cell, the volume of the solution, and the known stoichiometry of the reaction.

For example, suppose you have a magnesium-based electrochemical cell with a magnesium electrode and a copper electrode, and the half-reactions are:

$Mg^{2+} + 2e^- \rightarrow Mg(s)$
$2O^- \rightarrow O_2 + 2e^-$

The overall balanced reaction for this cell is:

$2MgO \rightarrow 2Mg(s) + O_2$

With the magnesium anode always at unit activity, the reaction quotient Q can be written as:

$Q = P\_O_2 / a_{MgO}$ Equation 2

As the reaction proceeds and more MgO is formed, the activity of a_{MgO} increases, Q decreases, and according to Equation 1, E_{cell} increases which means ΔG increases and the reaction becomes thermodynamically less favorable.

This study discusses an Mg-air battery designed to address prior metal-air battery challenges. The modeling section of this study includes a numerical model elaborated to estimate the Voltage/Current relation of the cell. The experimental setup is then tested which showed the highest open-circuit voltage for an Mg-air battery to date: 1.9 V.

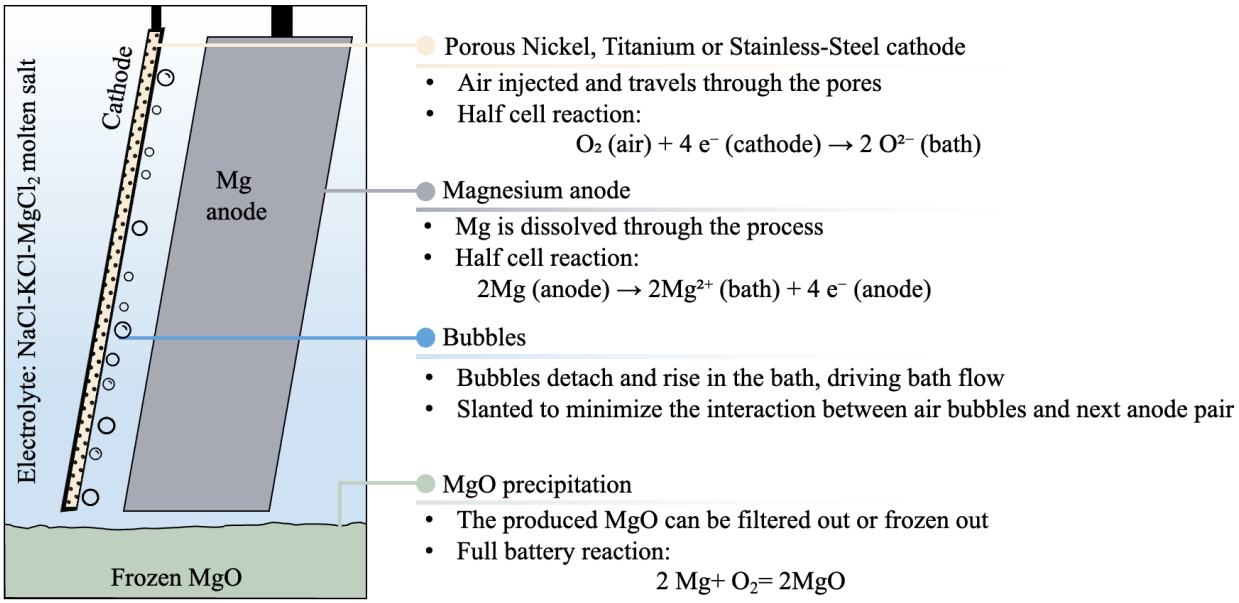

Figure 4, Design on MAB and component description

2.3Analytical Model & Polarization

Polarization in batteries refers to the accumulation of charges at the electrodes of the battery, which can cause a decrease in the battery's performance. When a battery is in use, chemical reactions take place at the electrodes to produce an electric current. As the battery discharges, the concentration of reactants at the electrodes decreases, which can lead to an accumulation of charge at the electrodes. This charge buildup can create a potential barrier that opposes the flow of current, reducing the battery's efficiency and capacity.

To reduce polarization, various techniques are used in battery design, such as incorporating conductive additives in the electrodes or using high surface area electrode materials. In addition, periodic recharging of batteries can help to reverse polarization and restore the battery's performance.

Activation polarization in batteries is a type of polarization that occurs when a battery is initially activated or started up. When a battery is not in use, the reactants at the electrodes are in a state of equilibrium and the chemical reactions do not occur. However, when a load is connected to the battery, chemical reactions start to occur, and the current flows through the battery.

During the initial activation of the battery, a certain amount of energy is required to initiate the chemical reactions at the electrode surfaces. This energy is referred to as activation energy, and the amount of energy required depends on factors such as the nature of the electrodes, the type of electrolyte used, and the temperature of the battery.

Activation polarization occurs when the activation energy required to initiate the charge transfer electrochemical reactions is higher than the energy available in the battery, which can lead to a decrease in the battery's performance. This can be particularly problematic for batteries with high internal resistance or low-temperature operation.

To reduce activation polarization, battery designers may use materials with lower activation energies, such as catalysts or high surface area electrodes. They may also adjust the operating temperature of the battery or optimize the battery's internal resistance to reduce the amount of activation energy required. Higher temperatures, such as those of this MAB, tend to reduce the activation polarization dramatically, in this battery it is likely negligible (<0.1 V).

Ohmic polarization in batteries is a type of polarization that occurs due to the resistance of the battery's components to the flow of current. When a current flows through a battery, it encounters resistance as it passes through the electrodes, electrolytes, and other components. This resistance, also known as the internal resistance of the battery, can lead to a voltage drop across the battery, which reduces the voltage available to the load and can cause a decrease in the battery's performance.

Ohmic polarization is caused by the resistance of the battery's components to the flow of current. This resistance depends on factors such as the size and geometry of the electrodes, the conductivity of the electrolyte, and the temperature of the battery. The higher the resistance, the greater the voltage drop across the battery and the greater the ohmic polarization.

To reduce ohmic polarization, battery designers may use materials with higher conductivities, such as electrolytes with higher ionic conductivities or electrodes with higher electrical conductivities. They may also optimize the size and geometry of the electrodes to reduce resistance or adjust the temperature of the battery to reduce the viscosity of the electrolyte, which can improve its conductivity. In addition, using larger cross-sectional area conductive paths can also help to reduce the internal resistance of the battery.

Concentration polarization in batteries is a type of polarization that occurs due to the depletion of reactants or excessive accumulation of products at the electrode surfaces, which can limit the rate of the electrochemical reactions in the battery. During battery discharge, the reactants at the electrodes are consumed to produce electrical energy, and as a result, the concentration of reactants at the electrode surfaces decreases. This decrease in concentration can create a concentration gradient, which can limit the rate of the electrochemical reactions.

Concentration polarization is most observed in batteries that use liquid electrolytes. In such batteries, as the concentration of the reactants decreases, the concentration gradient across the electrolyte-electrode interface increases, leading to a decrease in the rate of the electrochemical reactions. This can reduce the performance of the battery and limit its overall capacity.

To reduce concentration polarization, battery designers may use materials or additives that improve the availability of reactants at the electrode surfaces, such as high surface area electrodes or porous electrodes that increase the effective surface area. In addition, increasing the flow of the electrolyte or agitation of the electrolyte can help to reduce concentration polarization by

increasing the transport of reactants to the electrode surfaces. By minimizing concentration polarization, the battery's performance can be improved, and its overall capacity can be increased.

2.4 Electrochemical Model

The energy balance modeling of the proposed Mg-air battery was calculated based on former solid oxide fuel cell studies [59]–[63]. Pure magnesium was used as the anode material and porous nickel was used as the cathode. $MgCl_2$-NaCl-KCl-MgO (19.9-32-48-0.1 wt%) molten salt was used as the electrolyte. Due to the losses in the cell, the actual cell voltage (V) is less than the theoretical open circuit voltage [59], E_{th}, and illustrated in Equation 3 where η shows the polarization and ΔV_{lead} shows the voltage loss from the leads. Moreover, Kakac et al. found these polarizations by categorizing them into three separate groups: activation polarization, ohmic polarization, and concentration polarization which are shown by η_{act}, η_{ohm}, and η_{conc} respectively. The η_{act} is insignificant and ignored in this study. According to electromotive force (EMF), the theoretical open-circuit voltage can be calculated based on Gibbs's free energy of the cell reaction as shown in Equation 4 and 3.

$$V=E_{th}\text{-Losses}=E_{th}-\eta-\Delta V_{lead} \quad \text{Equation 3}$$

$$V=E_{th}-\eta_{act}-\eta_{ohm}-\eta_{conc}-\Delta V_{lead} \quad \text{Equation 4}$$

$$V=\frac{-\Delta G}{nF}-\eta_{act}-\eta_{ohm}-\eta_{conc}-\Delta V_{lead} \quad \text{Equation 5}$$

Furthermore, one can calculate the three polarizations using Equation 6 [64]. In the later equation, j_L is the limit of the current density of the electrode is calculated using Equation 9 [64].

$$\eta_{act}=\frac{RT}{nF}\left(\frac{1}{\alpha_a}\ln\left(\frac{j}{j_{0a}}\right)-\frac{1}{\alpha_c}\ln\left(\frac{j}{j_{0c}}\right)\right) \quad \text{Equation 6}$$

$$\eta_{ohm}=jASR_{ohm} \quad \text{Equation 7}$$

$$\eta_{conc}=\frac{RT}{nF}\left(1+\frac{1}{\alpha_i}\right).\ln\left(\frac{j_L}{j_L-j}\right) \quad \text{Equation 8}$$

$$j_L=nF\frac{D\,\Delta C}{L} \quad \text{Equation 9}$$

Finally, the voltage corresponding to energy loss in the leads (ΔV_{lead}) is calculated using Equation 10.

$$\Delta V_{lead}=2\sqrt{L_{el}\, T\, \Delta T} \qquad \text{Equation 10}$$

The parameters and assumptions used for this study are shown in Table 2 [62], [65]. Using this information, the limiting current density of the anode and the cathode was found as 7.72 and 2.92 A/cm^2 respectively. Oxygen consumption ratio and heat exchanger efficiency are model parameters assumed as 50% and 90% respectively. Furthermore, the energy loss per cell was 0.04V. As shown in Figure 5, the $\frac{-\Delta H}{nF}$ value for the designed cell was 3.2 V. The theoretical voltage was found as $\frac{-\Delta G}{nF}$ =2.62 V. Similarly, the voltage after lead loss and air heat exchange loss was found as 3.07 V.

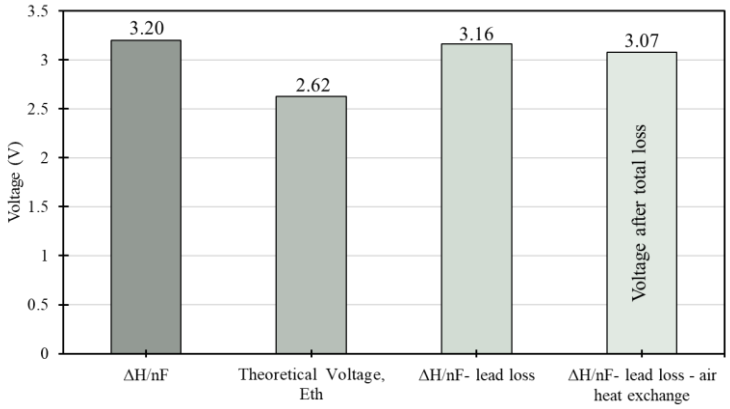

Figure 5, The voltage loss through entropy, lead loss, and Mg and air heat exchange

Table 2, Battery performance model parameters

L	Thickness of electrode	0.5 cm
E_{th}	Theoretical open circuit voltage	2.624195 V/mol
T0	Ambient temperature	293.15 K
T	Operating temperature	823.15 K
$D_{cathode}$	Diffusion coefficient of cathode	0.9615 cm2/s
$C_{L,cathode}$	Limiting MgO molar density	3.94E-06 mol/cm^3
α_{MgO}	Charge transfer coefficients of MgO for cathode	2
α_{Mg}	Charge transfer coefficients of Mg for anode	2
n_{leads}	Number of leads	2
n_{cells}	Number of cells in a “stack”	10
ASR_{ohm}	Electrolyte area-specific resistance for ohmic polarization	0.5626 Ω·cm^2

OCR	Oxygen consumption ratio	50%
HEF	Heat exchanger efficiency	90%

Chapter 3 – High-Temperature Experiments

3.1 Experimental Setup and Procedure

The high-temperature experiments explained in this section were designed as a proof of concept for the described Mg-air battery and to measure the open-circuit voltage (OCV) of the battery. Compared to the energy balance modeling the voltage was expected to be around 2.6 V.

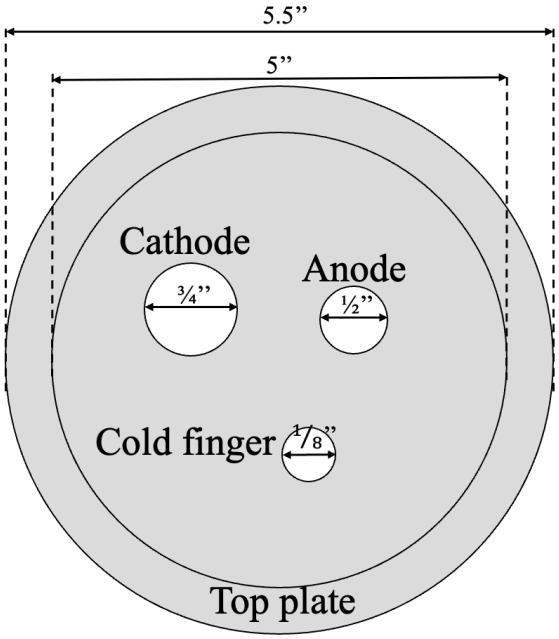

Figure 6 shows the experimental setup schematic. The salt ($MgCl_2$ 40 wt%, NaCl 27.5 wt%, and KCl 32.5 wt%) was added to the crucible and placed into the furnace. The anode and cathode were set up to stay above the crucible at the start of the process. The Mg anode was in the shape of a cylinder with a 2.5cm diameter and 1.5-8 cm height. Nickel mesh, with a 2 cm^2 exposed area was attached at the end of the cathode. Before the start of the experiment, the oxygen partial pressure of the chamber was verified to stay below 0.05 bar by injecting Argon gas. This prevented the burning of the graphite components as well as the oxidation of the other components. The furnace temperature was then increased and kept at 450°C to stabilize. Next, the temperature was ramped up to 500°C and stabilized. Similarly, two more steps were taken to stabilize the temperature to

550°C and 600°C. All temperature ramping-up rates in this experiment were 10°C/min. The setup was ready to start the test once all the salt was molten. Then, the anode and cathode were inserted into the molten salt bath, airflow through the nickel mesh cathode began at 1 standard liter/minute, and the voltage and current were measured at variable resistance using the voltmeter. Both anode and cathode were drawn out of the bath before shutting off the furnace and ending the experiment.

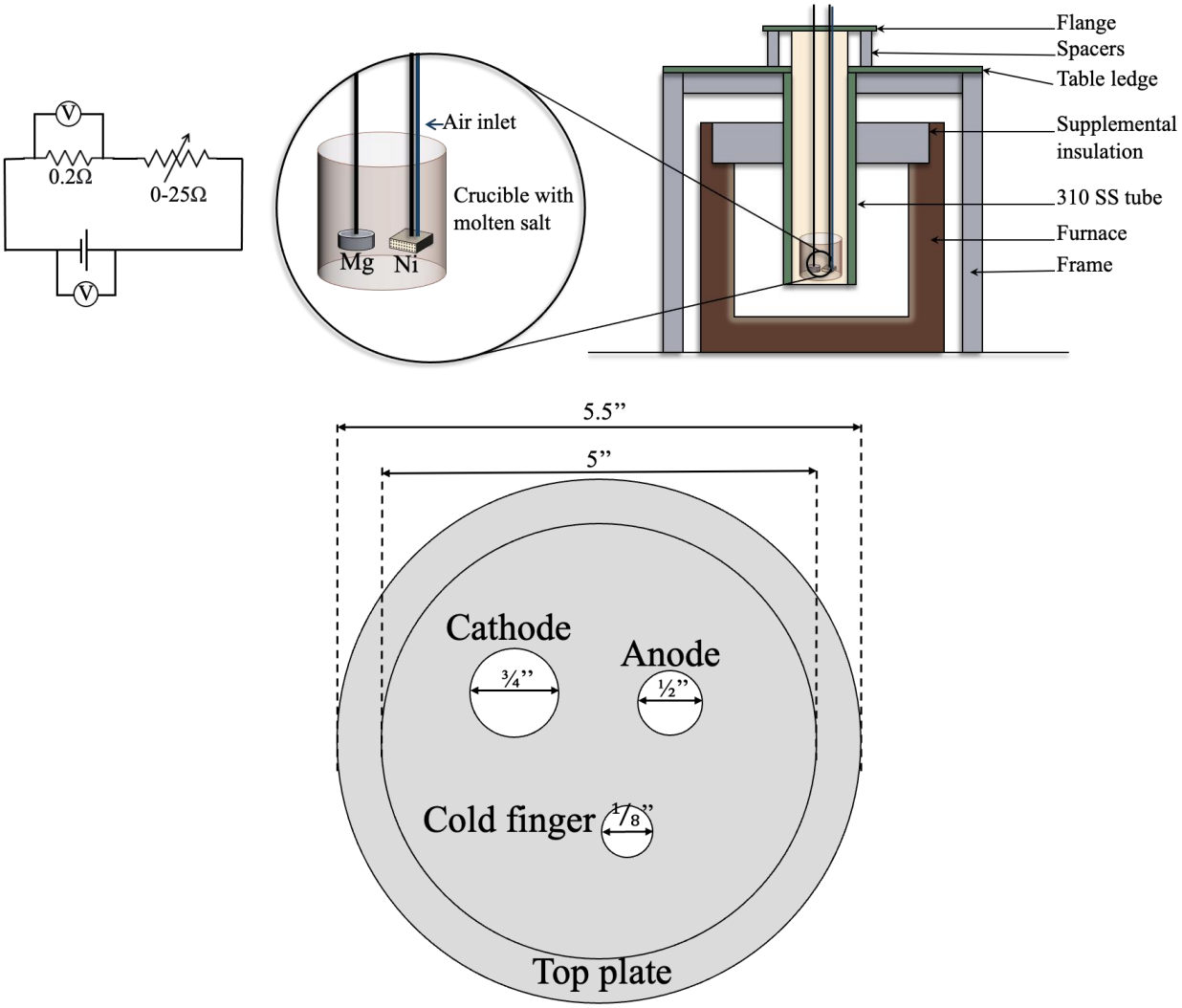

Figure 6, Schematic of MAB experimental setup and electrical wiring

3.2 Experimental overview

Exp #	Goals	Main Findings	Max OCV
Exp1	Proof of concept and show the OCV of the battery	• With only passive cooling of the top plate, it gets too hot • The use of baffles and a cooling fan is necessary	NA
Exp2	• The OCV around 2.6V at 550 ºC • The current is around 6A at 0V	• Max voltage of 1.83 V was achieved • The current of 2.4 A was achieved	1.83 V
Exp3	• The OCV around 2.6V at 550 ºC • The around 6A at 0V • Operating time longer than 33 min based on the previous experiment	• Max voltage of 1.25 V was achieved • The current of 2.94 A was achieved • Proof of concept achieved	1.25 V
Exp4	• The OCV around 2.6V at 550 ºC • The around 6A at 0V • Operating time longer than 33 min based on the previous experiment	• Max voltage of 1.94 V was achieved • The current of 2.41 A was achieved	1.94 V
Exp5	• The OCV around 2.6V at 550 ºC • The around 6A at 0V • Operating time longer than 33 min based on the previous experiment	• Max voltage of 1.78 V was achieved • The current of 2.96 A was achieved	1.78 V

Exp6	Repetition of the previous experiment	• Max voltage of 0.9 V was achieved	0.9 V
Exp7	Repetition of the previous experiment	• Max voltage of 1.38 V was achieved	1.38 V
Exp 8	Study the effect of cold finger starting mid-test	• Using a cold finger increased OCV almost as high as the initial value • Cold finger reduces voltage fluctuations	1.6 V
Exp 9	• Repeat Exp8 to verify the effect of a cold finger • Use a desiccant to dry the injected air through the cathode	• Using a cold finger increased OCV almost as high as the initial value • Cold finger reduces voltage fluctuations	1.26 V
Exp 10	• Use a data logger to measure data • Study how the voltage change during inserting the cold finger	• At the moment of starting the cold finger, the voltage drops but then gradually increases up to almost the initial OCV • Isolation problem found between the cathode and the furnace's top plate	1.17 V
Exp11	• Ensuring electrical isolation of the cathode by using an insulating tube • Isolating the top plate from the furnace body by adding tapes	• Isolation problem still exists	1.23 V

EXP12	• No prebaking of the salt, holding the salt at 250C for 3h during heating in the experiment to dry it	Isolating ceramic plates were missing under the crucible Skipping prebaking and drying the salt inside the furnace does not significantly affect the results	1.2 V
EXP13	• Higher cold finger flow (higher than the rotameter range) • Set the potentiometer to R=1ohm and run for a long time discharge • Not missing ceramic isolations for the crucible • No prebaking of the salt	• Higher cold finger flow did not affect the voltage plot significantly • However, it ensured keeping the voltage at around 0.15 V for a relatively long time	1.6 V
EXP14	• Connect potentiosatat • Apply resistance sweeps by a potentiostat • No prebaking of the salt	• Unable to use the data from the potentiostat • Potentiostat does not match the current range of our battery	1.13V
EXP15	• Second potential stat test • Put the cathode in epoxy and cut it in half • No prebaking of the salt	• Unable to use potentiostat • The cathode was epoxied and studied	NA
EXP 16	• Long rung • Adding ammonia chloride for high OCV • Preheating as usual	• Adding ammonia chloride resulted in higher OCV • Current loss exists in the system • Measured Mg dissolved • Cold finger used from early on in the experiment	1.8 V

EXP17	• Very long run, 30h run time • Preheating as usual	• Discharge for more than 30h • Current-Voltage plots dropped over time • Lower current than expected	1.31 V
EXP18	• First recharging • Multiple recharging sweeps • Preheating as usual	• Three recharging sweeps performed • Other elements rather than Mg were deposited on the anode • Thin Mg dendrites were formed around Mg as seen in EDS	0.96 V
Exp19	• Second recharging • Constant current recharging	• Five recharging sweeps • Ti deposited on the original Mg anode	1.5V
Exp20	• Changing cathode mesh from Ni to dense Ti • Discharge only	• Unstable battery voltage	1.46 V

3.3 Experiment 1

In the first experiment, the goal was to study the heat up and cool down of the system. Only passive cooling was applied on the top plate and there was no insulation around the baffles. This will make the top plate heat up to around 200 ^{o}C which is approaching the O-ring service temperature. Based on this experiment, a fan was used to cool down the top plate and prevent any damage to the O-ring and furnace seal.

3.4 Experiment 2

In the second experiment, the goal was to achieve the theoretical values calculated in Section 02.3. the expected OCV at 550°C was estimated as 2.6 V and the maximum current of around 6 A.

3.5 Experiment 3

A similar goal to as of experiment 2, was applied to experiment 3. To identify the performance of the Mg-air battery discussed in this work, the voltages measured from the experiments were compared with modeling results and are shown in Figure 8. Figure 8 compares the calculated power from the experiments with the modeling results. As discussed in Chapter 2, OCV expected from the cell was 2.62 V. As the current increases the voltage decreases due to the concentration and ohmic polarization. The result from the electrochemical modeling illustrated that the Mg-air battery can operate under 0.5 A/cm^2 current density and 1.17 W/cm^2 power density at 73% efficiency. Similarly, 36% efficiency was achieved when operating under 2.5 A/cm^2 current density and 2.89 W/cm^2 power density.

The two experiments showed reasonable agreement with the model as shown in Figure 8. Lower measured cell performance than the model prediction is likely due to the presence of MgO reaction product in the bath, which the model does not include. The first experiment reached a very high current density of 2.9 A/cm^2 which is almost equal to the limiting current density (2.92 A/cm^2). Moreover, the second experiment reached 1.86 V which is 71% of the theoretical OCV. In both experiments, following the initial run, both OCV and current density fell over time. After each experiment, the nickel mesh cathode was partially blocked, with most pores filled with solid salt and some remaining open.

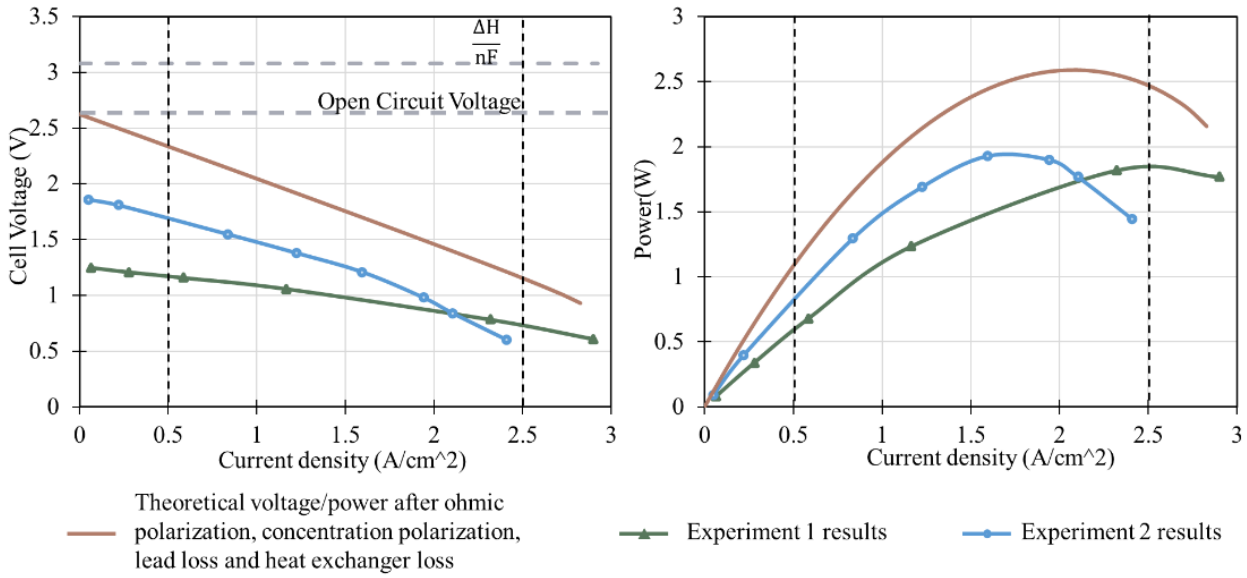

Figure 7, MAB results from the analytical model and initial three experiments which prooved the concept

3.6 Experiment 4

After proofing the concept of Mg-air batteries in experiments 1 and 2, the following four experiments were conducted to reassure and double-check the voltages. The results from experiment 4 are shown in Figure 8, which shows the high OCV of 1.94 V and maximum current of 2.41 A.

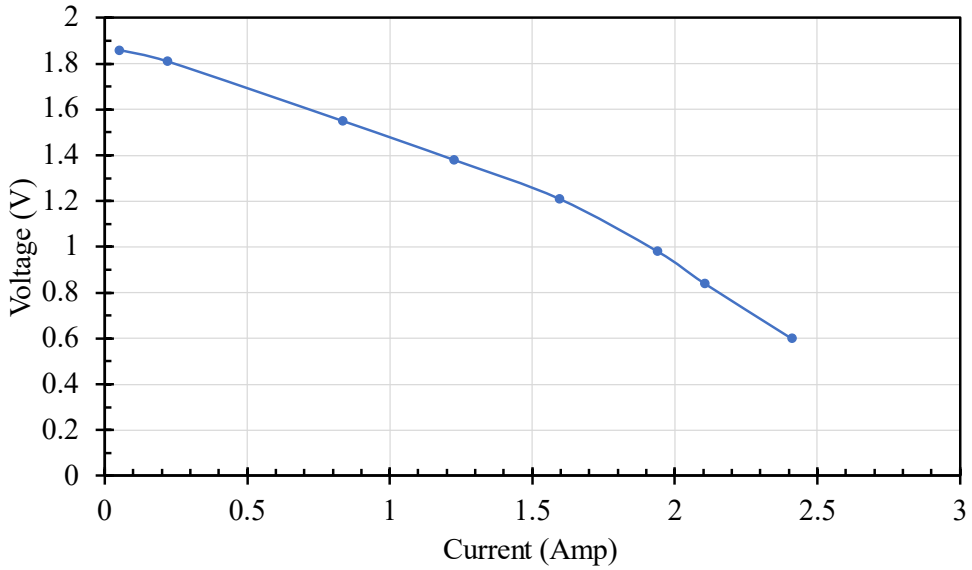

Figure 8, V-I Plot from experiment 4

3.7 Experiment 5

In a similar study as the previous experiment max voltage of 1.78 V and a maximum current of 2.96 A were achieved. The experimental results from this experiment are shown in Figure 9. As shown in this Figure 9, the voltage-current drop over time is most probably due to the increase of MgO in the molten salt electrolyte which decreases the thermodynamical tendency for the Mg to turn into MgO as explained in Section 2.2.

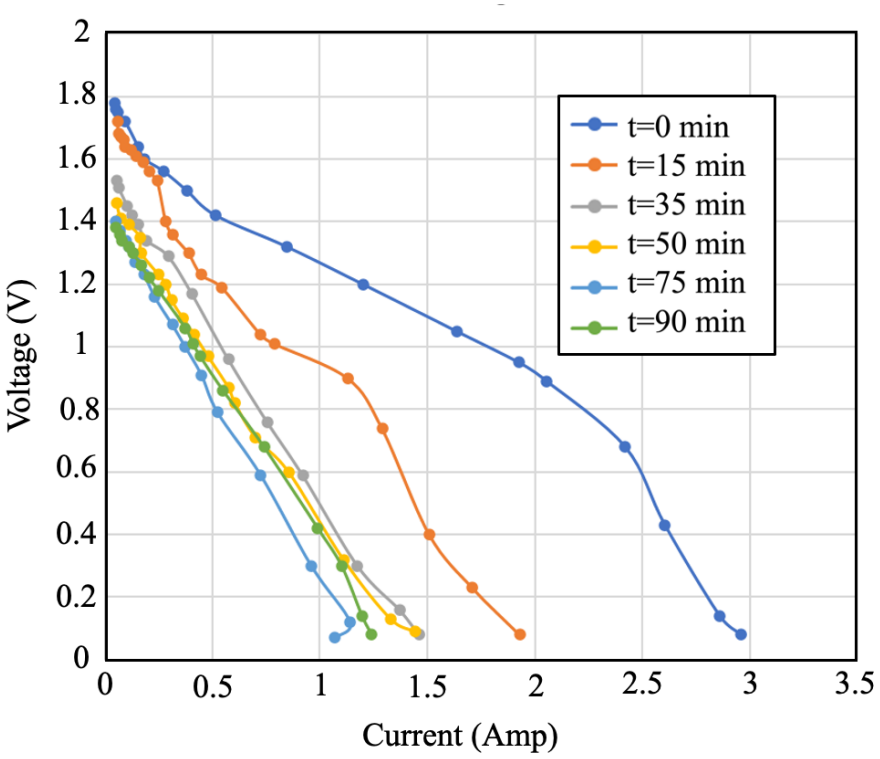

Figure 9, V-I Plot from experiment 4

3.8 Experiment 6

The approach taken in experiment 6 is similar to the one from experiment 5 and the results also show a similar trend as shown in Figure 10. In this experiment, the drop in current is much more significant than the drop in current. This has been explained in the following experiment.

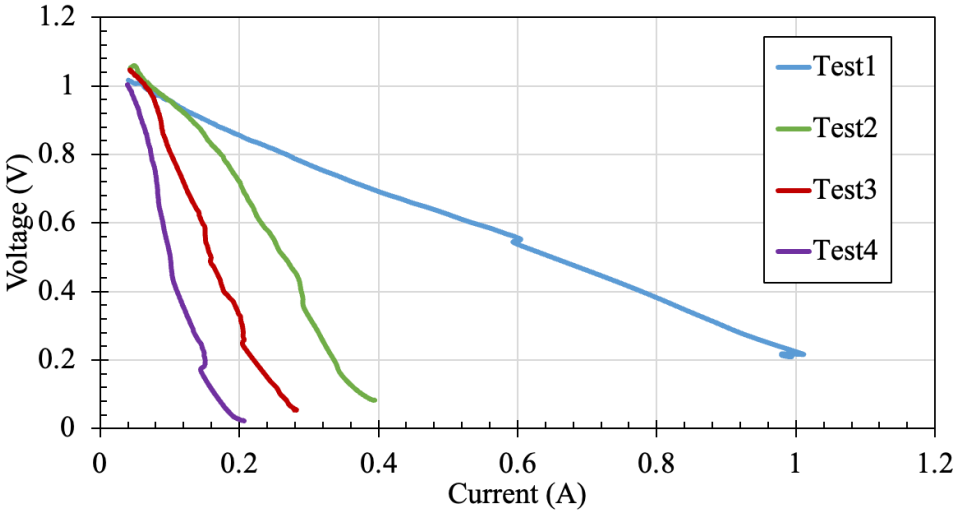

Figure 10, V-I Plot from experiment 6

3.9 Experiment 7

Experiment 7 illustrated a similar trend in voltage drop throughout the experiment. This leads the team to an innovative idea of using the cold finger to keep the MgO concentration low in the molten salt electrolyte.

Chapter 4- Efficiency Improvement Using Cold Finger

4.1 Experiment 8

The eighth Mg-air battery experiment started similarly to the previous one. The electrolyte salt (MgCl2 20 wt%, NaCl 32 wt%, and KCl 48 wt%, eutectic temperature 403^{o}C) was added to the crucible and placed in a furnace of 300^{o}C to prebake and eliminate its excess moisture content. The crucible was then put in the experimental cage as shown Figure 11. Next, the cathode which consisted of a stainless-steel tube with porous nickel mesh at the bottom was set up to stay above the crucible. The nickel mesh has 2 cm^{2} of exposed area. Similarly, the anode which was a stainless-steel threaded rod with a cylinder shape Mg with a 2.5 cm diameter and 5 cm height screwed to the bottom was set on top of the crucible. What was new in this experiment was the use of a cold finger. The cold finger consists of two tubes nested within one another. The inner tube is a 304 stainless steel tube with a 0.125'' outer diameter (OD) and was used for injecting the compressed air. The outer tube was a stainless-steel tube with 3/8'' OD with a close-ended Yor-Lok connection. After isolating the crucible from the cage and connecting the thermocouples to the system, the experimental cage was inserted into the furnace and the system was sealed to minimize oxygen interaction during temperature ramp-up. Before starting the heated ramp-up, the oxygen partial pressure was reduced to below 0.05 bar by injecting argon gas into the furnace. First, the temperature was set to 250^{o}C at 10^{o}C/minute and held for 60 minutes to remove water with minimal oxide formation. Then the temperature was increased to 550^{o}C at the same rate. The battery was ready to perform once the salt was fully molten. Next, the cathode's air flow of 1 standard liter/minute was started and inserted into the molten salt bath along with the anode. OCV and voltage vs. current data were recorded using a potentiometer to sweep resistance from 0 to 25 ohms. After 1.5 h of battery operation and data logging, the cold finger flow was started, and it was inserted into the molten salt. Due to the cool-down effect of the cold finger, the MgO will most likely deposit on the cold finger and filter out from the molten salt, reducing the MgO concentration in the salt. When ending the test, all anode, cathode, and cold finger leads were

drawn out of the bath, the cathode and cold finger flows were shut off and lastly, the furnace was turned off.

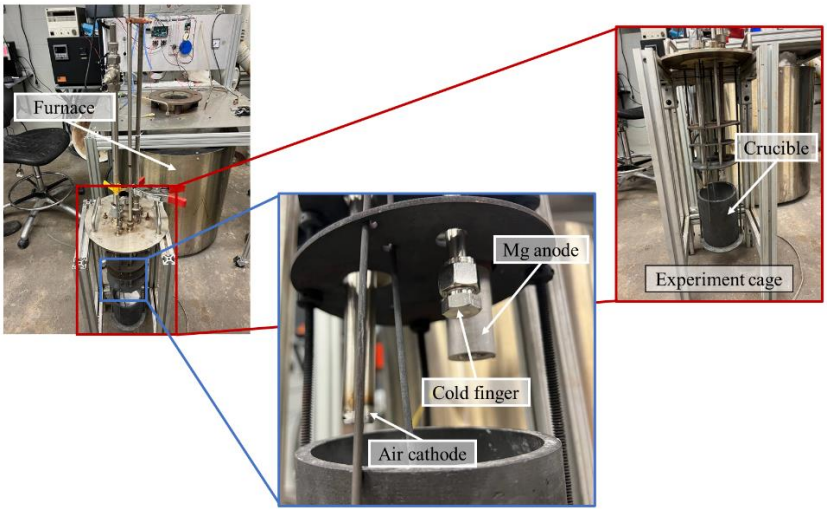

Figure 11, Cold finger experimental setup

To identify the cold finger effect on Mg-air battery performance, the voltage-current plots were studied. The electrical circuit consists of the battery, a 0.02 Ω shaft resistor, a 0-25 Ω potentiometer, and a voltmeter to measure the battery voltage. At the beginning of the test, the OCV was 1.58±0.01V. Starting 10 minutes into the test four resistance sweep tests were performed with a 10-minute interval between the first three tests and 40 minutes interval for the last one. In these tests, the resistor was decreased from 25Ω to 0Ω and then back to 25Ω. As shown in Figure 12, the voltage for different currents decreases as the battery is used which can be due to the increasing composition of MgO in the molten electrolyte. After 2.5 h of the battery running the cold finger cooling down flow was started at 1000 SCCM, and the cold finger was inserted into the molten electrolyte. Five minutes after cold finger initiation the OCV started to increase from 0.55V to 1.35V. The cold finger flow was then increased which resulted in a further increase of OCV to 1.39V as shown in Figure 13. Figure 13 shows the Mg and cold finger after the experiments. It is visible that a layer of oxides was formed on the cold finger in this process.

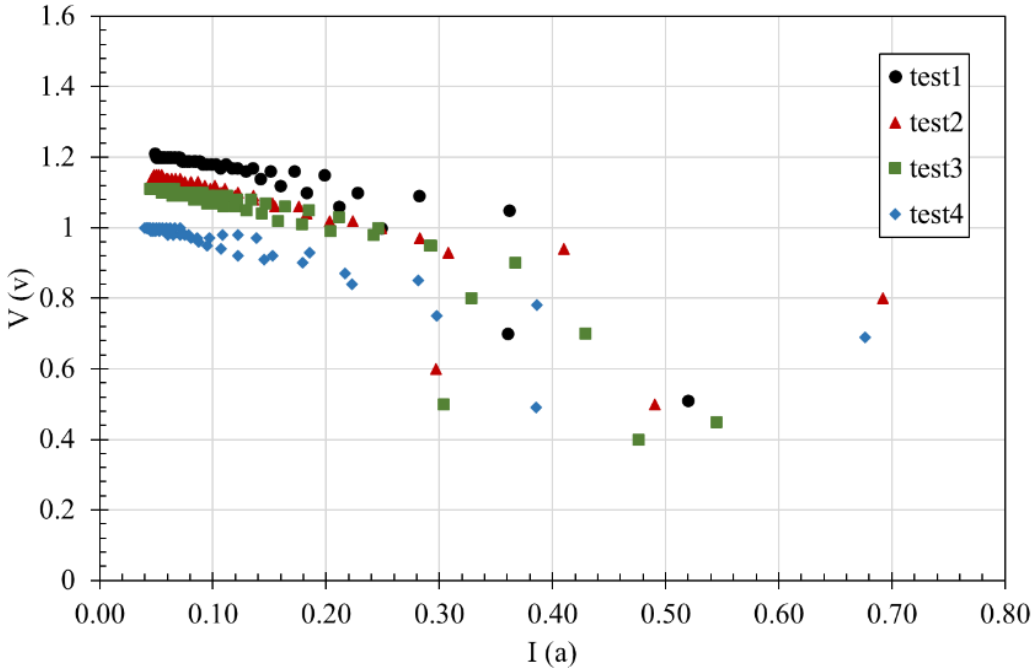

Figure 12, V-I Plot from experiment 8

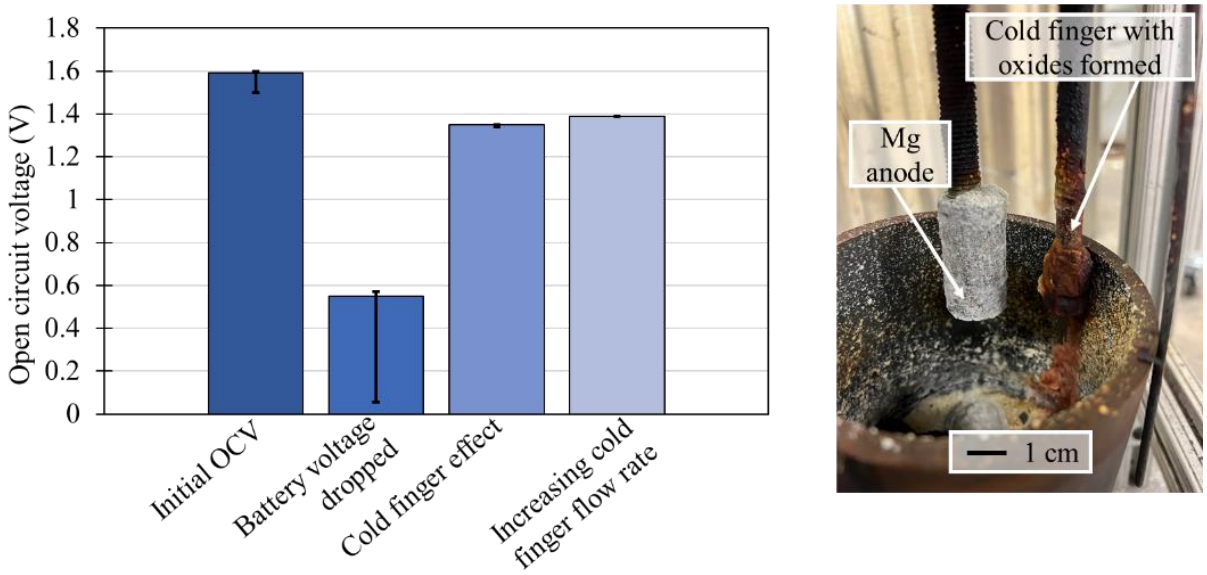

Figure 13, left) Voltage drop and recovery in experiment 8 showing the effect of the cold finger. Right) Cold finger after the experiment showing the oxides formed on it

4.2 Experiment 9

The effect of the cold finger was again verified in experiment 9. Starting from this experiment, a desiccant air dryer was used on the way of the cathode in flow to ensure low humidity of inserted air as shown in Figure 14. Results from this experiment are aligned with the results from the prior experiment. Maximum OCV at the initiation of this experiment was 1.26 V. As shown in Figure 15, the cold finger was started after the drop in the OCV which resulted in increasing the OCV back to 1.1 V. The use of a cold finger has also resulted in more stability of the voltage and fewer fluctuations as shown in Figure 16.

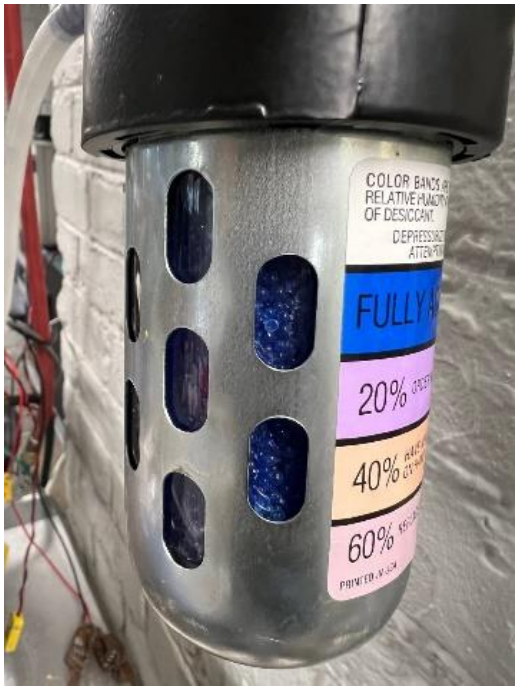

Figure 14, Desiccant air dryer used in experiment 9

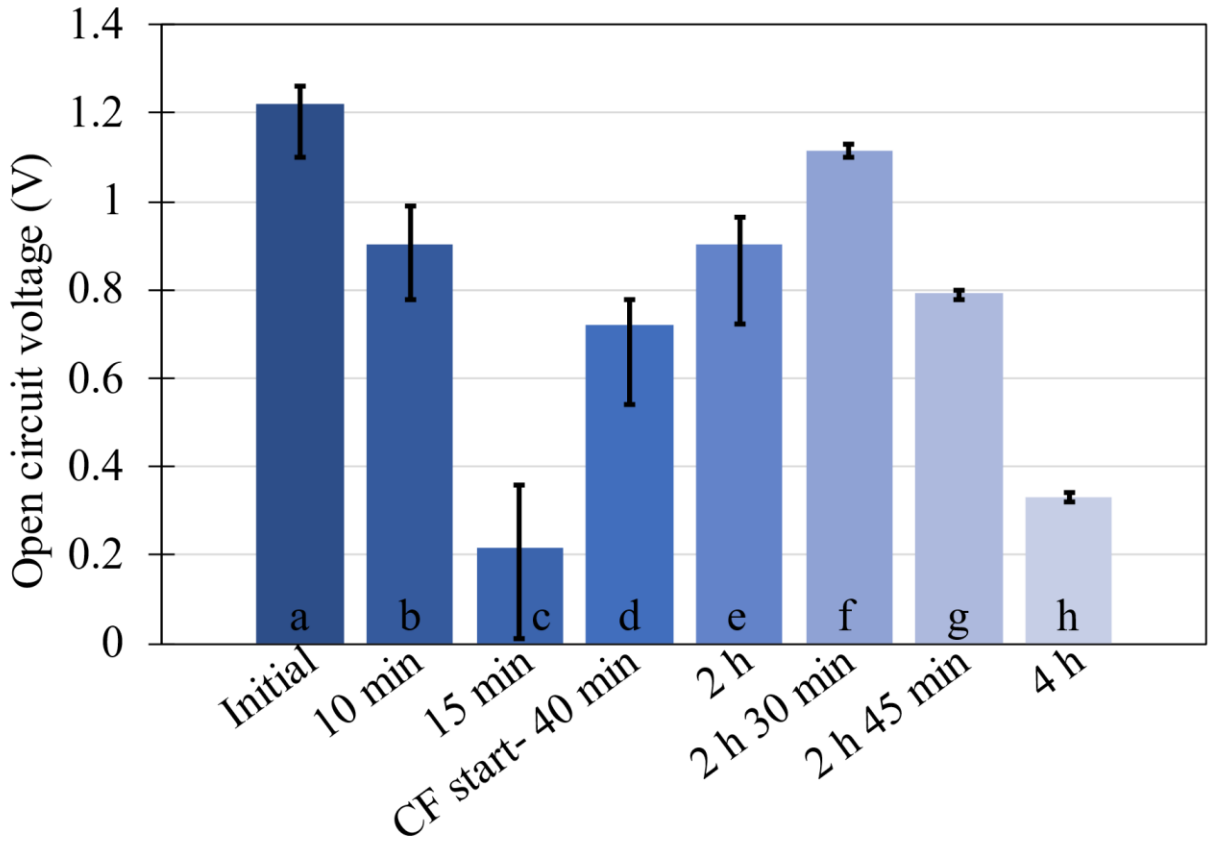

Figure 15, Effect of cold finger on OCV in experiment 9

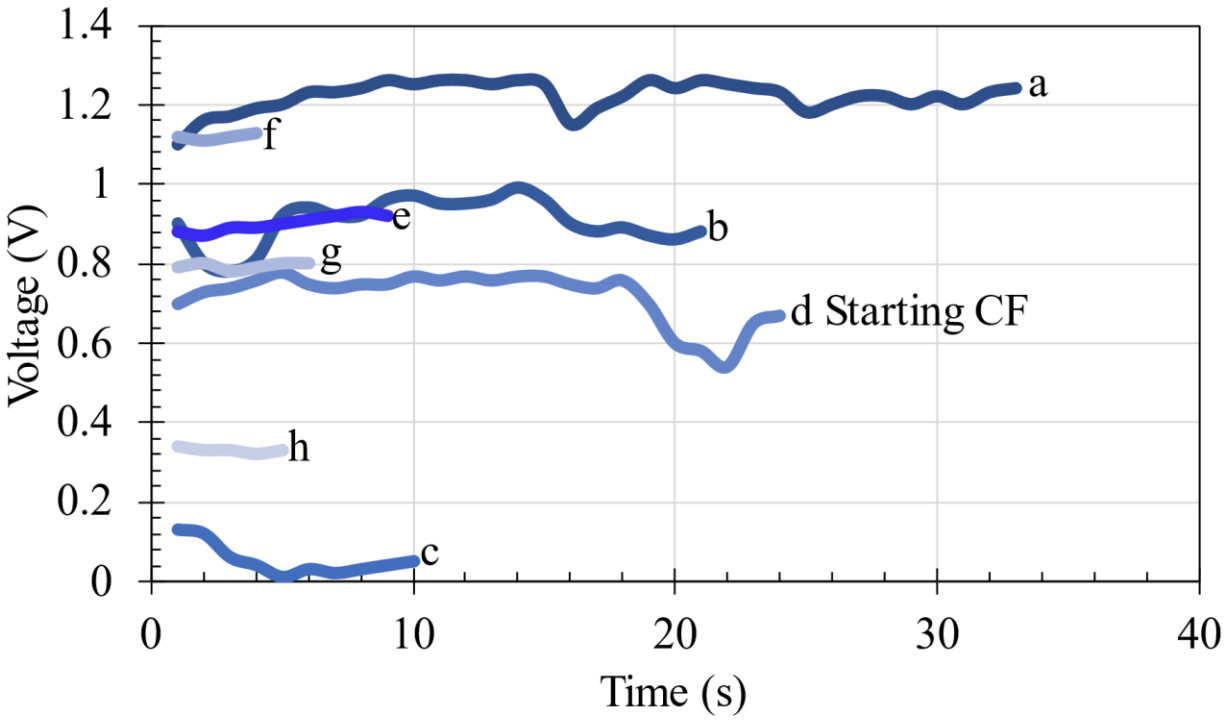

Figure 16, Effect of cold finger on OCV fluctuations in experiment 9

4.3 Experiment 10

In experiment 10, we planned to study how the voltage change when inserting the cold finger. Figure 17 from this experiment shows the changes in OCV from the insertion of the cold finger. Starting OCV in this experiment was 1.17 V but dropped shortly after the initiation of the test. Right after inserting the cold finger the OCV which was decreased to 0.67 V starts to increase gradually and then suddenly reached 1.08 V. The OCV stayed stable during this test and the test ended after 42 minutes. One of the most important results of this experiment was that the top plate and the anode are not isolated from one another. As a result of this, there was a high voltage of 1.6 V between the cathode and the top plate. To overcome this issue, an isolating tube was placed around the cathode in the following experiment.

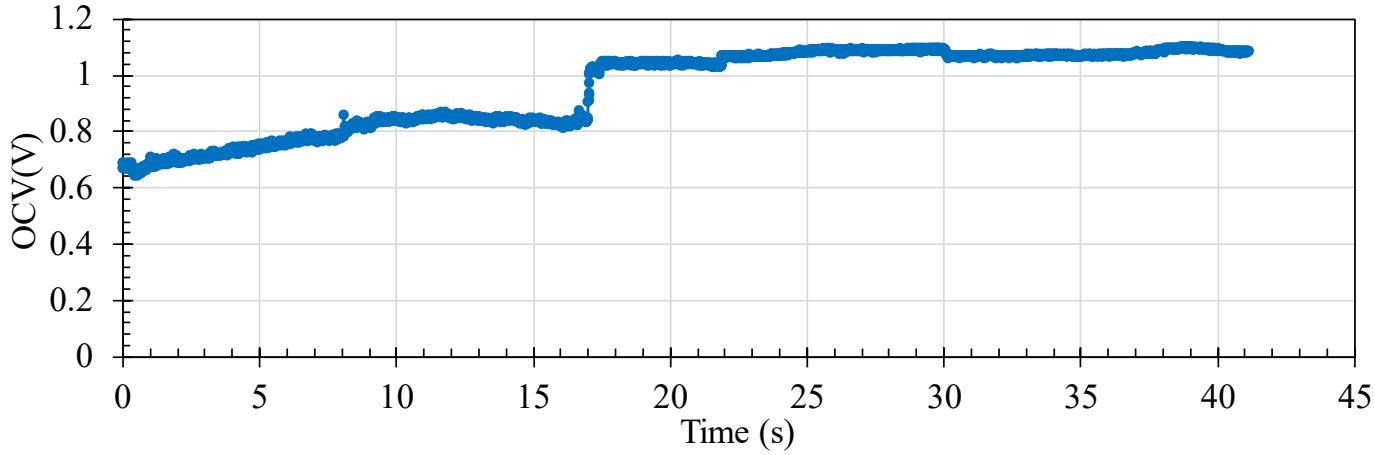

Figure 17, OCV during insertion of the cold finger in experiment 10

4.4 Experiment 11

As mentioned in the previous experiment, the purpose of experiment 11 was to ensure the isolation of the cathode from the top plate. To do so, two ceramic plates were placed under the crucible to isolate it from the cage. Moreover, a plastic tube was placed around the cathode to isolate it from the top plate. The highest OCV in this experiment was 1.23 V however the voltage between the cathode and the top plate was still 1.4 V. This showed that the isolation was not complete in this setup. After finishing the test and analyzing the setup it was found that the isolation tube around the cathode was placed too low and melted away during the high temperature. This is shown in Figure 18 along with the isolating ceramics that were put under the crucible. The two main conclusions from this experiment were to place the cathode isolating tube higher in the setup and to isolate the furnace tube by applying tapes on the four pieces holding it. In this experiment, the Mg was weighed before and after the experiment. It was 43.6 and 43.9 gr respectively. The 43.9 gr is the weight of the remaining Mg along with the oxidations formed on it. In the following experiments, the Mg was put into a solution to dissolve the oxides from it so that the weight of the Mg dissolved throughout the discharge is found.

Figure 18, Left) Isolating ceramics Right) The experimental cage after experiment 11

4.5 Experiment 12

Experiment 12 was the first long-run experiment on the Mg-air battery. In this experiment, the battery was discharged for 6h. Isolations were adjusted so that the cathode isolation is not melted, the ceramic plates are placed under the crucible and the furnace tube is isolated from the rest of the setup. To avoid the interaction of the stainless-steel threaded rod with the molten salt the Mg anode was not inserted into the molten salt. This is shown in Figure 19. Another difference between this experiment and the previous ones was that the salts were not pre-baked before the test. Instead, they were placed in the furnace and the furnace was heated up and stayed at 300 ^{o}C for three hours to make sure all the humidity leave the salts. The highest OCV in this experiment was 1.224 V and the results are shown in Figure 20. This experiment started with a high fluctuation within the battery voltage. Twelve minutes into the experiment the cold finger (CF) was inserted into the salt and the CF flow was started. About fifty minutes into the test, the voltage suddenly drops but started to recover to 1.2 V without any modifications. After about 1h there was another voltage drop which continued with voltage fluctuation and the voltage was dropped and stabilized at 0.02 V after that. Although this was not a successful long-run experiment there were important findings based on this experiment. To start with the cold finger flow was not open at the beginning of the test and was turned on when it was inserted into the molten salt. This means, as opposed to the previous experiments, the cold finger was not as cool as it can get to solidify the MgO formed in the molten chloride. Another point is that the cold finger was previously used in another experiment. This means that it might have not been as heat

conductive as a new one because it had oxidations formed on it. Moreover, not having the cold finger working as expected, there are salts built up on the cathode and at the bottom of it that blocks the oxygen air inlet. As shown in Figure 21, the cathode was fully blocked after the test and there are salts formed on the cathode tube. This can be the reason behind the two drops in the voltage. With minimal oxygen flow into the system, the voltage significantly dropped in the experiment after three hours of operation.

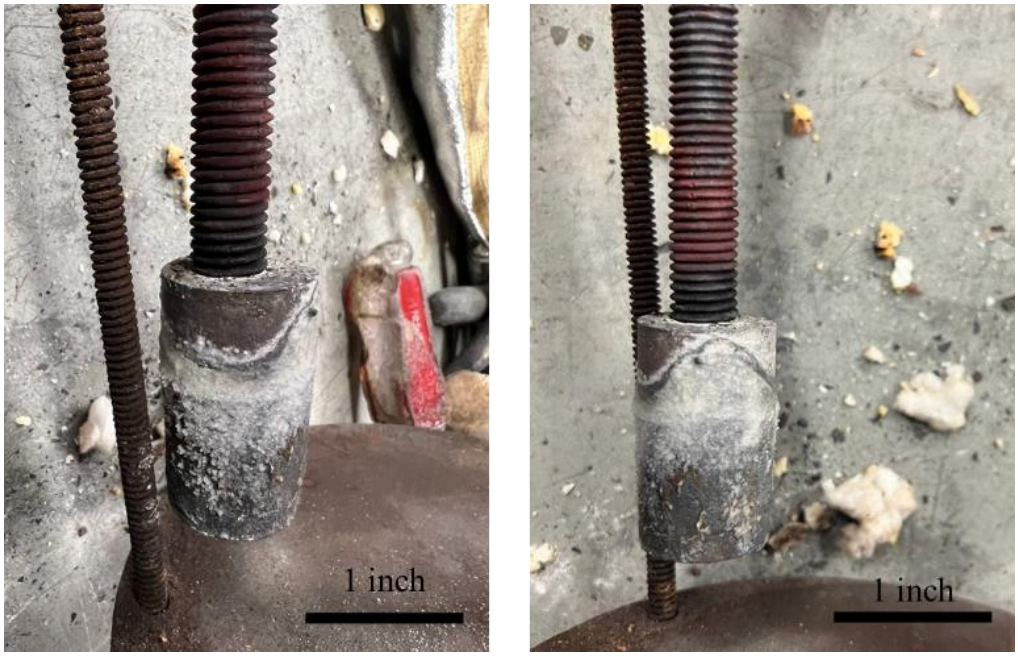

Figure 19, Mg anode after experiment 12, showing the dissolved Mg and the oxides formed on it

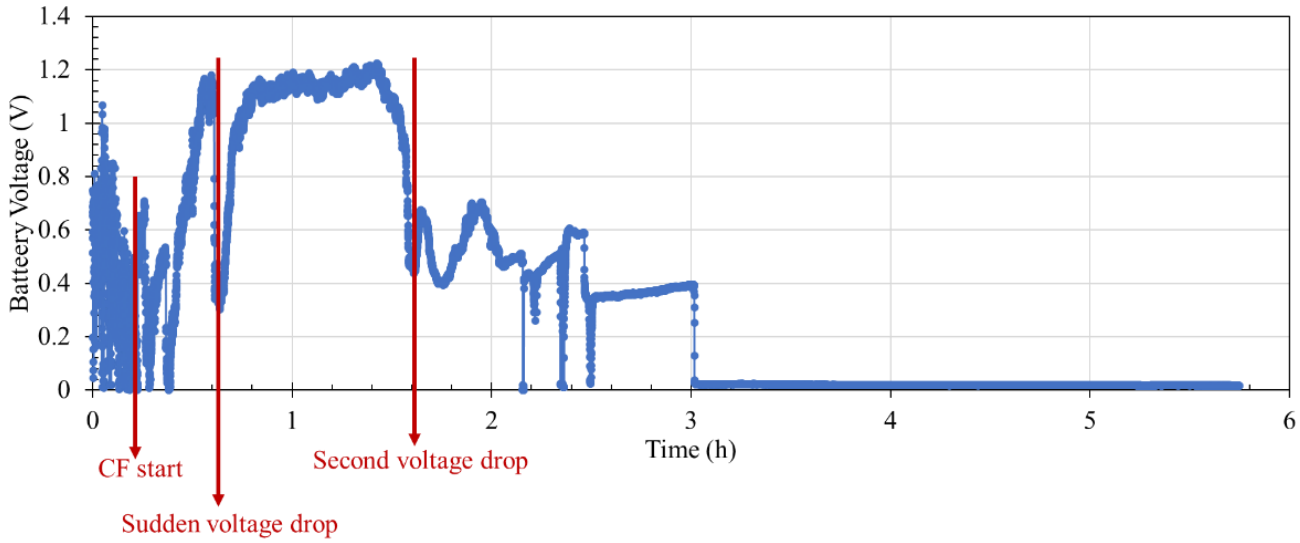

Figure 20, Battery voltage in experiment 12

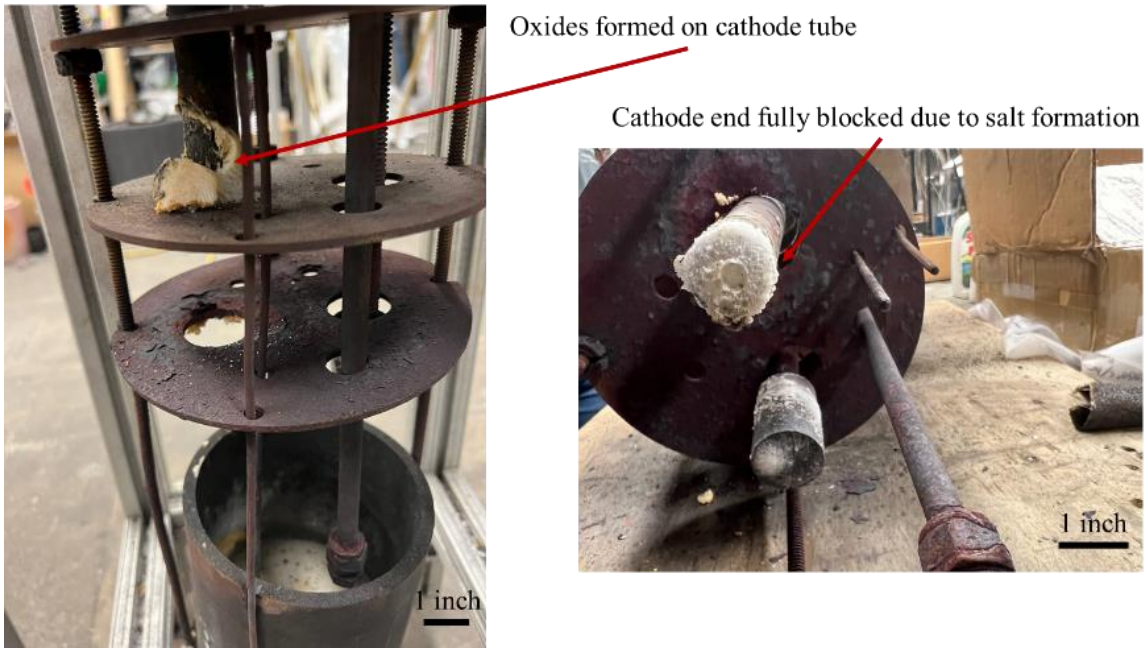

Figure 21, Left) Experimental cage after the experiment, Right) Cathode and anode after the experiment showing the blocked cathode due to deposition of salts on the cathode's outlet

4.6 Experiment 13

In the thirteenth experiment, we aimed to repeat the long-run experiment and measure OCV for more than 10h. Due to the misprogramming of the furnace, the furnace temperature started to go beyond 550 to 800^{o}C almost 8 hours into the experiment as shown in Figure 22. Although the results beyond this time are not useful for the analysis of this study, they can be used for the safety management of these cells. The cell ran at 800^{o}C for more than two hours. During this time there was a high increase in the OCV of the cell which shows that the last bit of Mg was used up. After this time the cell was cooled down and opened for studying. This unexpected increase in the temperature did not cause a safety problem. The Mg was completely evaporated and the thermal shock within the cold finger made it break as shown in Figure 23. This shows that if for any reason there is an overheat in the battery, its functionality of it will be negatively affected but this will not result in a health hazard.

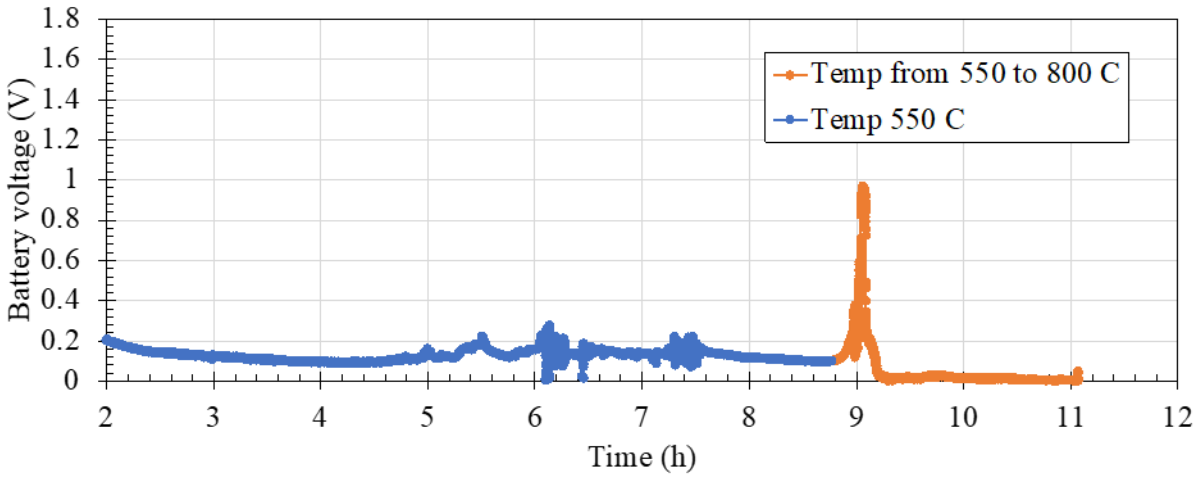

Figure 22, Battery voltage during discharge and higher than normal temperature in experiment 13

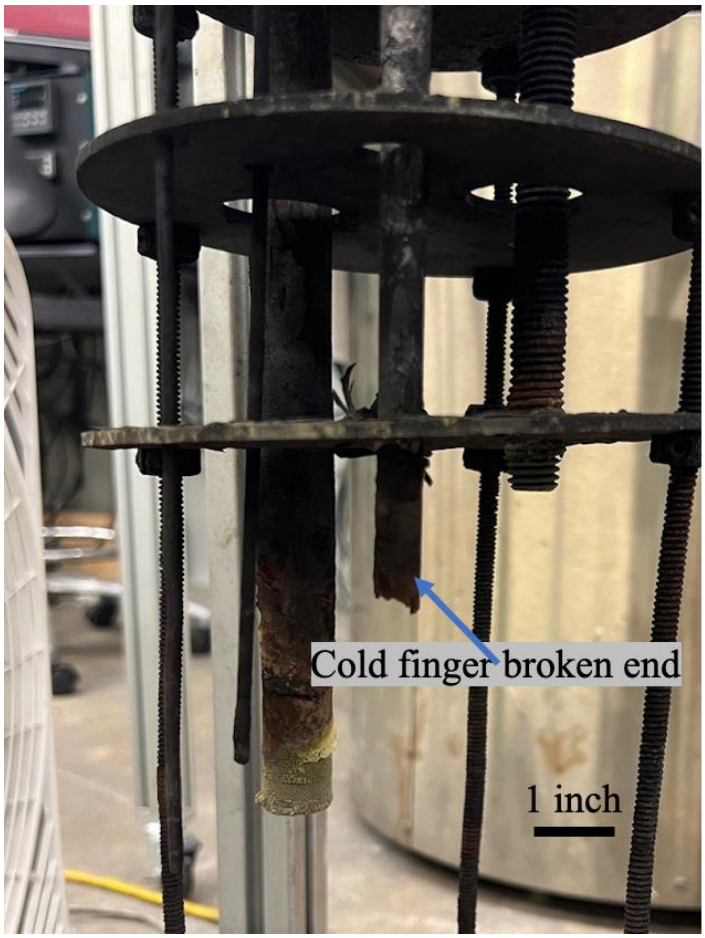

Figure 23, Higher than normal temperature in experiment 13 broke the cold finger

4.7 Experiment 14

In a similar experiment, Exp 14, the cathode inlet tube popped off, and therefore cathode flow was stopped. This caused the battery voltage to reach almost zero. When the cathode flow was reconnected, the battery voltage was back to 1.1 V as shown in Figure 24.

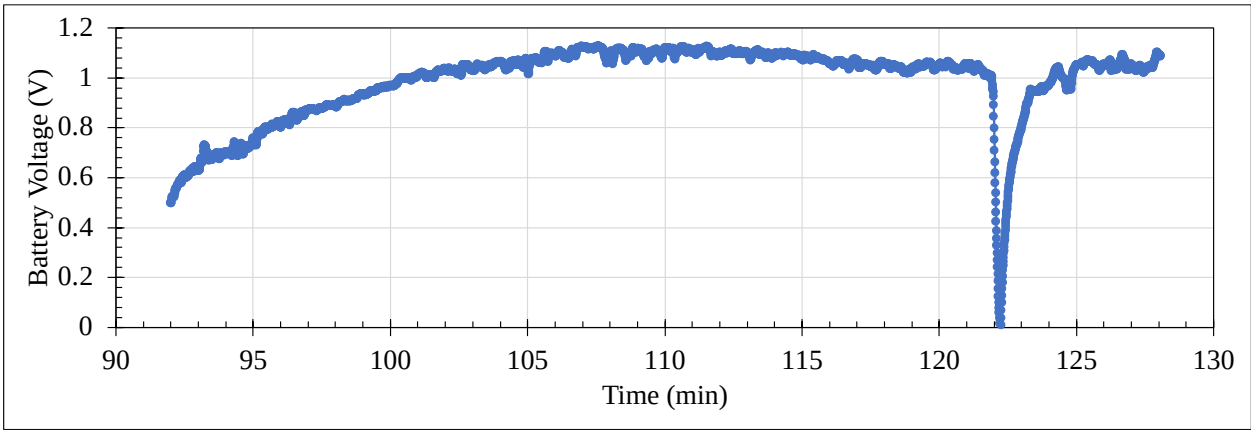

Figure 24, Battery voltage during experiment 14

4.8 Experiment 15

A similar approach was taken for the next experiment. To study the cathode flow the cathode end was cut off and mounted in the epoxy after the experiment. It was then cut in half across its length as shown in Figure 25. Based on this photo, the Nickel mesh is only blocked at the bottom and its pores are empty in the center. This shows there is a great seal between the Ni mesh and the stainless tube so that the cathode air passes through the Ni mesh and not around it.

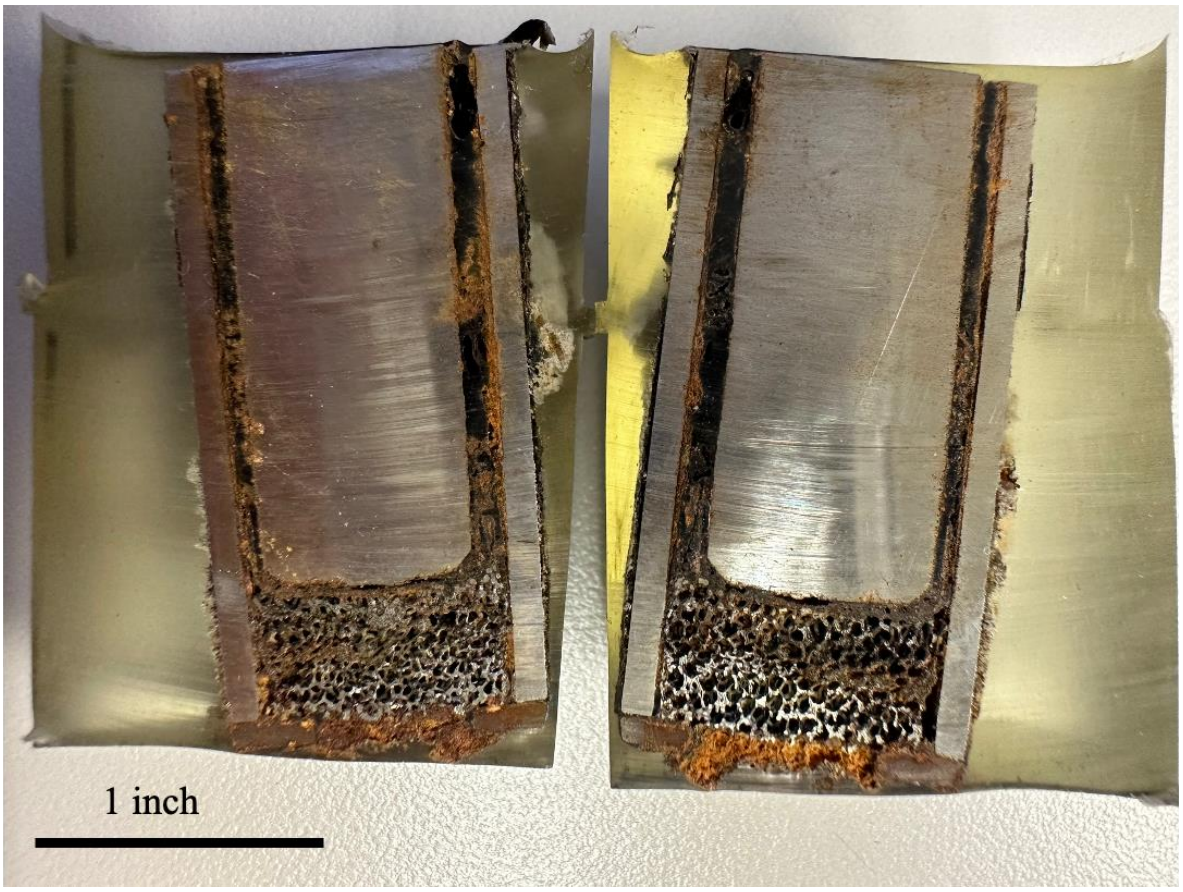

Figure 25, Cathode cross-section view after experiment 15, the cathode porosity looks intact and the blockage is seen at the outlet of the cathode

4.9 Experiment16

The theoretical amount of electrical charge, or charge capacity, that can be generated by the reaction of 1 gram of Mg in an electrochemical cell depends on the specific conditions of the cell, such as the size and configuration of the electrodes, the type and concentration of the electrolyte, and the overall reaction that takes place.

Assuming a simple electrochemical cell where magnesium is the anode and copper is the cathode, and the half-reactions are:

$Mg \rightarrow Mg^{2+} + 2e^-$

$O^{2-} + 2e^- \rightarrow 0.5O_2$

The theoretical charge capacity of this cell can be calculated as follows:

Determine the number of moles of Mg in 1 gram of Mg by dividing the mass of Mg by its molar mass:
moles of Mg = 1 g / 24.31 g/mol = 0.041 mol

Calculate the number of electrons transferred in the reaction, which is equal to the number of moles of Mg multiplied by the number of electrons transferred in the half-reaction (2 electrons per Mg atom):

number of electrons = 0.041 mol Mg x 2 electrons/mol = 0.082 C

Calculate the charge capacity of the cell, which is equal to the number of electrons transferred multiplied by the Faraday constant (96,485 C/mol):
charge capacity = 0.082 C x 96,485 C/mol = 7,922 C

Therefore, the theoretical charge capacity of this cell would be 7,922 Coulombs (C), which is equivalent to 7,922 ampere-seconds (A.s) or 2.2 ampere-hours (Ah) of electricity. However, in reality, the actual amount of electrical charge that can be obtained from this reaction will be lower due to losses from resistance, side reactions, and other factors.

One of the important aspects of this battery is to achieve high OCV. One reason that can decrease OCV is the water content in the cell. Although the air desiccant is used to dry out the inlet air in the experiment, in experiment 16, an extra step was taken. Here 50 grams of ammonia chloride was added to the salt mixture. Ammonia chloride will react with humidity and reduce it in the cell. As shown in Figure 26, the highest OCV has reached 1.815 V which is 61% higher

than our general Max OCV from the previous test (1.2 V). Two hours into the test three resistance sweeps were done as shown in Figure 27. Evan's diagram based on these sweeps is shown in Figure 28. Based on this figure, the highest voltage of these plots reduce after each sweep.

A side effect of using Ammonia chloride in our salt is that the whole furnace tube and all its components become coated in Ammonia chloride. This will make the gas outlet partially blocked and the clean-up process longer.

The Mg sample after the experiment was studied under the SEM and the results are shown in Figure 30. The Au shown as one of the elements in this study comes from the sputter coating which uses Au and Pd.

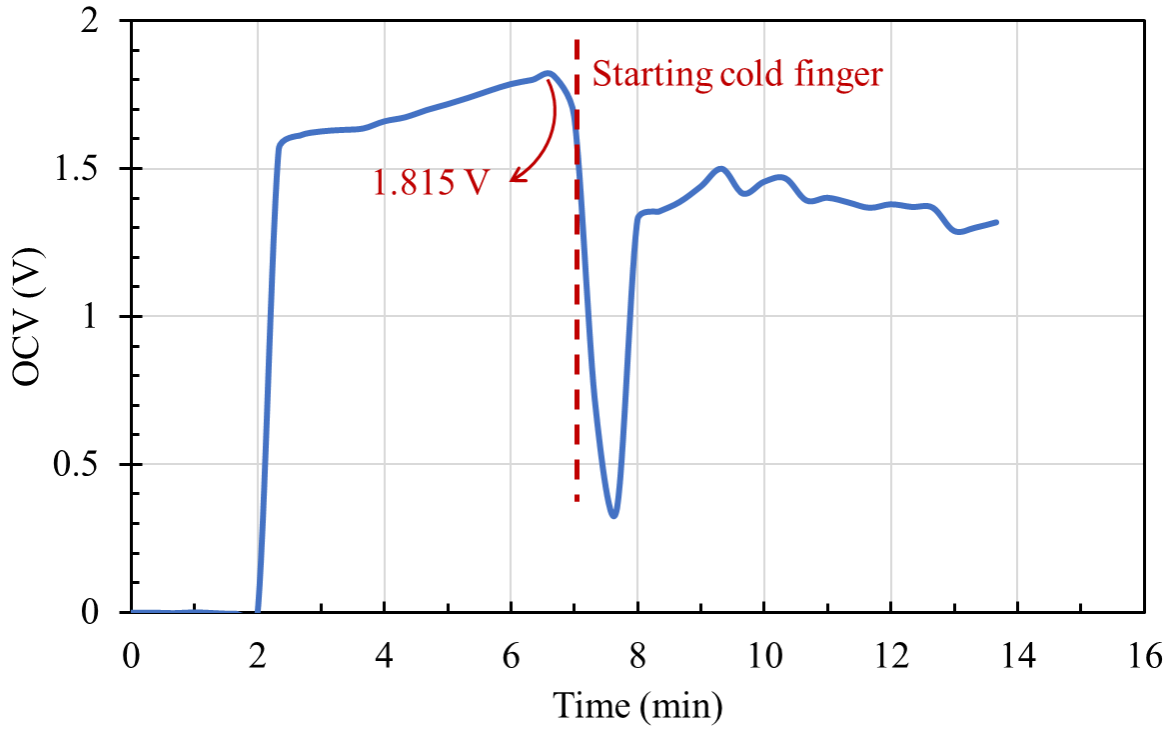

Figure 26, OCV at the start of experiment 16

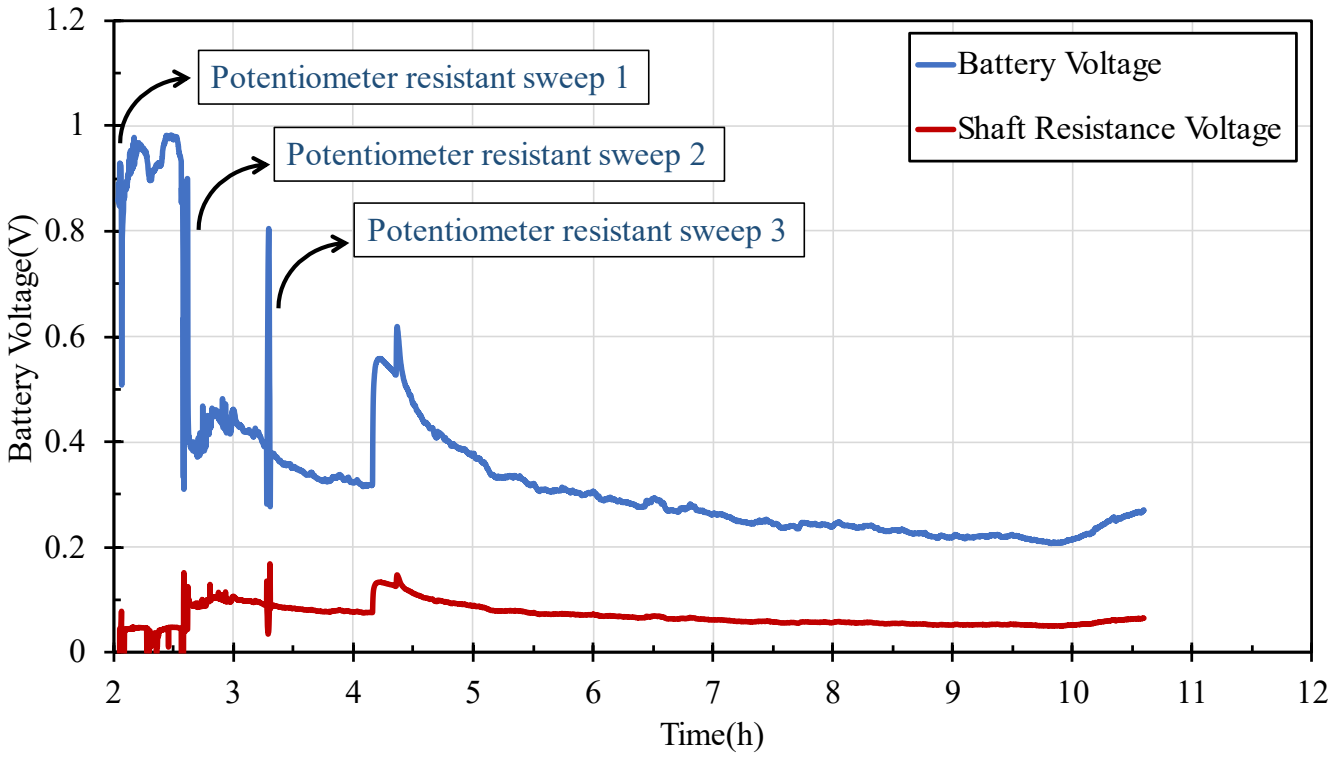

Figure 27, Battery voltage in experiment 16 showing three resistance sweeps in this experiment

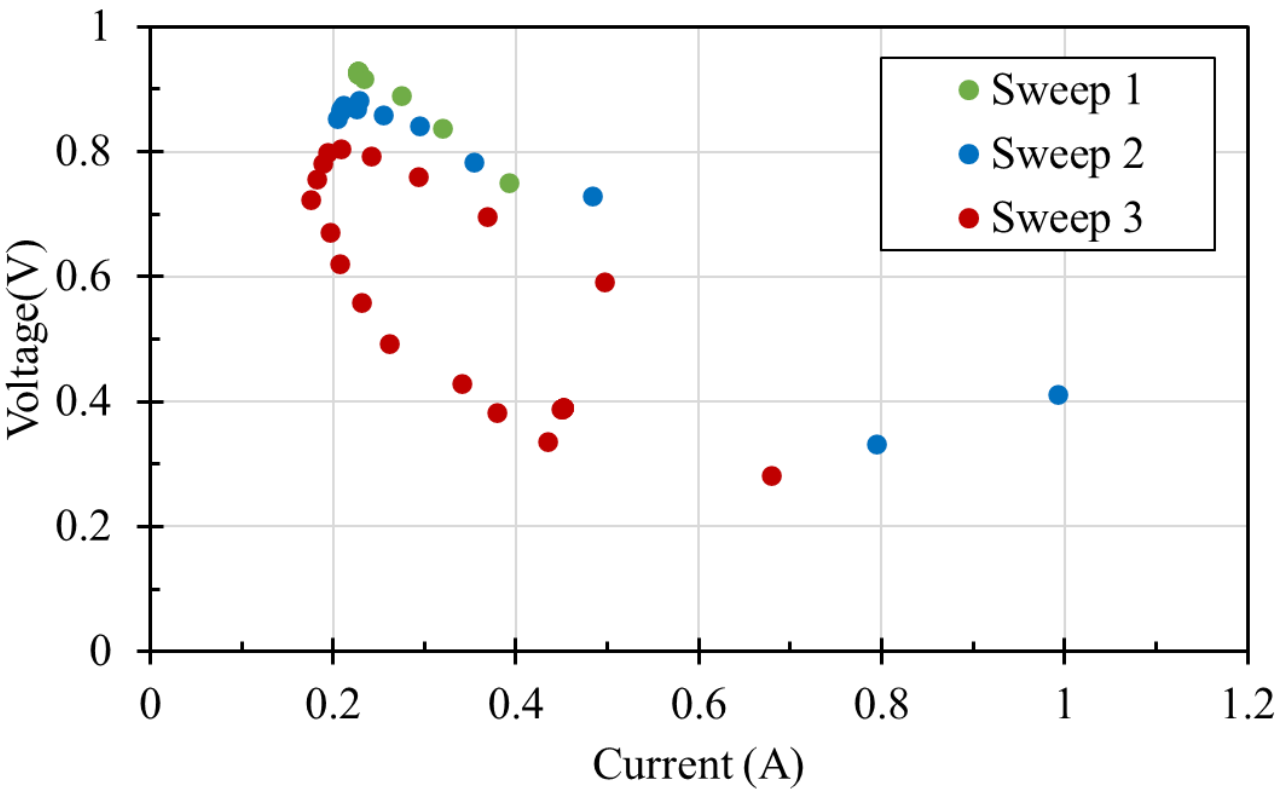

Figure 28, V-I Plot from experiment 16 from the three sweeps

Figure 29, Furnace door from the inside after experiment 16 showing the ammonia chloride deposited around the furnace wall from inside

EDS Layered Image 7

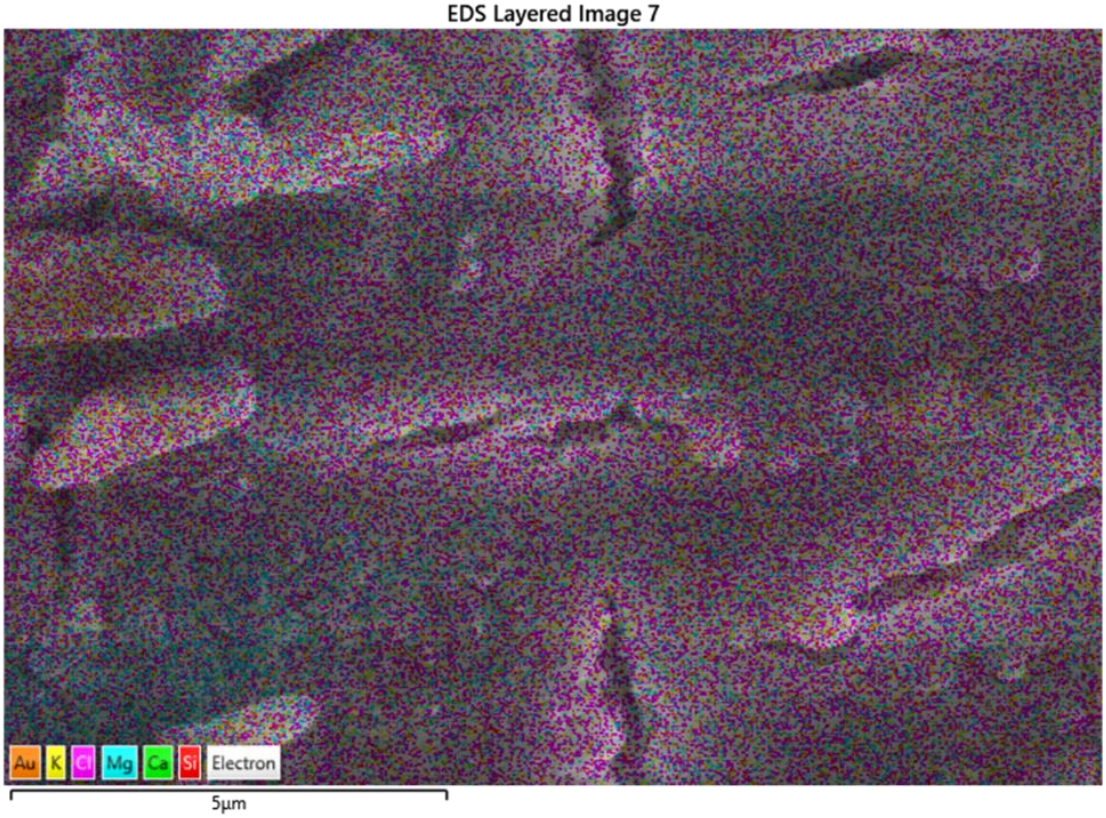

Cl Kα1

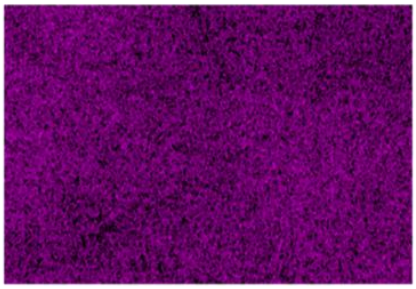

Mg Kα1,2

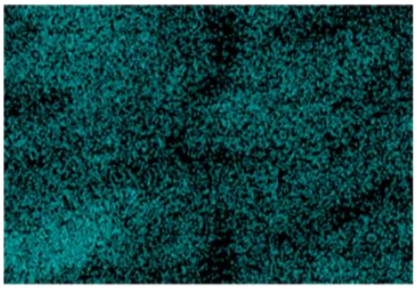

K Kα1

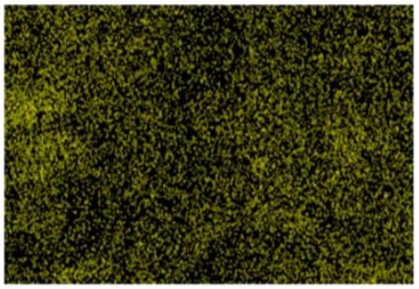

Au Mα1

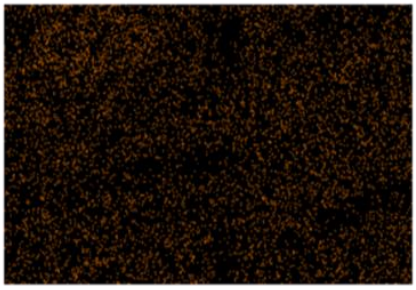

Si Kα1

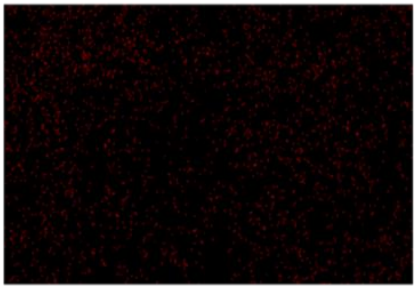

Ca Kα1

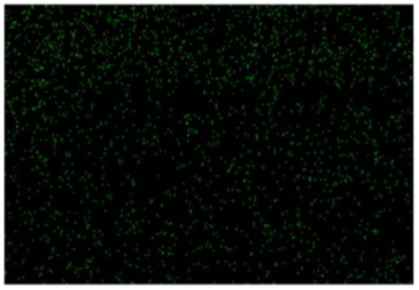

Figure 30, SEM image of deposited material on the Mg showing that it mostly consists of the salts

The current over time in this experiment is shown in Figure 31. The average current can be estimated as 0.4 A and the operating time is 8.5h which gives us 3.4 Ah energy. As shown in Figure 32 about 5.7 of Mg has turned into MgO during the test which results in 60% current efficiency for this cell.

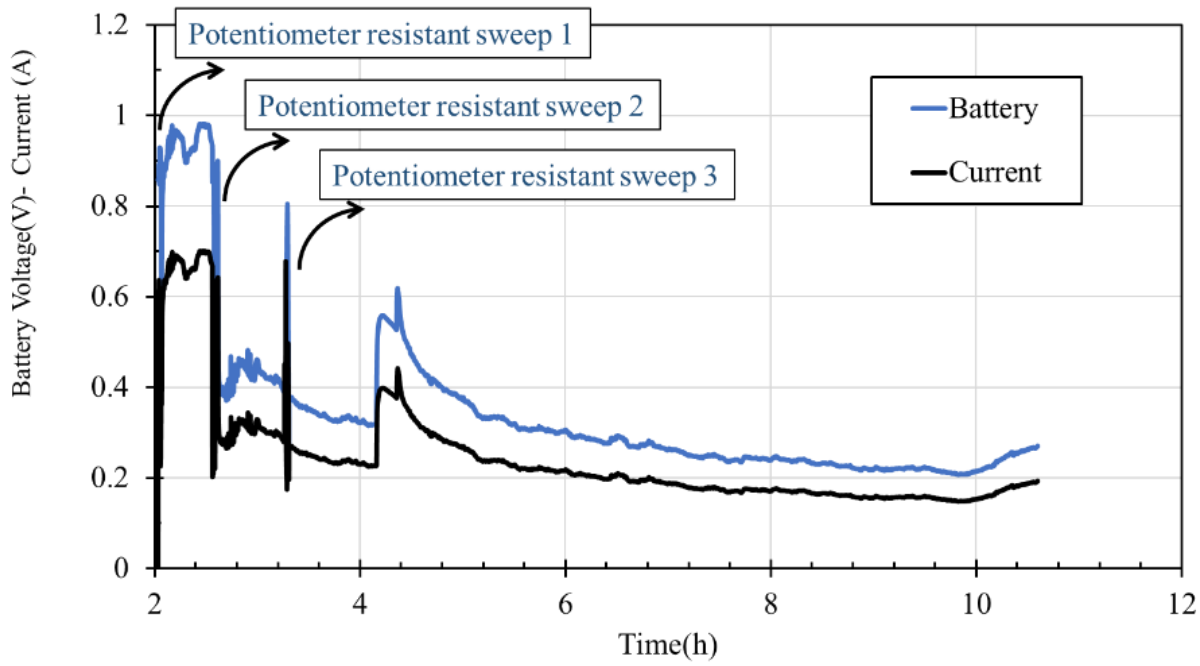

Figure 31, Voltage and current of the battery during discharge and sweeps in experiment 16

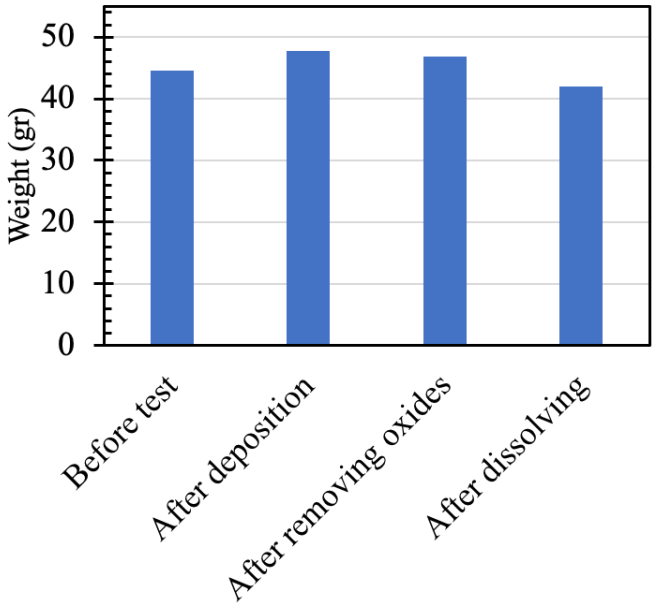

Figure 32, The weight of the Mg anode before and after the experiment, after physical removal after the oxides and after dissolving the oxides to calculate the amount of the Mg dissolved

Chapter 5- Long Run Experiments

5.1Experiment 17-first long run

In experiment 17, we aimed for a very long run to study the battery performance for over 30 h. We started the test at 8 am and finished it at 5 PM of the following day. During this time, the resistance sweep was studied almost every hour. Each time two sweeps were run, one using two 0.2 ohm resistors and the other using two 0.02 ohm resistors.

Ammonia chloride was again used in the salts for this experiment, resulting in almost full blockage of the outlet tube. This is shown in Figure 33 along with the huge solidified component of the cold finger and the cathode.

The highest OCV in this experiment was 1.31 V and the battery voltage for the first 22 mins of the experiment is shown in Figure 34.

Figure 35 shows all the sweeps in this experiment and Figure 36 shows three of the sweeps at a time for different times. Based on these figures the voltage for these sweeps generally decreased over time.

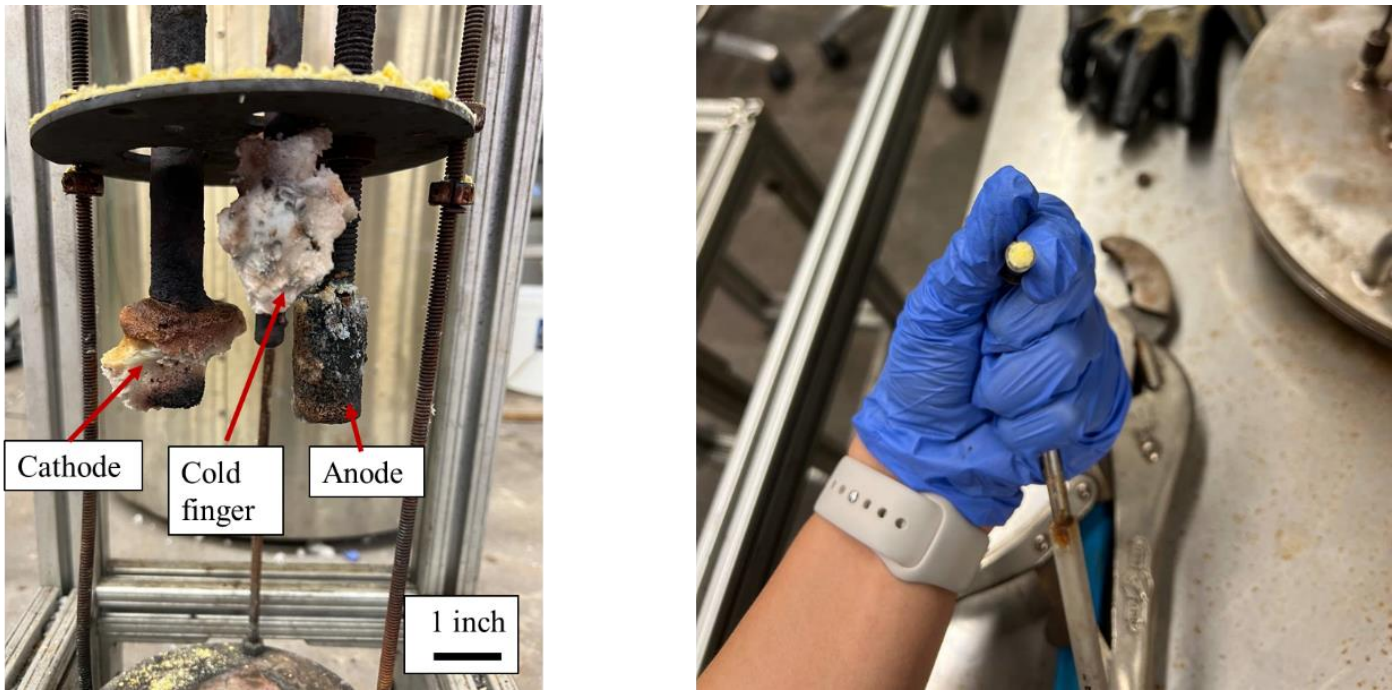

Figure 33, Right) The cage after the long discharge of experiment 17, showing the huge solidified component formed on the cold finger as well as the cathode Left) the gas outlet pipe of the furnace was blocked as a result of using ammonia chloride

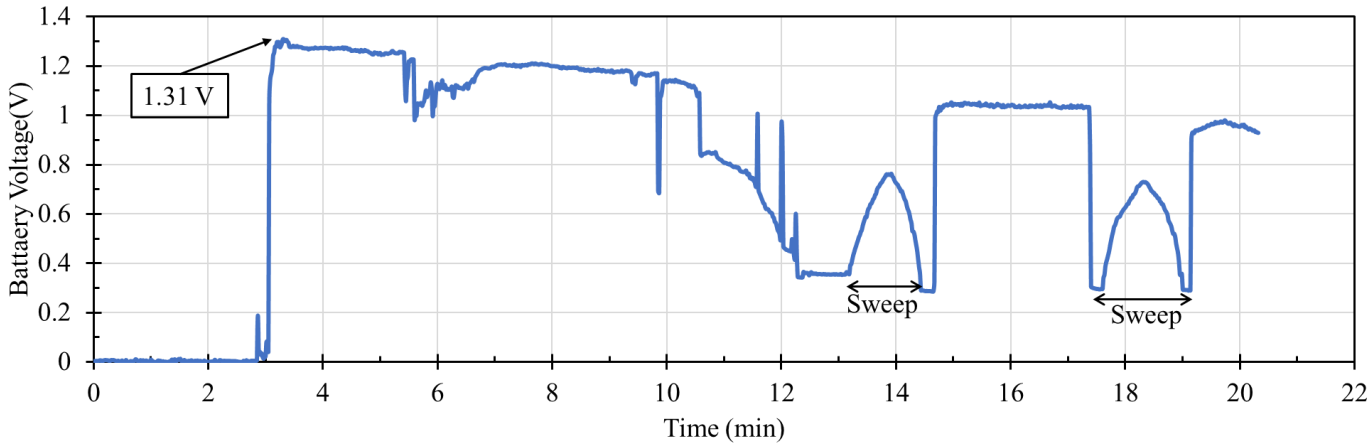

Figure 34, The battery voltage during the long discharge in experiment 17

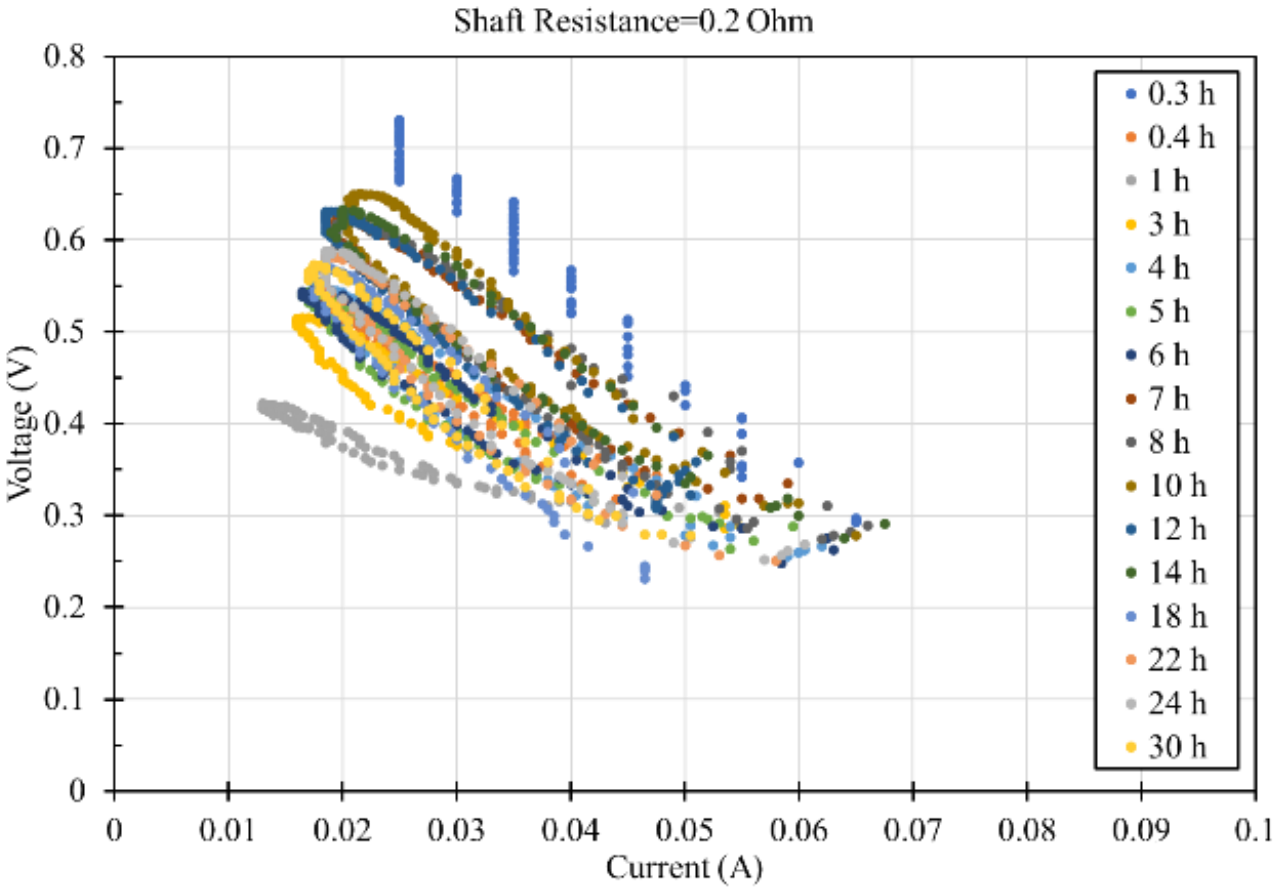

Figure 35, Sixteen V-I Plot from experiment 17

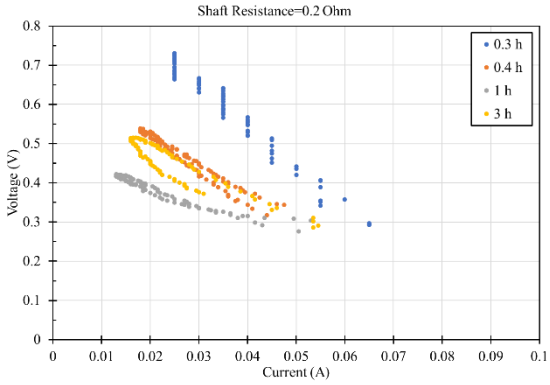

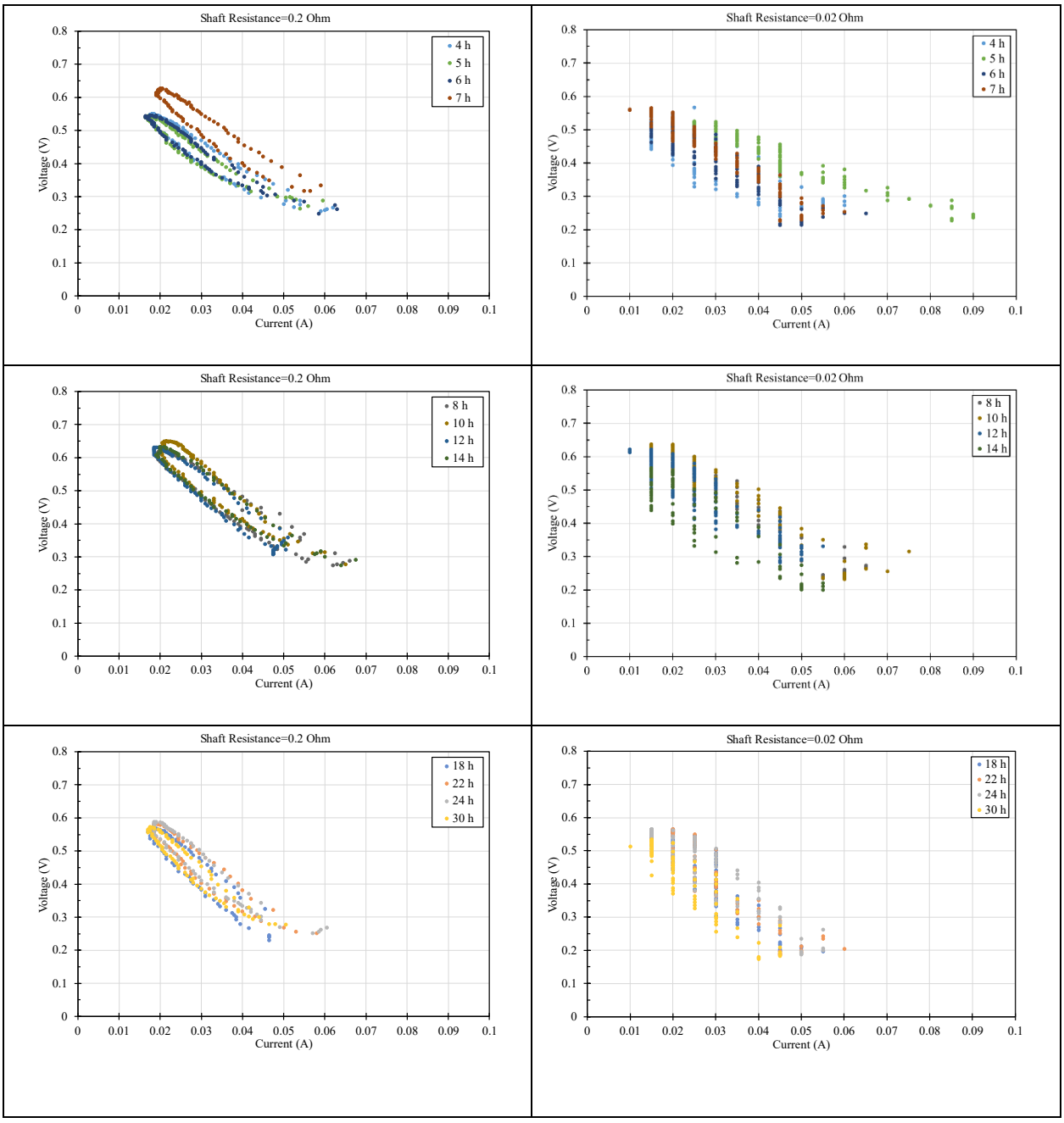

Figure 36, Sixteen V-I Plot from experiment 17 from the three sweeps plotted separately

As shown in Figure 37, the average current in this experiment was about 0.15A with 30 h operation time. As shown in Figure 38, 3.1 gr of Mg has dissolved in this experiment which

results in 6.82 Ah energy. Using this information the current efficiency of the cell can be estimated as 66%.

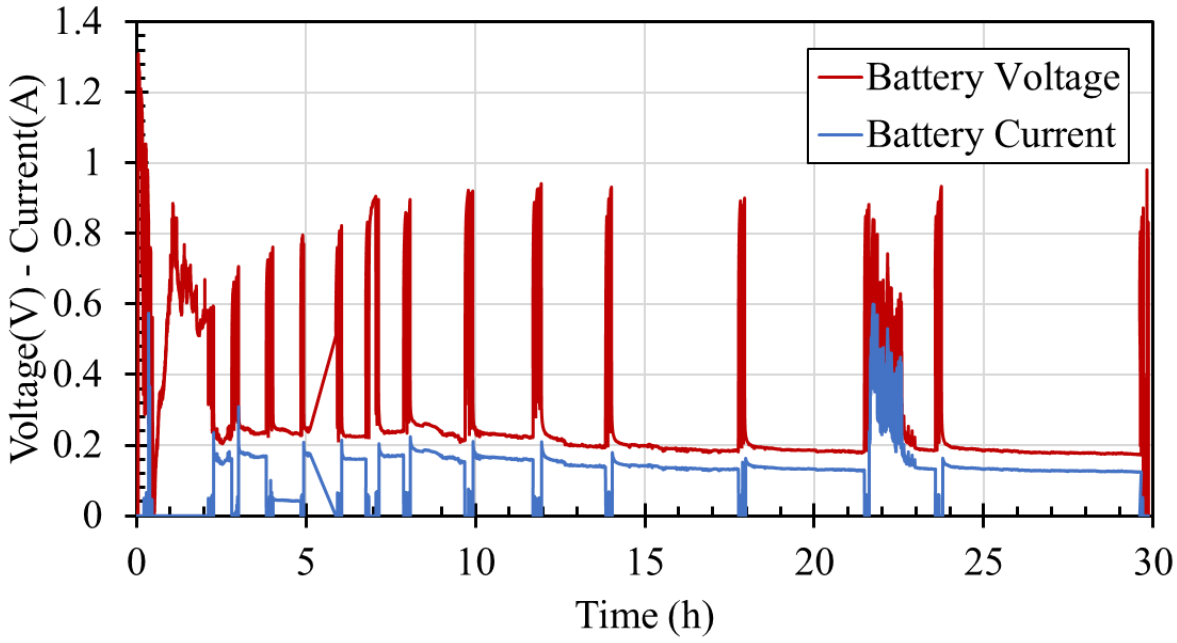

Figure 37, Voltage and Current plot in experiment 17 showing multiple sweeps

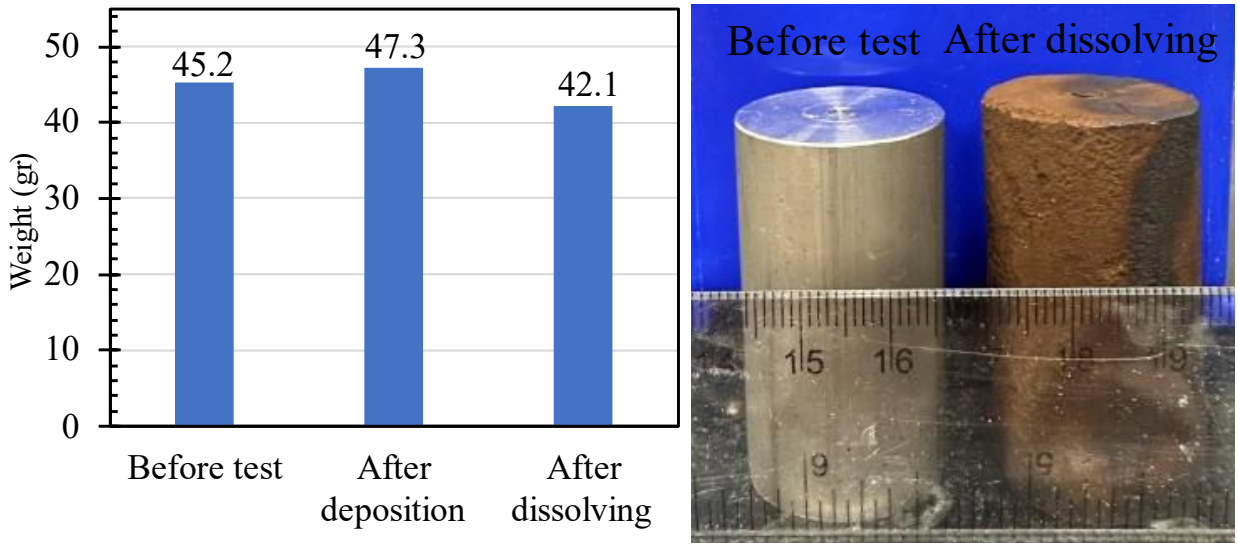

Figure 38, Left) The weight of the Mg before and after the experiment and after dissolving the oxides in the solution Right) showing a piece of Mg before the experiment, and another one after the experiment and dissolving the oxides away

Chapter 6- Rechargeability

6.1 Experiment 18

It is important to note that during the recharging of this cell, O_2 is not produced because it needs a Platinum electrode. Platinum is a widely used material for the construction of electrodes in various electrochemical processes, including the production of oxygen. There are a few reasons why platinum is a good choice for this purpose:

- Catalytic activity: Platinum is an excellent catalyst for the electrochemical reaction that produces oxygen. A catalyst is a substance that increases the rate of a chemical reaction without being consumed in the process. Platinum's unique electronic and crystal structure properties make it highly efficient in catalyzing the reaction that produces oxygen.

- Stability: Platinum is a highly stable material, even at high temperatures and in the presence of corrosive environments. This makes it an ideal choice for use as an electrode in high-temperature and high-pressure electrochemical cells used to produce oxygen.

- Conductivity: Platinum is an excellent conductor of electricity. This property is essential for ensuring efficient electron transfer during the oxygen production process.

In summary, platinum is a good choice for an electrode in the production of oxygen due to its excellent catalytic activity, stability, and conductivity but it is out of the scope of these experiments.

Experiment 18 was the first recharging experiment in this project. For the recharging experiment, the battery was set up as normal and set to run for 13 h as shown in Figure 39. After that, the

cold finger and cathode flow were shut off. The battery leads were then connected to the power supply so that the Stainless steel/Ni is the positive and Mg is the negative lead. Then the sweeps were started by applying voltage from 0 to 5V over 10 mins which means 0.1 V every 12 seconds. The current was then set to 0 and OCV and measured for 10 mins. Then the electrolysis was started by running the system at a constant voltage of 2V for 30 mins. This was for the impurities to leave the Mg surface so more pure Mg can be deposited at the next electrolysis. During this process, it was possible to dissolve/oxidize some of the components in stainless steel or Ni. After 10 mins of OCV measurement, another 0 to 5V sweep was done to give a more clean I-V plot as a result of reduced impurities. Next, another round of electrolysis was started at 4 V for one hour followed by a 10-minute OCV measurement. The test was then finished with another resistant sweep and 10 mins OCV recording. The results from the three sweeps are shown in Figure 40 which shows that the chromium in stainless steel is either turning into Cr_2O_3 or chromium ions.

- $MgO+Cr \rightarrow Cr_2O_3+Mg$ [forms Chromium oxide on the tube]
- $Mg^{2+}+Cr \rightarrow Mg+Cr^{2+/3+/4+}$ [Chromium ions dissolve in the salt]

The Mg was cut and studied under the SEM, and EDS. One study was on the cross-section of the Mg and the other on the lump shape formed on its edge as shown with red boxes in Figure 41. Figure 42 and Figure 43 show the EDS of the cross-section of the Mg in two different magnifications. Some high Mg regions of the size of a couple of microns show that the Mg dendrites were formed around the initial Mg anode. Figure 44 and Figure 45 show the EDS of the Mg lump in two different magnitudes. Here also Mg regions are seen which are significantly smaller and are on the order of 5 microns.

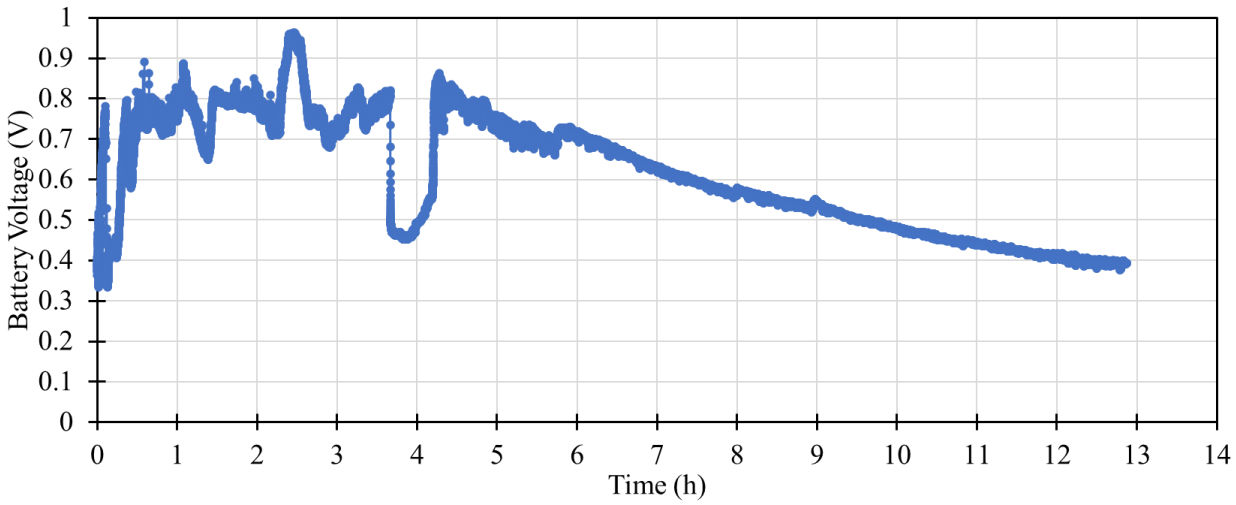

Figure 39, The battery voltage during discharge in experiment 18

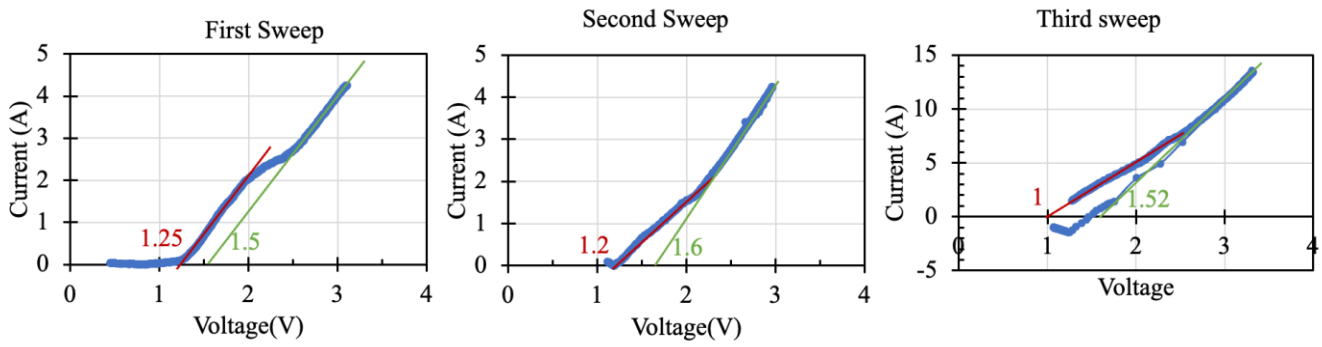

Figure 40, The three recharging sweeps in experiment 18

Table 3, Possible reaction happening during MAB recharging and their standard voltage

Reaction	***E*°** (V)
$Mg^{2+} + 2e^- \rightleftharpoons Mg(s)$	–2.356
$O_2\ (g) + e^- \rightleftharpoons O_2^-(aq)$	-0.33
$Fe^{2+} + 2e^- \rightleftharpoons\rightleftharpoons Fe(s)$	–0.44
$Fe^{3+} + 3e^- \rightleftharpoons\rightleftharpoons Fe(s)$	–0.037

$Fe^{3+} + e^- \rightleftharpoons Fe^{2+}$	0.771
$Cr^{3+} + e^- \rightleftharpoons Cr^{2+}$	–0.424
$Cr^{2+} + 2e^- \rightleftharpoons Cr(s)$	–0.90

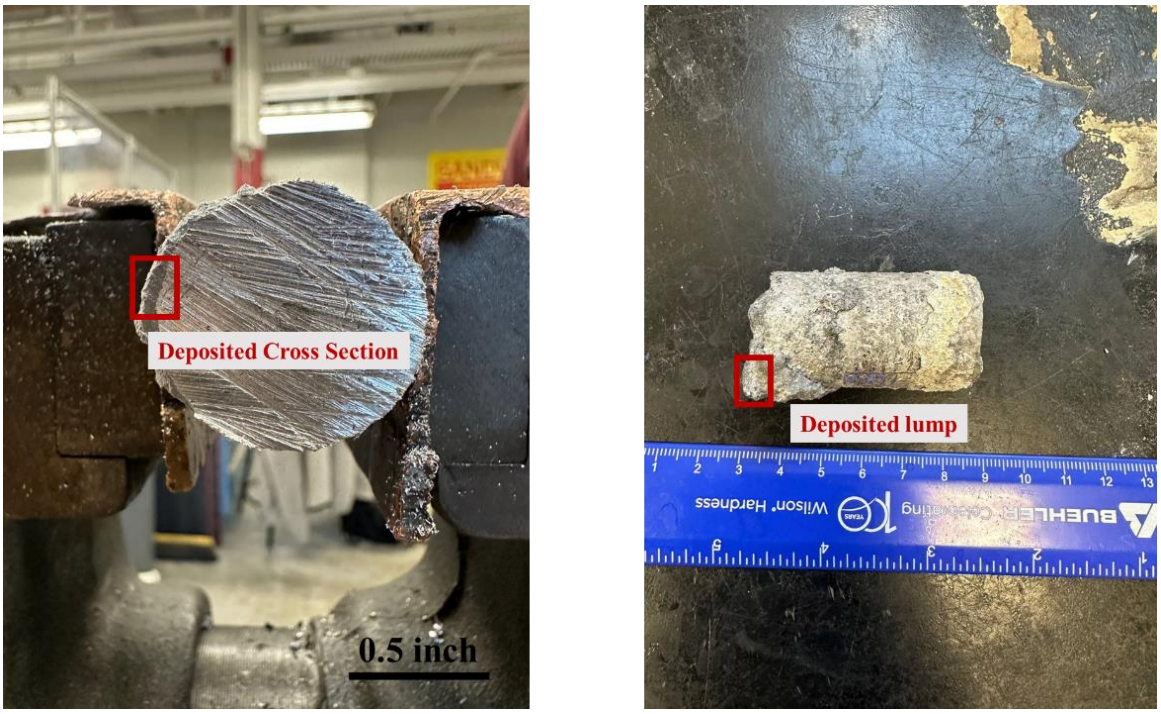

Figure 41, The Mg after recharging showing the cross section and deposited lump from experiment18

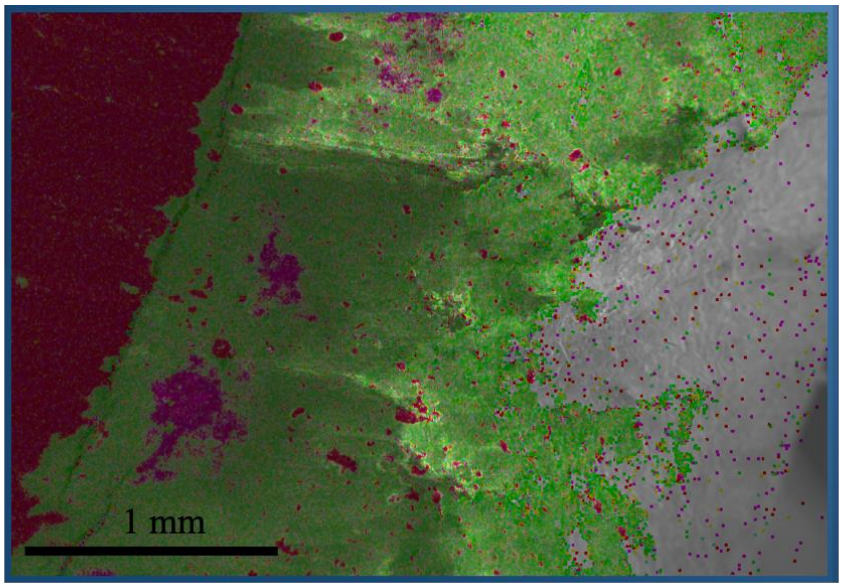

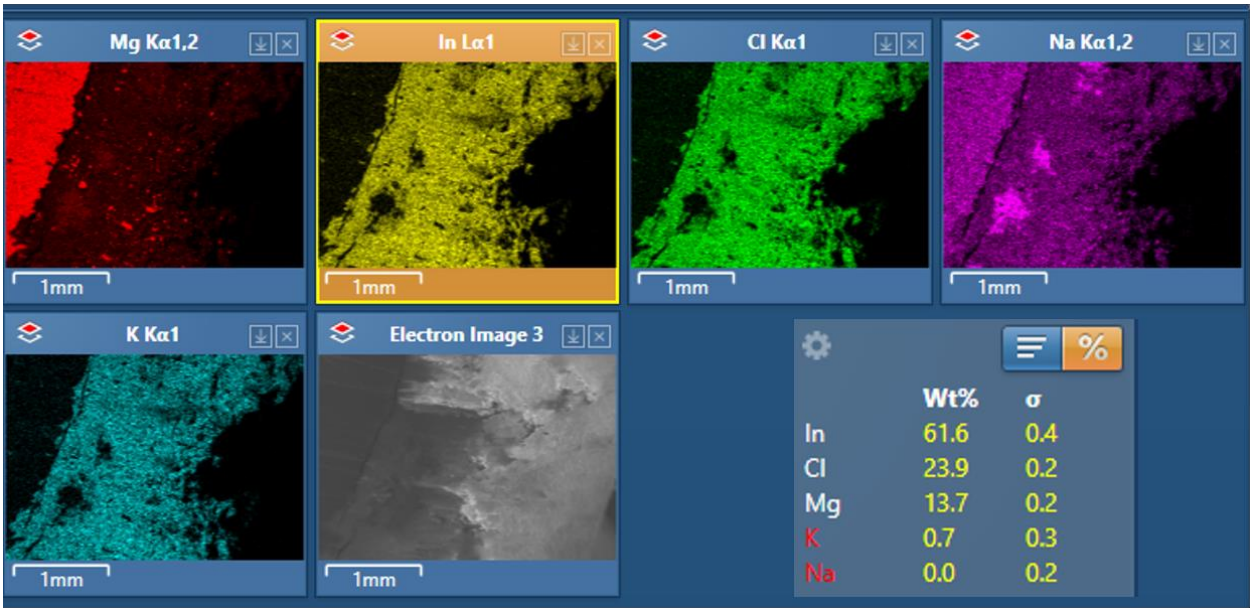

Figure 42, SEM image of the cross-section of Mg after recharging in experiment 18

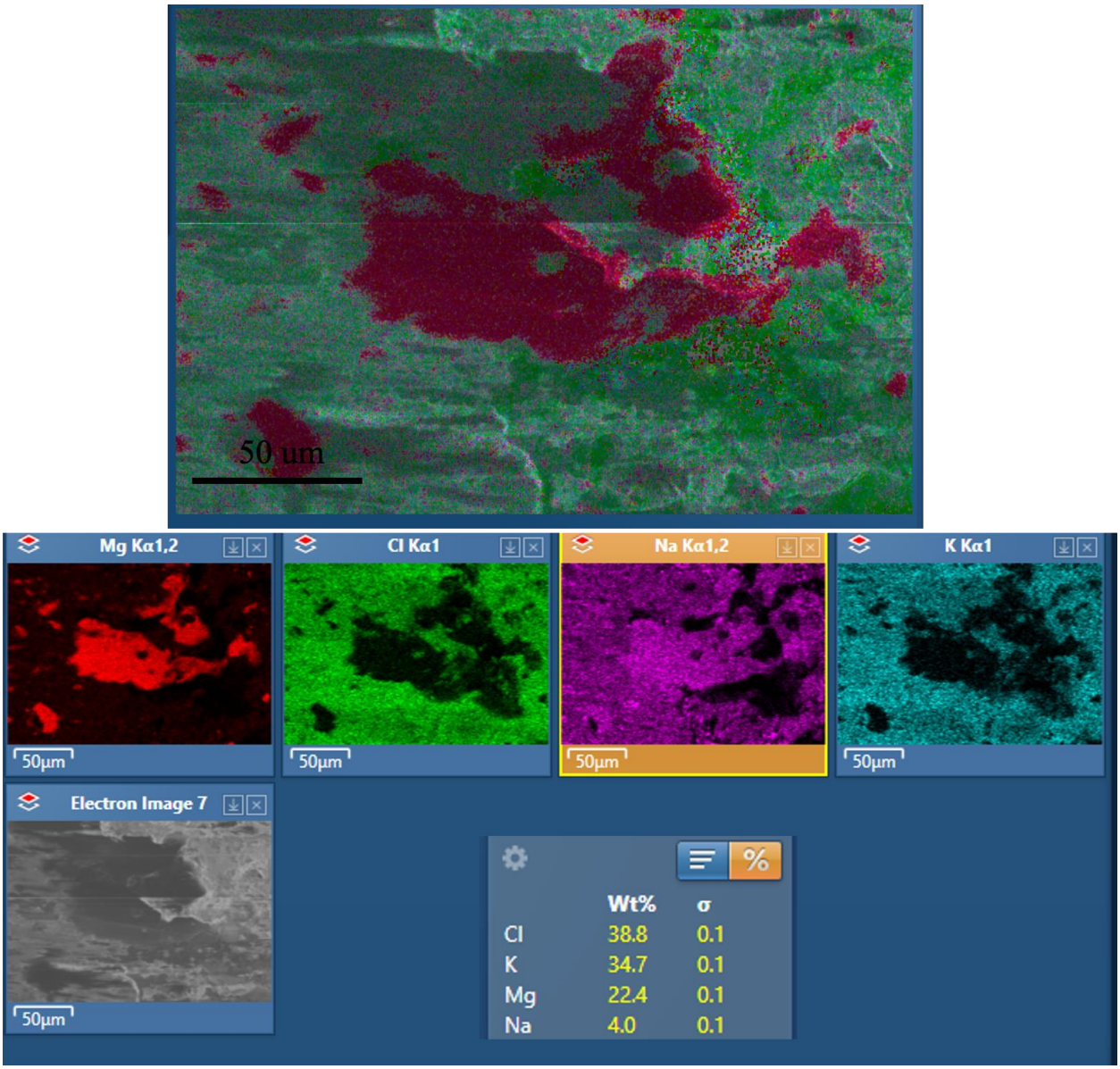

Figure 43, Zoomed-in SEM image of the Mg cross-section after the recharging experiment

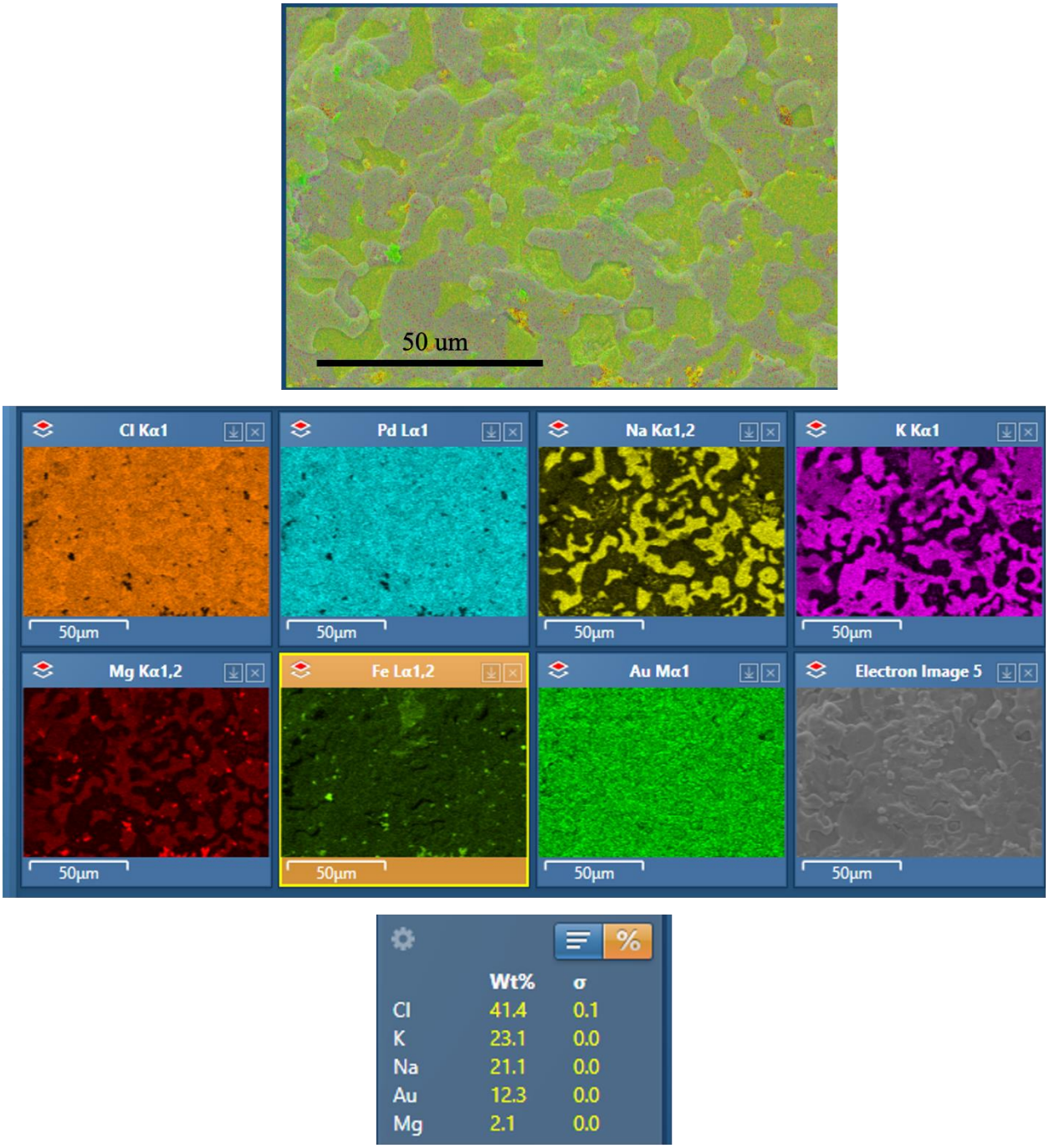

Figure 44, SEM image of Mg lump after experiment 18 recharging

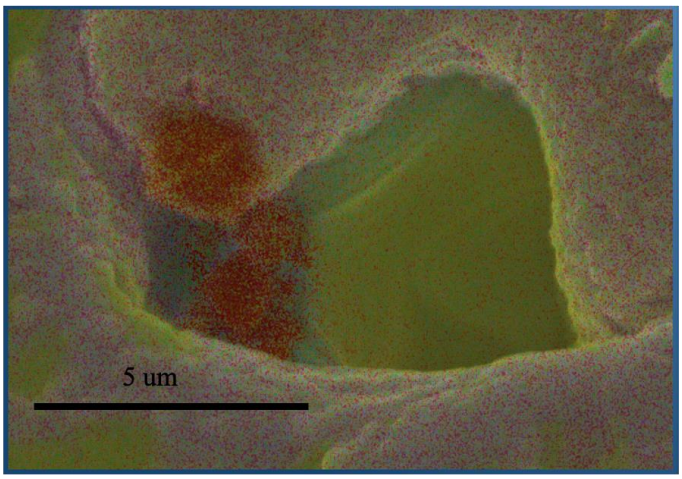

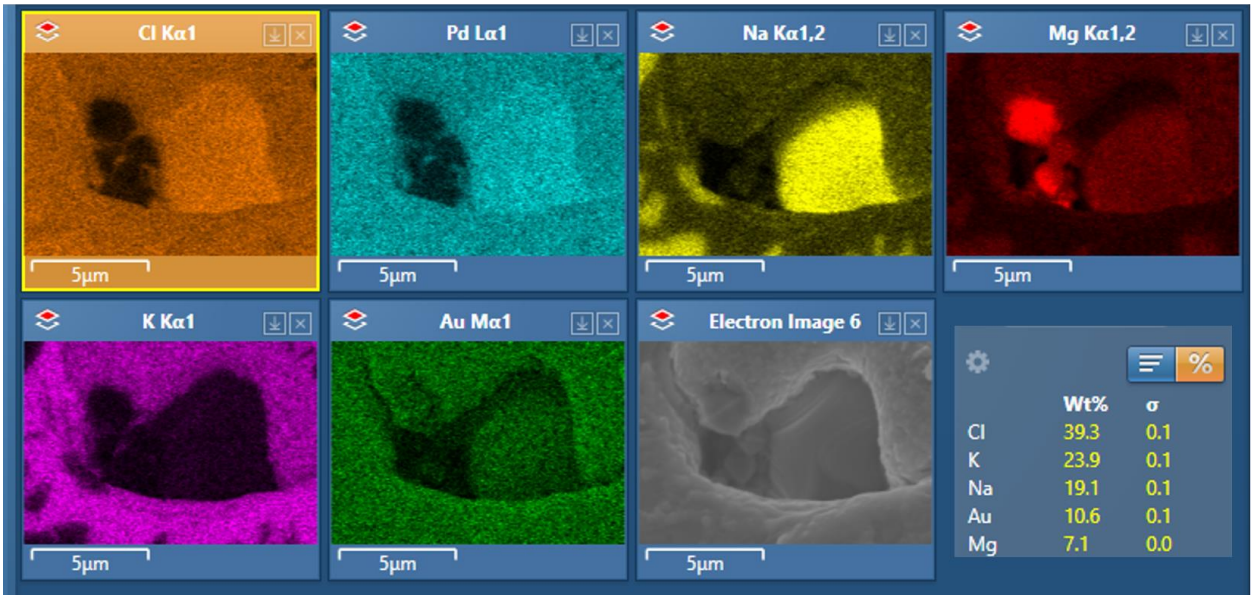

Figure 45, Zoomed-in SEM image of the Mg lump after experiment 18 recharging

6.2 Experiment 19- Second recharging

In this experiment, the recharging of the Mg-air battery was restudied. Similar setup as the previous experiments were performed and followed by a 10-hour discharge of the battery. The maximum OCV in this period was 1.5V.

During discharge, the anode of a battery is the negative terminal, while the cathode is the positive terminal. However, during charging, the flow of electrons is reversed, and the anode becomes the

positive terminal, while the cathode becomes the negative terminal. This is because, during charging, an external voltage source is applied to the battery, which drives the flow of electrons in the opposite direction to the flow during discharge. As a result, the charge carriers in the battery, which are typically ions, move from the cathode to the anode during charging, whereas they move from the anode to the cathode during discharge. Following this, after the 10-hour discharge, the cathode was pulled up and removed from the molten salt and a Ti rod was inserted as the new negative terminal.

At this point, five minutes of OCV was measured with the highest OCV of 1.25V. Two recharging 0-4 V sweeps were performed with the rate of 0.5V/min with a one-hour constant current of 1-amps in between. The OCV in this period was 0.715V, 0.85V, and 0.85V. The voltage plots for this part of the experiment are shown in Figure 46. The two recharging sweeps are shown in Figure 47 and the constant current plots and the resulting voltage are shown in Figure 48.

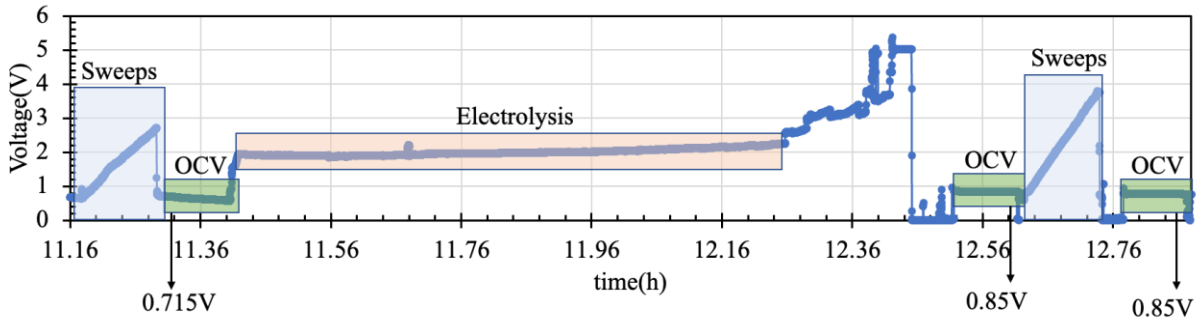

Figure 46, Battery voltage of experiment 19 recharging showing recharging sweeps and the OCV

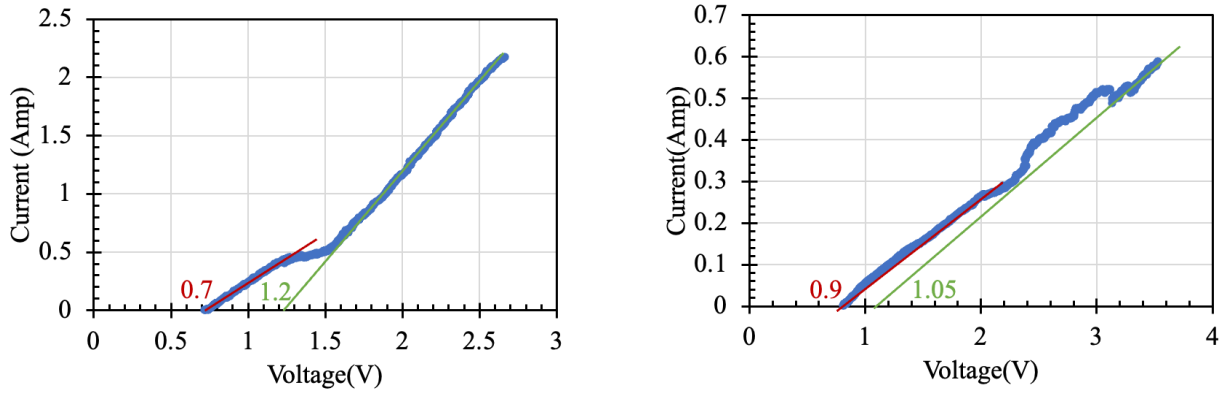

Figure 47, V-I Plots of Constant Current recharging in experiment 19

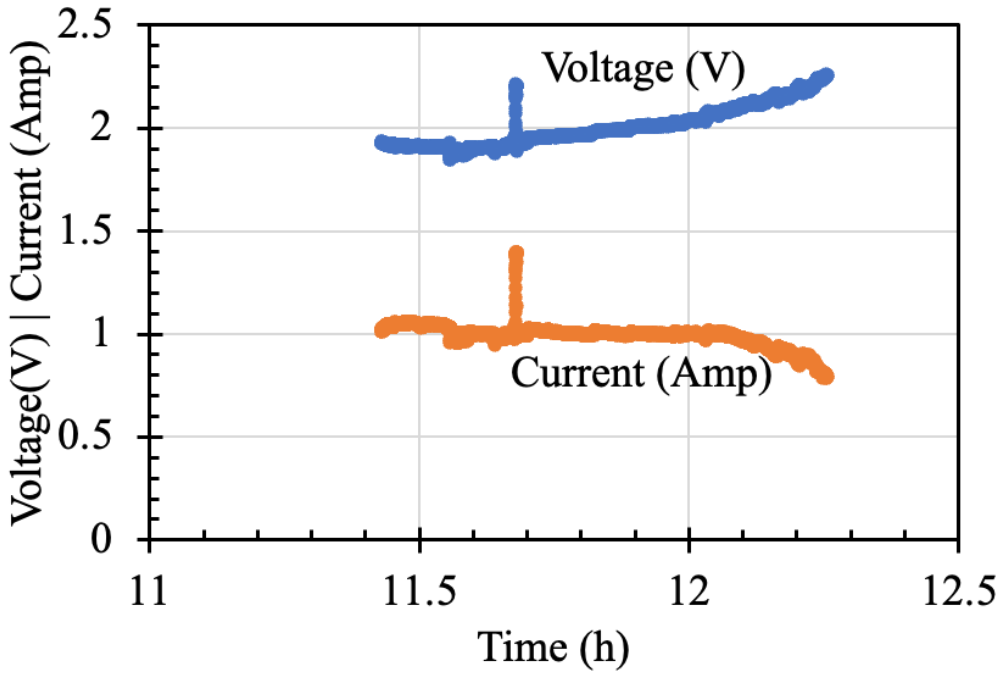

Figure 48, Voltage and Current Plots during the constant recharging of the battery in experiment 19

This test continued with two two-hour electrolysis and two voltage sweeps after that. The voltage plot over time is shown in Figure 49 and the sweeps are shown in Figure 50. The constant current and the resulting voltage are shown in Figure 51.

- 91.44 cm -81.5 cm
- $TiO2+2Mg \rightarrow 2MgO+Ti$

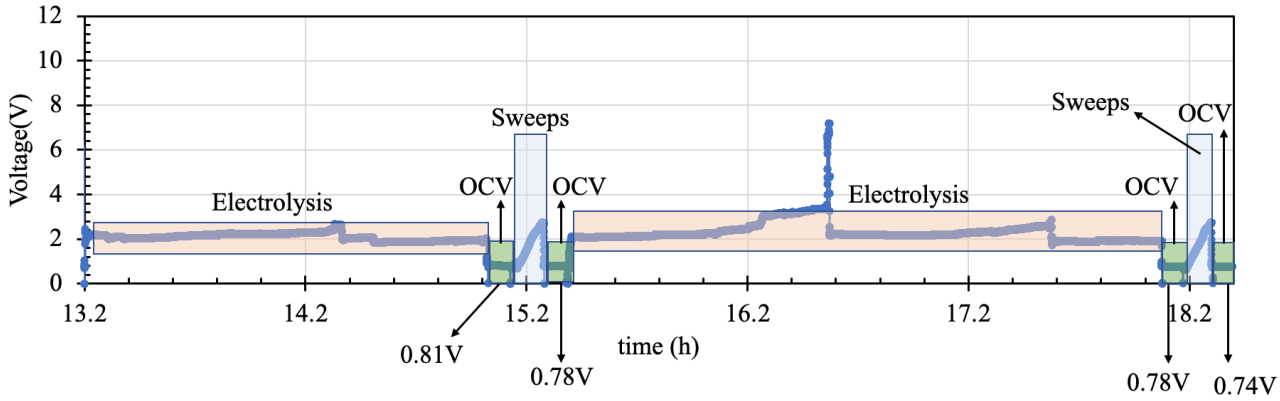

Figure 49, Battery voltage of experiment 19 recharging showing recharging sweeps and the OCV

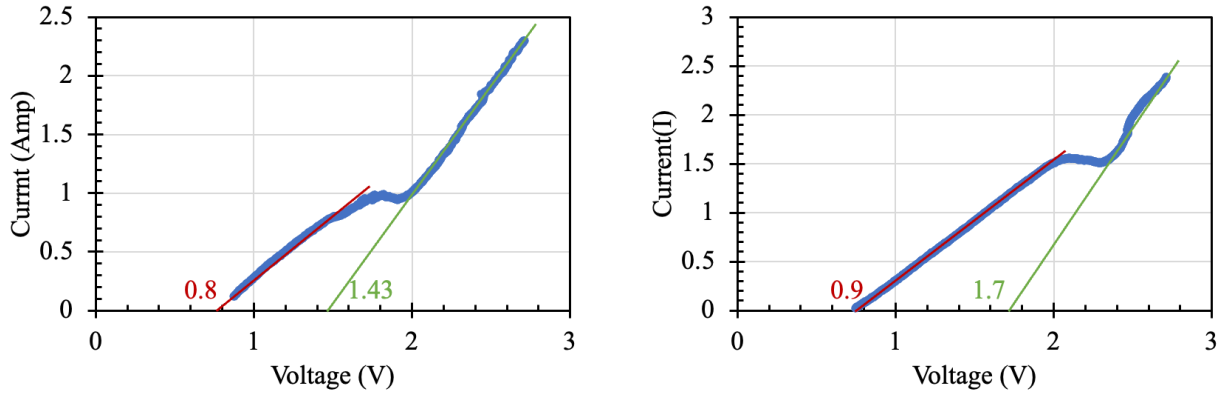

Figure 50, V-I Plots of Constant Current recharging in experiment 19

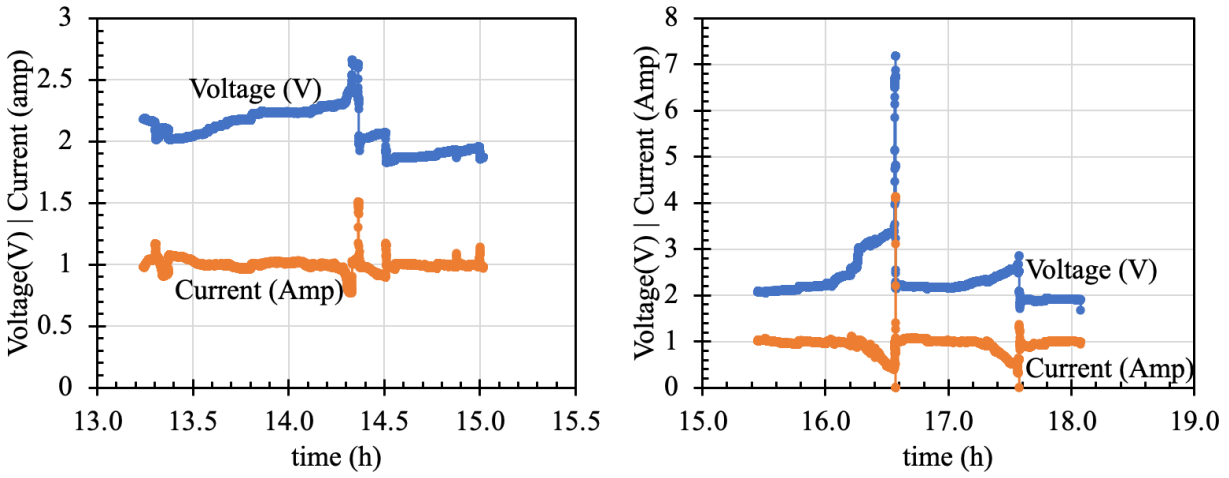

Figure 51, Voltage and Current Plots during the constant recharging of the battery in experiment 19

Figure 52 shows the Mg anode after the five-hour electrolysis. The deposited material on the initial Mg was studied under SEM-EDS and the results are shown in Figure 53, Figure 54 and Figure 55. Based on this result, mostly salts and some Ti was deposited on the charging positive terminal.

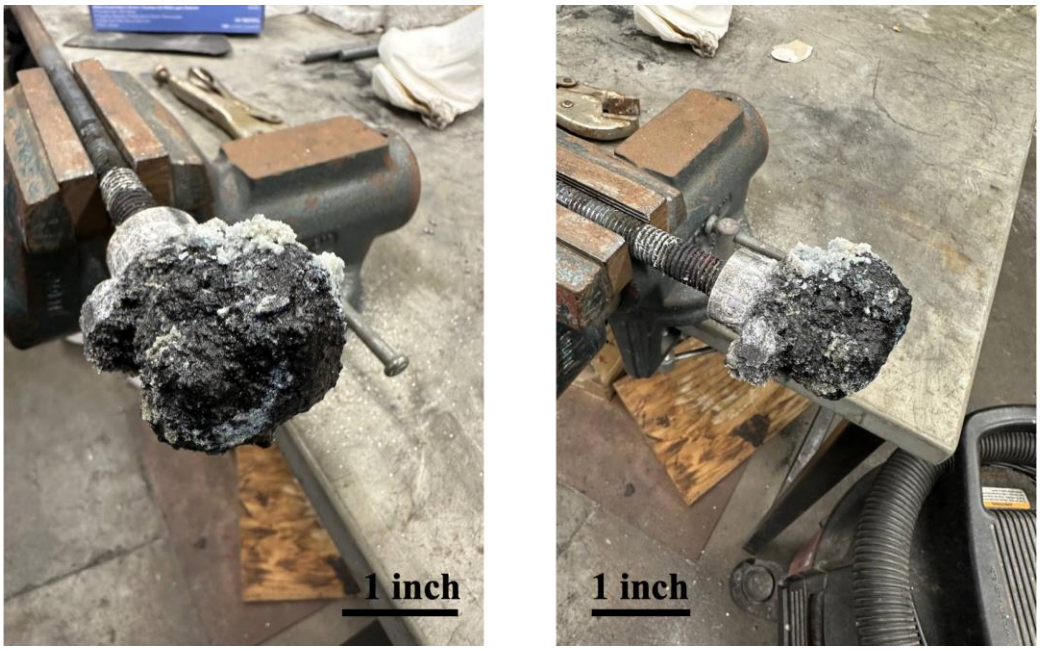

Figure 52, Mg after experiment 19 recharging

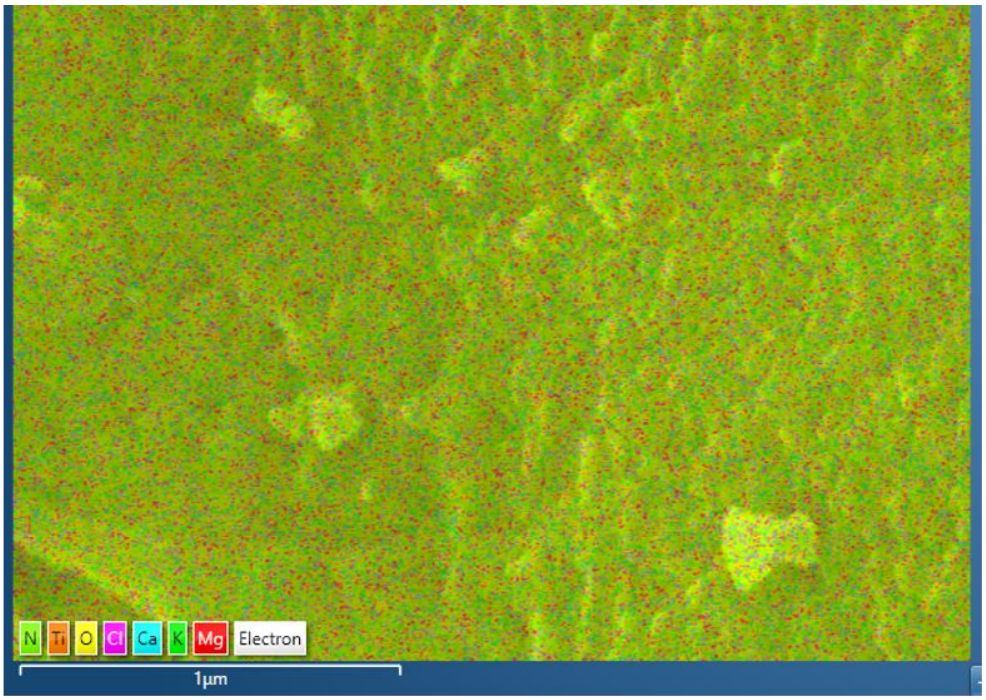

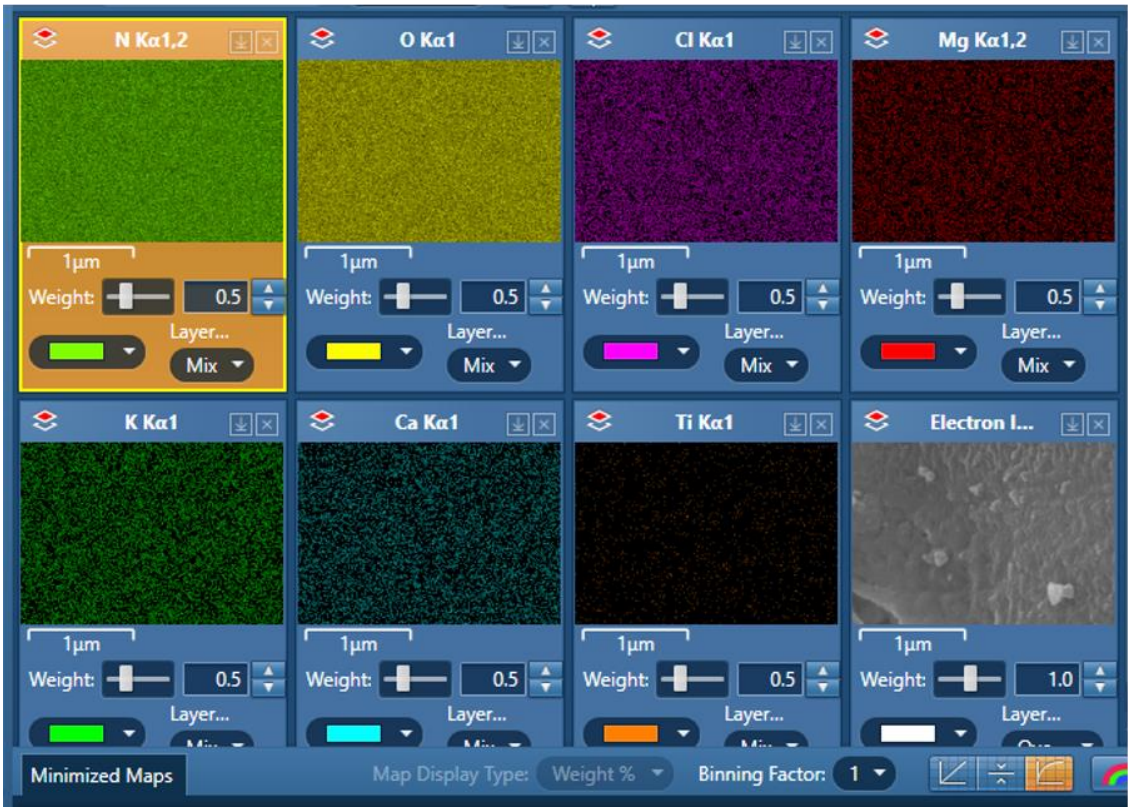

Figure 53, SEM image of Mg after experiment 19 recharging

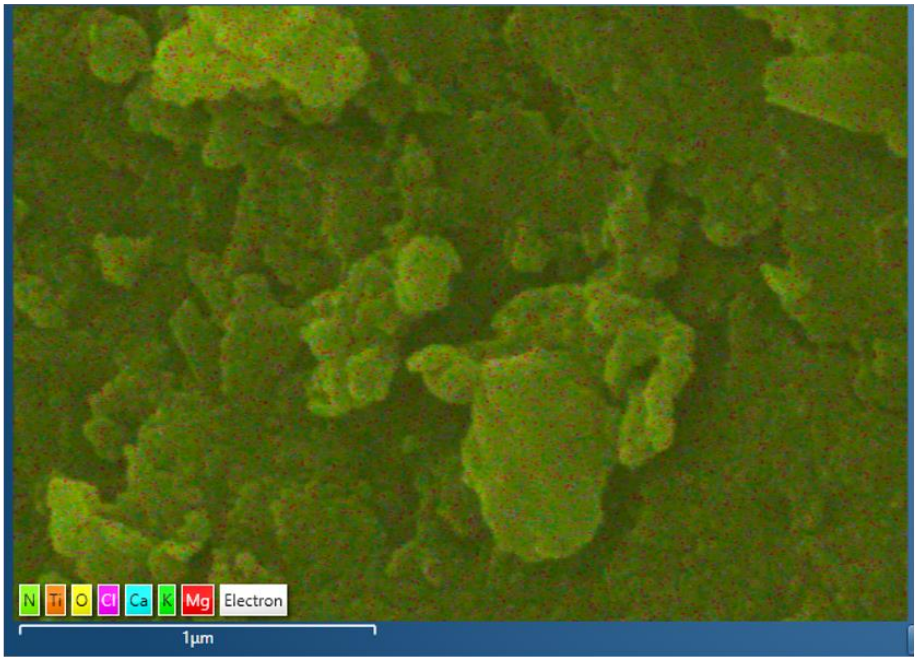

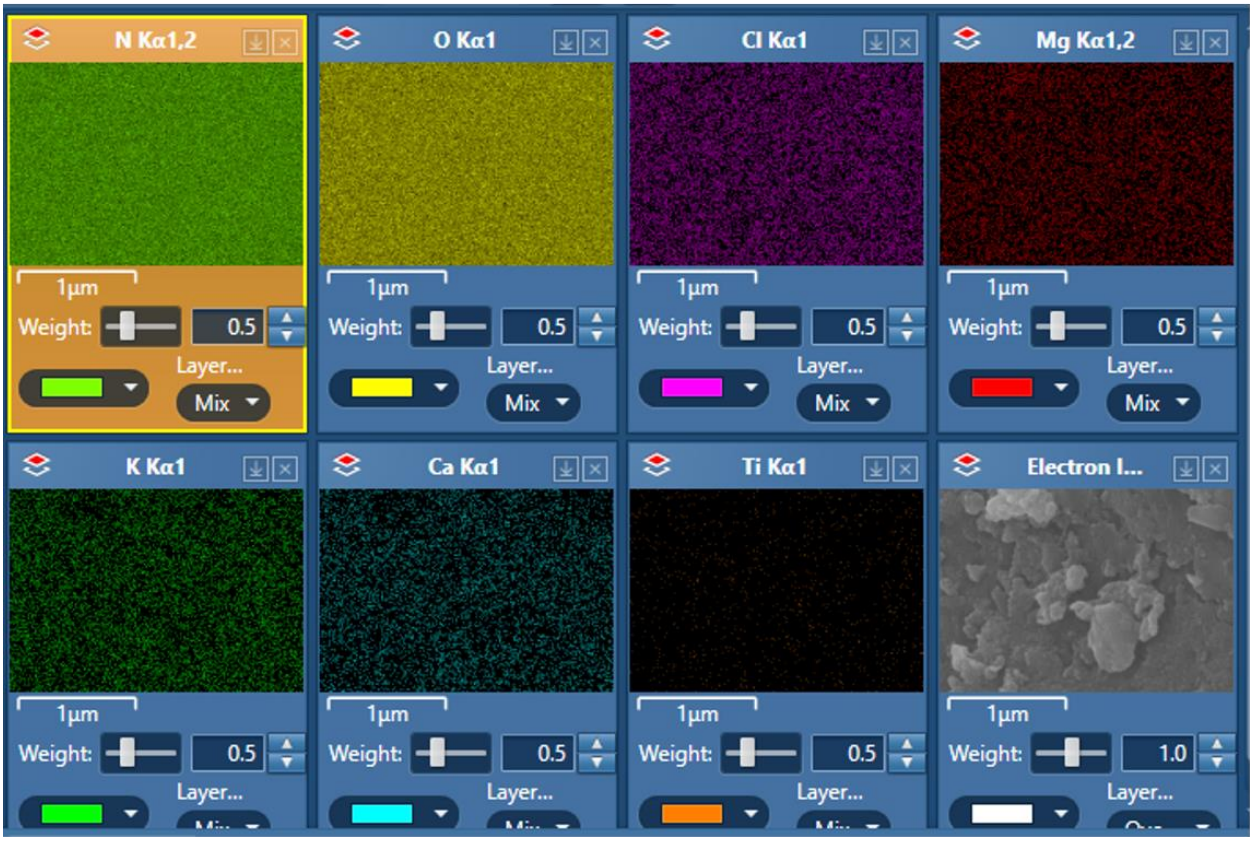

Figure 54, SEM image of Mg after experiment 19 recharging

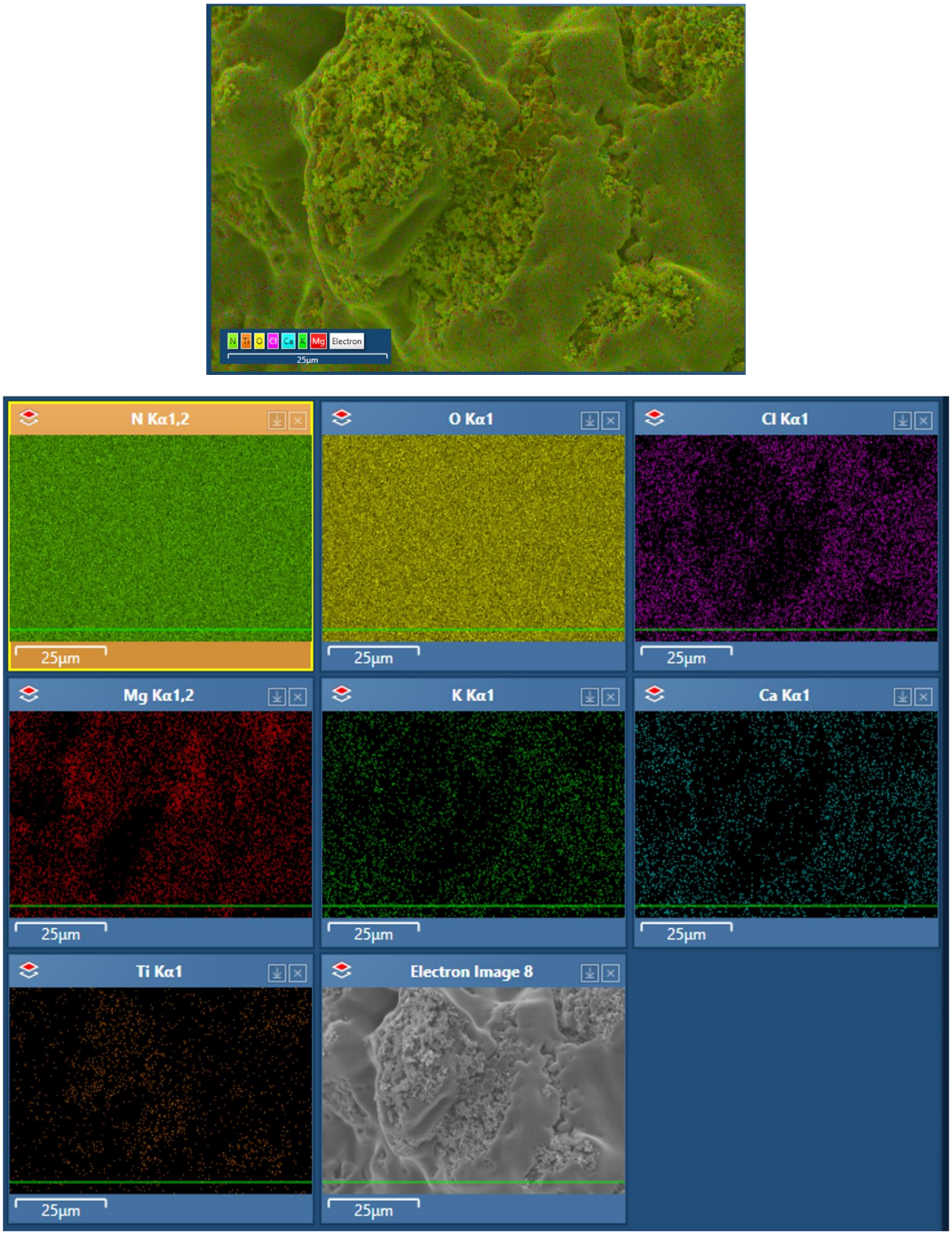

Figure 55, SEM image of Mg after experiment 19 recharging

6.3Experiment 20- Ti mesh

The twenties experiment was a replica of the normal discharge experiment but this time a dense Ti mesh was used instead of the original Ni mesh. As shown in Figure 56, the battery voltage was unstable with a maximum OCV of 1.46 V. The Mg anode is getting dissolved in layers that are different than how it was dissolved in previous experiments.

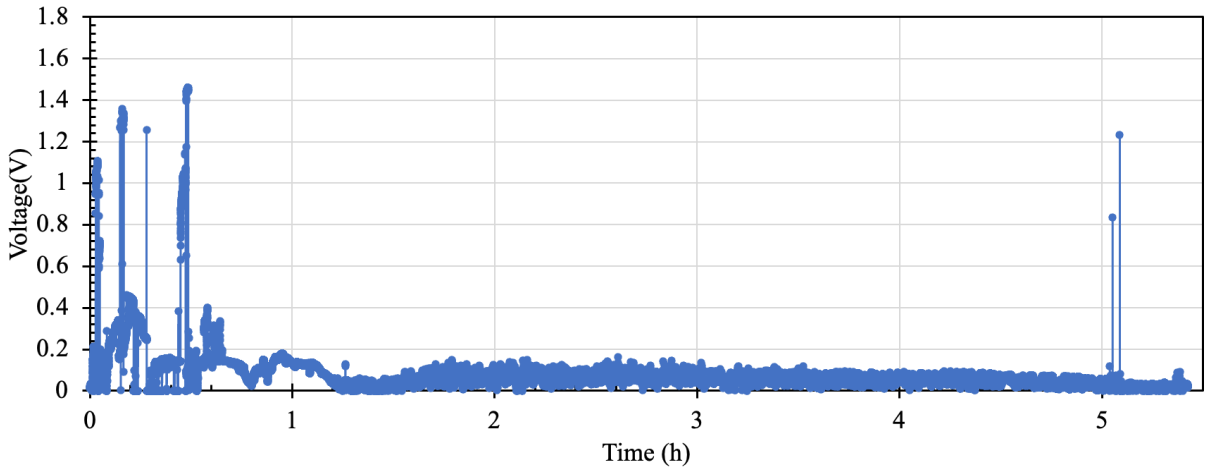

Figure 56, Voltage of MAB using Ti mesh in experiment 20

Figure 57, Experimental setup after experiment 20

Three different counter electrodes were studied. Among these stainless steel was the most promising one. Further options should be studied. Du et al. [66] presented a new type of electrode for use in high-temperature electrolyzers, which are devices that use electricity to split water into hydrogen and oxygen. Their electrode is made from an iron-based material and is designed specifically for the oxygen-evolution reaction, which is one of the two reactions that occur during water electrolysis. The authors of the paper describe the development of the electrode, including the synthesis of the iron-based material and the fabrication of the electrode.

The Ellingham diagram is a graphical representation of the thermodynamic stability of metal oxides under different temperatures and oxygen partial pressure conditions. It is used to predict the feasibility of metal oxide reduction reactions, such as the reduction of iron oxide to produce iron in a blast furnace.

The diagram plots the Gibbs free energy change of the reduction reaction for a given metal oxide versus temperature. The slope of the line represents the entropy change, while the intercept with the y-axis indicates the standard Gibbs free energy change for the reaction at 0 Kelvin.

The diagram can also include lines representing the variation in Gibbs free energy change for the formation of gaseous oxides, such as CO or CO_2, at different temperatures and oxygen partial pressures. These lines can be used to determine the equilibrium partial pressure of oxygen required for a given reduction reaction to occur.

By using the Ellingham diagram, it is possible to identify the temperature and oxygen partial pressure conditions required for a particular reduction reaction to proceed, as well as the most suitable reducing agent to use. It is a valuable tool in the design and optimization of metallurgical processes.

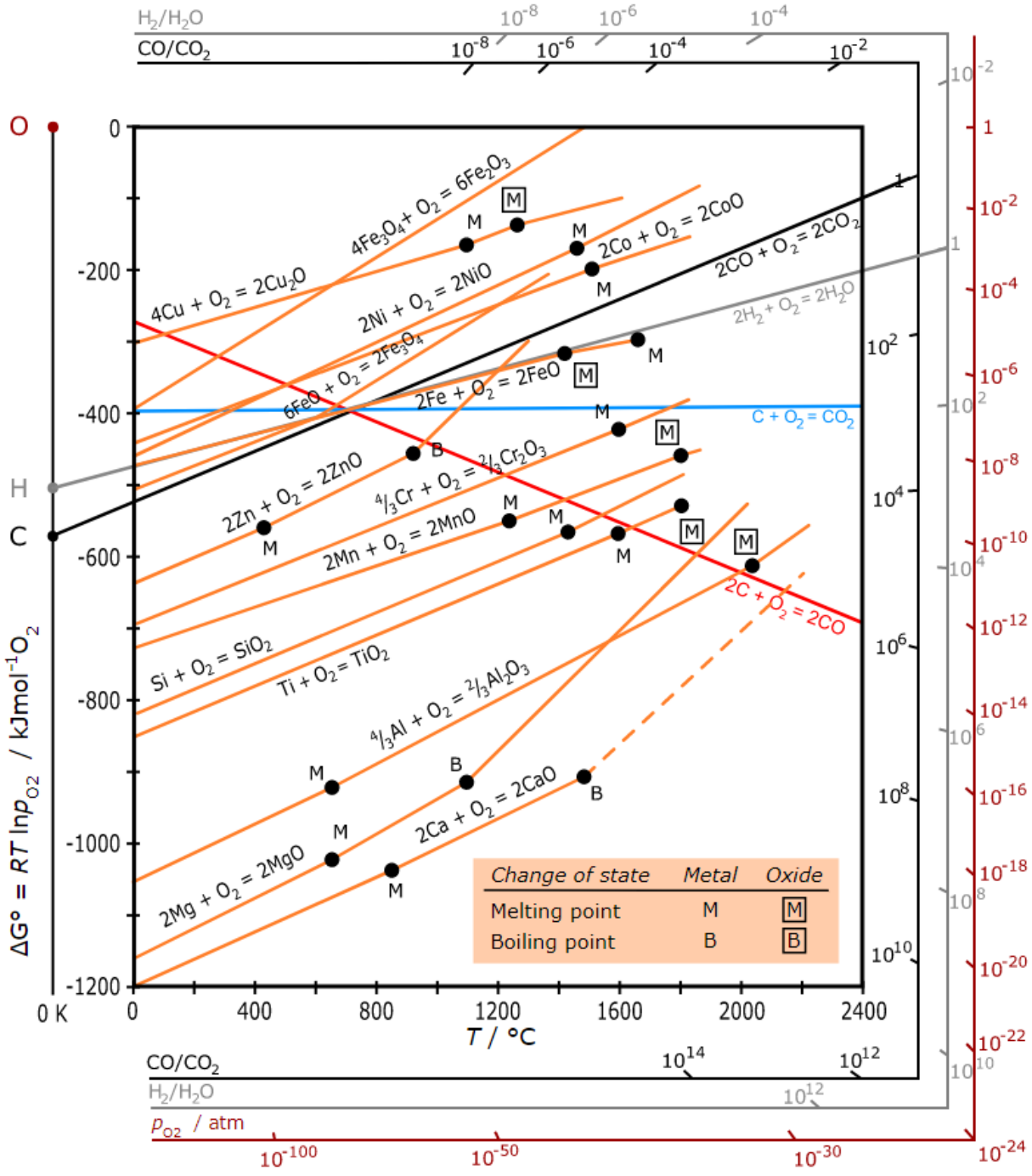

Figure 58, Ellingham Diagram for Oxides [67]

Chapter 7- 1D Diffusion Model

The following chapter includes a 1D model to calculate the boundary layer formed during supercooled solidification and estimate the required recirculation velocity to make it smaller.

C_L	Concentration of solute (O^{2-}) in liquid	mol/m^3
C_S	Concentration of (O^{2-}) in liquid at the liquid-solid interface	mol/m^3
X	Distance from phase boundary	m
D	Diffusivity in liquid	m^2/s
C	Solute concentration	mol/m^3
G	Thermal gradient	K/m

Classical Constitutional Supercooling Criterion (CSC) is derived as follows:

$(C_L-C_S)\frac{dx}{dt} = D\frac{dC}{dx}$

$\frac{dx}{dt} * \frac{dC}{dx} = D\frac{d^2C}{dx^2}$

$C=A+B \exp\left(-\frac{dX/dt}{D} * x\right)$

Boundary condition:

$C=C_L-(C_L-C_S) \exp\left(-\frac{dX/dt}{D} * x\right)$ $\rightarrow dX/dt = R = growth\ rate$

$\frac{dC}{dX} \mid (X=0) = \frac{R}{D} * (C_L-C_S)$

$\frac{dT}{dC} = \frac{dT/dX}{dC/dX} = \frac{G\ D}{R\ (C_L-C_S)} >$ (M) liquidus slope

$G > \frac{RM\ (C_L-C_S)}{D}$

R	Oxygen rate	m/s
C_O	Oxygen concentration	mol/m^3
J_O	Flux of oxygen	mol/(m^2.s)
C_{MgO}	Oxygen in MgO	mol/m^3
C_∞	Oxygen in bulk molten salt	mol/m^3
C_{int}	Oxygen in salt at the MgO interface	mol/m^3
δ	interface thickness	m
δ_u	Velocity boundary layer	

δ_T	Thermal boundary layer	
ν	kinematic viscosity	
M	Liquidus line slope	T/(mol/m^3)

In this case, the oxide ion concentration in MgO is very different from the bulk concentration in the liquid so we need a new criterion. Whereas the mass transfer boundary layer thickness in the traditional CSC is given by *D/R*, the much higher value of C_{MgO} than C_∞ means that the boundary layer thickness δ_C must be much smaller. This section quantifies the boundary layer thickness requirement.

Flux of oxygen: $J_O = RC_O - D\frac{dC_O}{dx}$ = Constant

$\frac{dJ_O}{dx} = 0 = R\frac{dC_O}{dx} - D\frac{d^2C_O}{dx^2}$

$\frac{dC}{dx} = \frac{C_\infty - C_{int}}{\delta}$

$-J_O|(X=0) = R(C_{MgO} - C_{int}) = D\frac{C_\infty - C_{int}}{\delta} + C_{int}*R$

⇨ $R(C_{MgO} - 2C_{int}) = D\frac{C_\infty - C_{int}}{\delta}$

⇨ $\delta = \frac{D(C_\infty - C_{int})}{R(C_{MgO} - 2C_{int})}$

Normally: $\delta = D/R$

But here because $C_{MgO} - 2C_{int} >> C_\infty - C_{int}$

⇨ $\delta \ll D/R$ Very small boundary layer [Point1]

$\frac{dT}{dC} = \frac{dT/dx}{dC/dx} = \frac{G*\delta}{C_\infty - C_{int}} > \frac{dT}{dC}|(liquisus\ line)$

Point1➔ $\frac{dT}{dC} = \frac{G*D*(C_\infty - C_{int})}{(C_\infty - C_{int})R(C_{MgO} - 2C_{int})} > \frac{dT}{dC}|(liquidus\ line)$

$G/R > M\frac{C_{MgO} - 2C_{int}}{D}$

In the classical format: $G/R > \frac{M(C_L - C_S)}{D}$

Next: what is the effective δ_C $\delta(V_\infty)$

We can write: $\delta_C = \frac{(C_\infty - C_{int})}{dC/dX|(X=0)}$

For velocity BL: $\frac{\delta u}{X} = 5.0\sqrt{\frac{\nu}{U_\infty X}} = \frac{5.0}{\sqrt{Re}}$

The Sc number is the Schmidt number, which is a dimensionless quantity that relates kinematic viscosity to diffusion rate. It is defined as the ratio of momentum diffusivity (kinematic viscosity) to mass diffusivity, and is given by:

Sc = ν / D

where ν is the kinematic viscosity and D is the mass diffusivity. The Schmidt number is commonly used in fluid mechanics to study transport phenomena, such as the diffusion of particles in a fluid.

$\frac{\delta_c}{\delta_u}$ = constant * $Sc^{-0.3}$

→ ν: e-5

→ D is very small, 10e-9 m^2/s

➔ $\frac{dC}{du} \approx 1/20$

δ_C concentration BL is so much smaller than δ_u velocity BL, this is in our favor. We want a small δ_C because we want to avoid constitutional supercooling, so MgO grows with a plane front.

These are all under the assumption that we have a laminar flow

h	convective heat transfer at the surface of a body	W/m²·K
k	conductive heat transfer through the body	W/m·K
L	characteristic length scale of the problem	m
K_d	mass transfer coefficient	m/s

The Sherwood number, denoted by Sh, is a dimensionless parameter used in mass transfer to characterize the transfer of a species between a fluid and a surface. It relates the rate of mass

transfer to the diffusive flux of the species and the length scale of the problem. The Sherwood number is defined as the ratio of the convective mass transfer at the surface of a body to the diffusive mass transfer through the fluid, and is given by:

$Sh = h_D L / D$

where Sh is the Sherwood number, h_D is the mass transfer coefficient, L is the characteristic length scale of the problem (such as the diameter of a pipe or the length of a reactor), and D is the diffusivity of the species in the fluid. Based on the approximate expression $h_D=D/\delta_C$, we can also approximate $Sh = L/\delta_C$.

The Sherwood number is used to characterize mass transfer in various applications, including absorption, desorption, and distillation. It plays a crucial role in the design of mass transfer equipment, as it provides a means of predicting the mass transfer coefficient for a given fluid and flow condition. The Sherwood number is also used in conjunction with the Reynolds and Schmidt numbers to characterize mass transfer in complex flows, such as turbulent and multi-phase flows.

The Sherwood number (Sh) is a dimensionless quantity used in the study of mass transfer in fluid mechanics. It relates the mass transfer rate, or the rate of transport of a species in a fluid, to the rate of diffusion of that species in the fluid. The Sherwood number can be expressed as a function of the Reynolds number (Re) and the Schmidt number (Sc) as follows:

Sh = C * Re^a * Sc^b

where C, a, and b are constants that depend on the geometry and flow conditions of the system being studied.

The value of the constant C can be determined experimentally, and its value typically ranges from 0.23 to 0.9 depending on the geometry of the system. The exponents a and b depend on the type of flow regime and the physical properties of the fluid.

For example, for laminar flow over a flat plate, the Sherwood number can be expressed as:

Sh = 0.664 * Re^(1/2) * Sc^(1/3)

where Re is the Reynolds number and Sc is the Schmidt number.

In general, the Sherwood number increases with increasing Reynolds number and decreasing Schmidt number, indicating that the rate of mass transfer increases with increasing fluid velocity and decreasing diffusivity of the species being transported. Therefore, in order to have a small δ_C, it is necessary to have a large value of Sh, a large value of Re, and high velocity. It is likely that the molten salt velocity due to gas lift from air bubbles will indeed be relatively large, but estimating it is beyond the scope of this work.

Chapter 8- Cost modeling

A single lab-scale Mg-air battery can achieve a current density of 2.3 A/cm^2 at 100% transformation of one electron per atom of Mg when operating at maximum power. The theoretical model predicts an open circuit voltage (OCV) of 2.6 V, and at this current density, the estimated operating voltage is 1.3 V, resulting in a power density of 2.93 W/cm^2.

Considering a single anode-cathode pair from the full-scale 20-foot battery, depicted in Figure 59, the Mg slab's dimensions are 1.5 x 2 x 0.45 m^3, resulting in a surface area of 30,000 cm^2. Thus, the power of a single cell can be estimated to be 87.96 kW, with an efficiency of 40.89% over 75 hours of operation.

A candidate 20-foot battery design consists of 10 anode and cathode pairs connected in series. With a 40% efficiency, the theoretical current density of this cell is 2.3 A/cm^2, and the cell voltage is 1.3 V, producing a power density of 2.9 W/cm^2. With 10 cells in a stack, the overall power in a container ship is 880 kW, and the capacity of the cell is approximately 66 MWh over 75.1 hours of operation, assuming perfect current efficiency and oxide removal from the bath. Alternatively, at a lower current density of 0.2 A/cm^2, the battery can achieve a voltage of 2.5 V, power density of 0.5 W/cm2, 81% efficiency, 151 kW power, and 130 MWh capacity.

Based on experimental results, the Mg-air battery exhibited a power density of 0.4 W/cm2 or 109 kW power on a full scale. However, the voltage-current profile demonstrated only 50-80% of theoretical voltage, likely due to dissolved oxide in the molten salt as mentioned above. If this performance holds for a larger battery, it could result in an energy delivery of 60-90 MWh from the 20-foot container battery.

The most significant cost drivers for Mg-air full-scale batteries are the nickel cathode materials, in the worst-case scenario. The estimated cost for these cells ranges from $315-365k for a 20-foot container battery delivering 60-90 MWh.

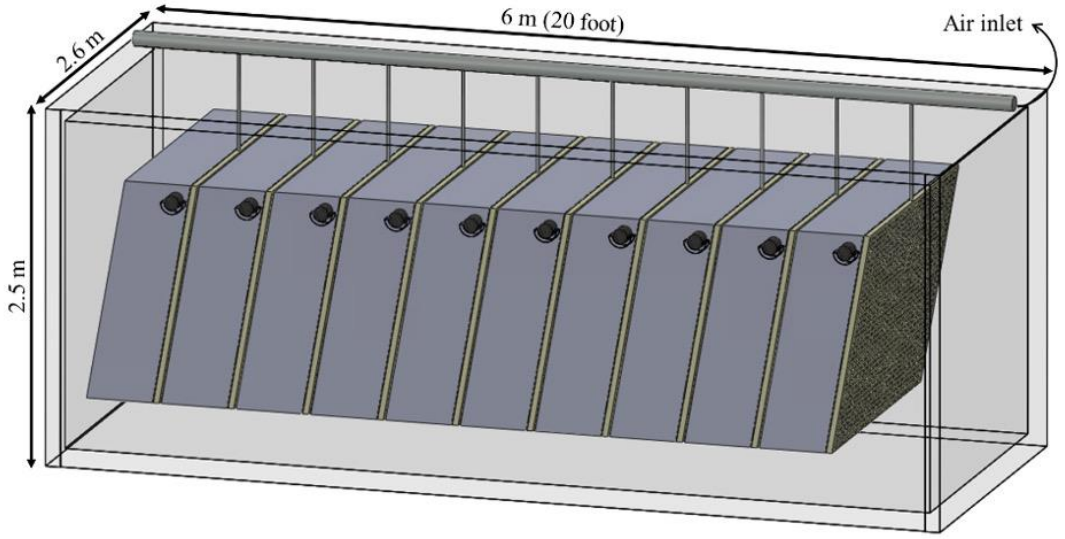

Figure 59, Full-scale MAB in a 20-foot shipping container

Key findings

With global warming being one of the most critical challenges of today's world, this paper proposes an innovative Mg-air battery as an emission-free alternative to conventional energy sources. This work includes modeling and experimental investigation of Mg-air batteries. The key findings of this work are listed below:

- Mg-air batteries can provide the high energy density required for long-haul transportation.
- The OCV of this battery was calculated as 2.62 V.
- Experiments were able to reach as high as 71% OCV of Mg-air battery.
- The maximum current density reached in the experiments was 2.9 which is almost equal to the modeling expectations.
- At 73% of efficiency, the Mg-air battery is expected to operate under 0.5 A/cm^2 current density and 1.17 W/cm^2 power density.
- At a current density of 2.5 A/cm^2, power increases to 2.89 W/cm^2, but efficiency falls to 36%.
- For reaching the highest performance of the battery, MgO concentration should be kept as low as possible in the electrolyte. This can be achieved by either freezing the MgO from the bottom or filtering it out.
- With 60-90 MWh battery capacity, the Mg-air battery has at least 8 times the battery capacity of other shipping batteries making transpacific zero emission cruising possible.
- The cold finger demonstrates that long-term battery operation is possible by selective solidification of MgO to maintain MgO composition in the molten salt.
- The MgO formed on the cold finger can be used for Mg electrolysis and recharging of the battery
- This molten salt Mg-air battery concept shows potential for much higher energy density at comparable cost vs. other metal-air chemistries such as iron-air[125].

Future Work

The following list includes some potential ideas for future work on this project:

- Study MgO directional solidification, required gradient, and the heat loss in the system.
- Study other materials as an inert counter-electrode for the recharging process and look into the morphology of the magnesium deposit.
- Investigate thermal modeling of the cell and ΔH of the half-reactions.
- Studying the species formed during discharge and recharging.
- Study the effect of operation temperature on battery performance.
- Try out a different mixture of salts (Ex: Increase Mg ion concentration, Add fluorides to the salts).
- Get a cross-section of deposition on cold finger deposit to study the structure and morphonology of the deposit and its oxygen concentration. This might require sample preparation with oil polishing followed by EBSD.
- Use pseudo reference electrode or reference electrode, to learn more about the electrochemical reactions during charge and discharge.

Data availability

All data taken in this study are disclosed in this document.

Declaration of competing interest

The author and advisor are co-inventors on a patent application covering this technology [69]. Aside from this, the authors declare that they have no known competing financial interests or personal relationships that could have appeared to influence the work reported in this paper.

References

[1] S. Kim *et al.*, "A comprehensive review on the pretreatment process in lithium-ion battery recycling," *J. Clean. Prod.*, vol. 294, p. 126329, Apr. 2021, doi: 10.1016/j.jclepro.2021.126329.

[2] N. Tapia-Ruiz *et al.*, "2021 roadmap for sodium-ion batteries," *J. Phys. Energy*, vol. 3, no. 3, p. 031503, Jul. 2021, doi: 10.1088/2515-7655/ac01ef.

[3] W. Sun *et al.*, "A rechargeable zinc-air battery based on zinc peroxide chemistry," *Science*, vol. 371, no. 6524, pp. 46–51, Jan. 2021, doi: 10.1126/science.abb9554.

[4] G. Wang, H. Zou, X. Zhu, M. Ding, and C. Jia, "Recent progress in zinc-based redox flow batteries: a review," *J. Phys. Appl. Phys.*, vol. 55, no. 16, p. 163001, Apr. 2022, doi: 10.1088/1361-6463/ac4182.

[5] S. Licht, B. Cui, J. Stuart, B. Wang, and J. Lau, "Molten air – a new, highest energy class of rechargeable batteries," *Energy Environ. Sci.*, vol. 6, no. 12, p. 3646, 2013, doi: 10.1039/c3ee42654h.

[6] B. Cui and S. Licht, "A low temperature iron molten air battery," *J Mater Chem A*, vol. 2, no. 27, pp. 10577–10580, 2014, doi: 10.1039/C4TA01290A.

[7] S. Liu *et al.*, "A novel rechargeable zinc-air battery with molten salt electrolyte," *J. Power Sources*, vol. 342, pp. 435–441, Feb. 2017, doi: 10.1016/j.jpowsour.2016.12.080.

[8] M. Yoshio, R. J. Brodd, and A. Kozawa, Eds., *Lithium-Ion Batteries*. New York, NY: Springer New York, 2009. doi: 10.1007/978-0-387-34445-4.

[9] F. Tong, S. Wei, X. Chen, and W. Gao, "Magnesium alloys as anodes for neutral aqueous magnesium-air batteries," *J. Magnes. Alloys*, p. S2213956721001146, Jun. 2021, doi: 10.1016/j.jma.2021.04.011.

[10] K. F. Blurton and A. F. Sammells, "Metal/air batteries: Their status and potential — a review," *J. Power Sources*, vol. 4, no. 4, pp. 263–279, Jan. 1979, doi: 10.1016/0378-7753(79)80001-4.

[11] H.-F. Wang and Q. Xu, "Materials Design for Rechargeable Metal-Air Batteries," *Matter*, vol. 1, no. 3, pp. 565–595, Sep. 2019, doi: 10.1016/j.matt.2019.05.008.

[12] "Multi-Gas Contributors to Global Climate Change," *Center for Climate and Energy Solutions*, Feb. 20, 2003. https://www.c2es.org/document/multi-gas-contributors-to-global-climate-change/ (accessed Sep. 01, 2021).

[13] Q. Zhang *et al.*, "Exposure to Alumina Nanoparticles in Female Mice During Pregnancy Induces Neurodevelopmental Toxicity in the Offspring," *Front. Pharmacol.*, vol. 9, p. 253, 2018, doi: 10.3389/fphar.2018.00253.

[14] E. Faegh, B. Ng, D. Hayman, and W. E. Mustain, "Practical assessment of the performance of aluminium battery technologies," *Nat. Energy*, pp. 1–9, Dec. 2020, doi: 10.1038/s41560-020-00728-y.

[15] P. Pei *et al.*, "A high-energy-density and long-stable-performance zinc-air fuel cell system," *Appl. Energy*, vol. 241, pp. 124–129, May 2019, doi: 10.1016/j.apenergy.2019.03.004.

[16] C. Peng *et al.*, "A Rechargeable High-Temperature Molten Salt Iron-Oxygen Battery," *ChemSusChem*, vol. 11, no. 11, pp. 1880–1886, Jun. 2018, doi: 10.1002/cssc.201800237.

[17] et Czelej al, “Atomistic insight into the electrode reaction mechanism of the cathode in molten carbonate fuel cells,” *J. Mater. Chem.*, 2017.
[18] A. G. Olabi *et al.*, “Metal-Air Batteries—A Review,” *Energies*, vol. 14, no. 21, p. 7373, Nov. 2021, doi: 10.3390/en14217373.
[19] L. Zhang, Q. Shao, and J. Zhang, “An overview of non-noble metal electrocatalysts and their associated air cathodes for Mg-air batteries,” *Mater. Rep. Energy*, vol. 1, no. 1, p. 100002, Feb. 2021, doi: 10.1016/j.matre.2020.11.001.
[20] Md. A. Rahman, X. Wang, and C. Wen, “High Energy Density Metal-Air Batteries: A Review,” *J. Electrochem. Soc.*, vol. 160, no. 10, pp. A1759–A1771, 2013, doi: 10.1149/2.062310jes.
[21] Y. Li and J. Lu, “Metal–Air Batteries: Will They Be the Future Electrochemical Energy Storage Device of Choice?,” *ACS Energy Lett.*, vol. 2, no. 6, pp. 1370–1377, Jun. 2017, doi: 10.1021/acsenergylett.7b00119.
[22] R. Cao, J.-S. Lee, M. Liu, and J. Cho, “Recent Progress in Non-Precious Catalysts for Metal-Air Batteries,” *Adv. Energy Mater.*, vol. 2, no. 7, pp. 816–829, Jul. 2012, doi: 10.1002/aenm.201200013.
[23] J.-S. Lee *et al.*, “Metal–Air Batteries with High Energy Density: Li–Air versus Zn–Air,” *Adv. Energy Mater.*, vol. 1, no. 1, pp. 34–50, 2011, doi: 10.1002/aenm.201000010.
[24] K. C. Divya and J. Østergaard, “Battery energy storage technology for power systems—An overview,” *Electr. Power Syst. Res.*, vol. 79, no. 4, pp. 511–520, Apr. 2009, doi: 10.1016/j.epsr.2008.09.017.
[25] J. R. Selman, R. K. Steuenberg, J. J. Barghusen, and W. G. Howard, “Proceedings of the symposium and workshop on advanced battery research and design, March 22--24, 1976. [Held at ANL],” Argonne National Lab., Ill. (USA), ANL-76-8; CONF-760312-, Jan. 1976. Accessed: Sep. 15, 2022. [Online]. Available: https://www.osti.gov/biblio/7339886#page=91
[26] L. S. Martins, L. F. Guimarães, A. B. Botelho Junior, J. A. S. Tenório, and D. C. R. Espinosa, “Electric car battery: An overview on global demand, recycling and future approaches towards sustainability,” *J. Environ. Manage.*, vol. 295, p. 113091, Oct. 2021, doi: 10.1016/j.jenvman.2021.113091.
[27] N. Nitta, F. Wu, J. T. Lee, and G. Yushin, “Li-ion battery materials: present and future,” *Mater. Today*, vol. 18, no. 5, pp. 252–264, Jun. 2015, doi: 10.1016/j.mattod.2014.10.040.
[28] S. Ma *et al.*, “Temperature effect and thermal impact in lithium-ion batteries: A review,” *Prog. Nat. Sci. Mater. Int.*, vol. 28, no. 6, pp. 653–666, Dec. 2018, doi: 10.1016/j.pnsc.2018.11.002.
[29] T. Oshima, M. Kajita, and A. Okuno, “Development of Sodium-Sulfur Batteries,” *Int. J. Appl. Ceram. Technol.*, vol. 1, no. 3, pp. 269–276, Jan. 2005, doi: 10.1111/j.1744-7402.2004.tb00179.x.
[30] W. W. Drenckhahn *et al.*, “A Novel High Temperature Metal - Air Battery,” *ECS Trans.*, vol. 50, no. 45, pp. 125–135, Apr. 2013, doi: 10.1149/05045.0125ecst.
[31] S. Yang, “Design and analysis of aluminum/air battery system for electric vehicles,” *J. Power Sources*, vol. 112, no. 1, pp. 162–173, Oct. 2002, doi: 10.1016/S0378-7753(02)00370-1.

[32] G. Toussaint, P. Stevens, L. Akrour, R. Rouget, and F. Fourgeot, “Development of a Rechargeable Zinc-Air Battery,” *ECS Trans.*, vol. 28, no. 32, pp. 25–34, Oct. 2010, doi: 10.1149/1.3507924.
[33] R. D. McKerracher, C. Ponce de Leon, R. G. A. Wills, A. A. Shah, and F. C. Walsh, “A Review of the Iron-Air Secondary Battery for Energy Storage,” *ChemPlusChem*, vol. 80, no. 2, pp. 323–335, Feb. 2015, doi: 10.1002/cplu.201402238.
[34] M. Shahabi, N. Masse, H. Sun, L. Wallace, A. Powell, and Y. Zhong, “Design of a Molten Salt Metal-Air Battery with High-Energy Density,” in *REWAS 2022: Energy Technologies and CO2 Management (Volume II)*, F. Tesfaye, L. Zhang, D. P. Guillen, Z. Sun, A. A. Baba, N. R. Neelameggham, M. Zhang, D. E. Verhulst, and S. Alam, Eds., in The Minerals, Metals & Materials Series. Cham: Springer International Publishing, 2022, pp. 47–57. doi: 10.1007/978-3-030-92559-8_6.
[35] R. Lan and S. Tao, “Ammonia as a Suitable Fuel for Fuel Cells,” *Front. Energy Res.*, vol. 2, Aug. 2014, doi: 10.3389/fenrg.2014.00035.
[36] C. M. Reich, A. Kaiser, and J. T. S. Irvine, “Niobia Based Rutile Materials as SOFC Anodes,” *Fuel Cells*, vol. 1, no. 3–4, pp. 249–255, Dec. 2001, doi: 10.1002/1615-6854(200112)1:3/4<249::AID-FUCE249>3.0.CO;2-A.
[37] T. Polat, A. H. Yalçin, and Sahin, H Mehmet, “Study on Processes of Hydrogen Production Based Nuclear Energy,” p. 21, 2012.
[38] A. Midilli, M. Ay, I. Dincer, and M. A. Rosen, “On hydrogen and hydrogen energy strategies I: Current status and needs,” *Fuel Energy Abstr.*, vol. 46, no. 4, p. 222, Jul. 2005, doi: 10.1016/S0140-6701(05)81477-8.
[39] A. Powell, “A Magnesium Clean Energy Ecosystem Vision,” in *Magnesium Technology 2022*, P. Maier, S. Barela, V. M. Miller, and N. R. Neelameggham, Eds., in The Minerals, Metals & Materials Series. Cham: Springer International Publishing, 2022, pp. 121–126. doi: 10.1007/978-3-030-92533-8_20.
[40] “DNV_Maritime_Forecast_2050_2021-Web.pdf.”
[41] S. Doll, “World’s largest electric cruise ship’ makes maiden voyage in China with a whopping 7,500 kWh in battery power,” *Electrek*, Mar. 31, 2022. https://electrek.co/2022/03/31/worlds-largest-electric-cruise-ship-makes-maiden-voyage-in-china-with-a-whopping-7500-kwh-in-battery-power/ (accessed Sep. 15, 2022).
[42] “Batteries powering new cruise ship AND e-ferry - Plugboats,” Jul. 03, 2019. https://plugboats.com/batteries-powering-new-cruise-ship-and-e-ferry/ (accessed Sep. 15, 2022).
[43] “Yara Birkeland | Yara International,” *Yara None*, Nov. 12, 2021. https://www.yara.com/news-and-media/press-kits/yara-birkeland-press-kit/ (accessed Sep. 15, 2022).
[44] “Ship Yara Birkeland (Container Ship) Registered in Norway,” *MarineTraffic.com*. https://www.marinetraffic.com/en/ais/details/ships/shipid:6407606/mmsi:257646000/imo:9865049/vessel:YARA BIRKELAND (accessed Sep. 16, 2022).
[45] “Ampere Electric-Powered Ferry,” *Ship Technology*. https://www.ship-technology.com/projects/norled-zerocat-electric-powered-ferry/ (accessed Sep. 15, 2022).
[46] D. L. Bleviss, “Transportation is critical to reducing greenhouse gas emissions in the United States,” *WIREs Energy Environ.*, vol. 10, no. 2, Mar. 2021, doi: 10.1002/wene.390.

[47] Y. F. Khalil, “Science-based framework for ensuring safe use of hydrogen as an energy carrier and an emission-free transportation fuel,” *Process Saf. Environ. Prot.*, vol. 117, pp. 326–340, Jul. 2018, doi: 10.1016/j.psep.2018.05.011.
[48] S. Hasanvand, M. Rafiei, M. Gheisarnejad, and M.-H. Khooban, “Reliable Power Scheduling of an Emission-Free Ship: Multiobjective Deep Reinforcement Learning,” *IEEE Trans. Transp. Electrification*, vol. 6, no. 2, pp. 832–843, Jun. 2020, doi: 10.1109/TTE.2020.2983247.
[49] “DNVGL-ST-0033 - Maritime simulator systems | GlobalSpec.” https://standards.globalspec.com/std/14297127/DNVGL-ST-0033 (accessed Mar. 28, 2023).
[50] “DNV-ST-0373 - Hardware in the loop testing (HIL) | GlobalSpec.” https://standards.globalspec.com/std/14480800/dnv-st-0373 (accessed Mar. 28, 2023).
[51] M. Anantharaman, R. Islam, F. Khan, and V. Garaniya, “A review of progress leading to Carbon-Free shipping,” in *Proceedings of the 2022 International Maritime Conference*, ’. ’, Ed., Australia: International Convention Centre, 2022, pp. 1–15. Accessed: Mar. 28, 2023. [Online]. Available: https://www.indopacificexpo.com.au/IMC2022/index.asp
[52] E. Malmgren, S. Brynolf, E. Fridell, M. Grahn, and K. Andersson, “The environmental performance of a fossil-free ship propulsion system with onboard carbon capture – a life cycle assessment of the HyMethShip concept,” *Sustain. Energy Fuels*, vol. 5, no. 10, pp. 2753–2770, 2021, doi: 10.1039/D1SE00105A.
[53] “IMO News Summer 2021 by IMO News Magazine - Issuu,” Jun. 16, 2021. Accessed: Mar. 28, 2023. [Online]. Available: https://issuu.com/imo-news/docs/imo_news_summer_2021_
[54] “EMSA OUTLOOK_2023.”
[55] “The Future of Trucks – Analysis,” *IEA*. https://www.iea.org/reports/the-future-of-trucks (accessed Mar. 28, 2023).
[56] “Maritime Decarbonisation Hub,” *Lloyd’s Register*. https://www.lr.org/en/marine-shipping/maritime-decarbonisation-hub/ (accessed Mar. 28, 2023).
[57] S. Roy *et al.*, “Unraveling Local Structure of Molten Salts via X-ray Scattering, Raman Spectroscopy, and *Ab Initio* Molecular Dynamics,” *J. Phys. Chem. B*, vol. 125, no. 22, pp. 5971–5982, Jun. 2021, doi: 10.1021/acs.jpcb.1c03786.
[58] T. Bauer and W. Ding, *SFERA II Project Deliverable D15.4: Report on innovative techniques for molten salts high temperature measurements*. 2018. doi: 10.13140/RG.2.2.21279.46249.
[59] S. Kakac, A. Pramuanjaroenkij, and X. Zhou, “A review of numerical modeling of solid oxide fuel cells,” *Int. J. Hydrog. Energy*, vol. 32, no. 7, pp. 761–786, May 2007, doi: 10.1016/j.ijhydene.2006.11.028.
[60] M. Ni, M. K. H. Leung, and D. Y. C. Leung, “A modeling study on concentration overpotentials of a reversible solid oxide fuel cell,” *J. Power Sources*, vol. 163, no. 1, pp. 460–466, Dec. 2006, doi: 10.1016/j.jpowsour.2006.09.024.
[61] P. Kim-Lohsoontorn and J. Bae, “Electrochemical performance of solid oxide electrolysis cell electrodes under high-temperature coelectrolysis of steam and carbon dioxide,” *J. Power Sources*, vol. 196, no. 17, pp. 7161–7168, Sep. 2011, doi: 10.1016/j.jpowsour.2010.09.018.
[62] M. Rutherford, A. E. Telgerafchi, G. Espinosa, A. C. Powell, and D. Dussault, “Low-Cost Magnesium Primary Production Using Gravity-Driven Multiple Effect Thermal System (G-METS) Distillation,” in *Magnesium 2021*, Orlando, Florida: TMS, Mar. 2021, pp. 139–144. doi: 10.1007/978-3-030-65528-0_21.

[63] R. O'Hayre, S.-W. Cha, W. Colella, and F. B. Prinz, *Fuel Cell Fundamentals*, 3rd ed. Wiley, 2016. Accessed: Sep. 06, 2021. [Online]. Available: https://www.wiley.com/en-us/Fuel+Cell+Fundamentals%2C+3rd+Edition-p-9781119113805
[64] C. Faria, "High-Efficiency High Power Density Direct Carbon Fuel Cell," Master of Science, Worcester Polytechnic University, Worcester, MA, USA, 2021. Accessed: Mar. 07, 2023. [Online]. Available: https://digital.wpi.edu/concern/etds/3b591c51g
[65] A. Kisza, J. Kazmierczak, B. Børresen, G. M. Haarberg, and R. Tunold, "Kinetics and Mechanism of the Magnesium Electrode Reaction in Molten MgCl2 - NaCl Binary Mixtures," *J. Electrochem. Soc.*, vol. 144, no. 5, p. 1646, May 1997, doi: 10.1149/1.1837654.
[66] K. Du *et al.*, "An iron-base oxygen-evolution electrode for high-temperature electrolyzers," *Nat. Commun.*, vol. 14, no. 1, p. 253, Jan. 2023, doi: 10.1038/s41467-023-35904-7.
[67] DerSilberspiegel, *Ellingham Richardson Diagram*. 2016. Accessed: Apr. 26, 2023. [SVG]. Available: https://commons.wikimedia.org/wiki/File:Ellingham_Richardson-diagram_english.svg
[68] D. L. Wood, J. Li, and C. Daniel, "Prospects for reducing the processing cost of lithium ion batteries," *J. Power Sources*, vol. 275, pp. 234–242, Feb. 2015, doi: 10.1016/j.jpowsour.2014.11.019.
[69] A. C. Powell IV, H. Sun, M. Shahabi, and Y. Zhong, "Metal-Air Battery" Accessed: Oct. 19, 2022. [Online]. Available: https://patents.google.com/patent/US20220302527A1/en